Structure-Property Relationships of Self-Assembled Conjugated Polymers

Pablo de la Iglesia

A dissertation submitted in partial fulfillment of the requirements for the degree of

Doctor of Philosophy

University of Washington

2015

Committee Members:

Prof. Lilo D. Pozzo, Chair

Prof. Jim Pfaendtner

Dr. Kjersta Larson-Smith

Prof. Christine Luscombe, GSR

Program Authorized to Offer Degree:

Chemical Engineering

Abstract

Structure-Property Relationships of Self-Assembled Conjugated Polymers

Pablo de la Iglesia

Chair of the Supervisory Committee:
Associate Professor Lilo D. Pozzo

Department of Chemical Engineering.

Conjugated polymers, due to their unique optical and electronic properties, can be used for applications such as photovoltaic devices, light-emitting diodes, transistors, and organic sensors. Although, conjugated polymers have several promising properties, uses for these materials are often limited by inefficient charge transport. Inducing polymer aggregation improves the efficiency of charge propagation due to an increase on the conjugation length of the polymer and the crystallization of the polymer domains.

The scope of this project is to study the self-assembly of conjugated polymers and its effect on the properties of the materials. More specifically, this project aims to control the kinetics of aggregation in order to affect the structural conformation of the polymer and have an impact on the properties of the material. Self-assembly is controlled by changing parameters such as solvent quality, temperature and dopant chemistry. Both structure and properties change in response to the conditions in which the polymer is placed. This means that the properties of the material could be controlled and optimized. Additionally, a protocol to synthesized organic solvent dispersible Poly(3,4-ethylenedioxythiphehe) is developed and studied. This synthesis uses the controlled aggregation of the polymer strands to prevent the polymer from going out of dispersion. This procedure enables the use of one of the most conductive conjugated polymers in applications previously prohibited due to its poor processability.

Table of Contents

List of Figures

List of Tables

Acknowledgments

Special thanks to the entire Pozzo Group: Dr. Monica Ospinal, Dr. Katie Weigandt, Dr. Kjersta Larson-Smith, Dr. Gregory Newbloom, Dr. Jeffrey Richards, Michael Lombardo M.S., Volha Hrechka, Kiran Kenekal, Yuyin Xi M.S., Yi-Ting Lee M.S., Ryan Kastilani, Dr. Yeneneh Yimer, Dr. David Li and the countless undergraduate students. Thank you all for the help and support, fantastic team, fantastic group! Thanks to Dr. Gregory Newbloom, Michael Lombardo M.S. and Brett Courtright M.S. for the help in the proofreading of this document. The staff in Benson Hall for being the gears which makes the entire apparatus work. To all the professors for the sharing of knowledge.

Very special thanks to Professor Lilo Pozzo for being my guide in the vast sea of the seek for knowledge. Thanks to all my family and friends, you guys are the one that kept me sane during these insane times. Thanks to Josh, Honorio, Edgar, Migan, Diego, Laura, Jose, Anne, everybody else, you guys rock. Thanks to all the baristas at the "H Bar" for providing me the fuel used to do all this work. To my mom, my dad, my other mom, my other dad, my many grandparents, my siblings Richard and Jackie for the support. Thanks to my wife Sara E. Barajas-Juarez for coping with my schedule and the lifestyle of a graduate student, I love you.

This works is partially supported by the Department of Energy Office of Basic Energy Science under the award number DE-SC0005153 and the Boeing Company. We acknowledge the support of the National Institute of Standards and Technology in providing the neutron research facilities for this work. This work benefited from the DANSE software developed under NSF award DMR-0520547. Part of this work was conducted at the University of Washington NanoTech User Facility, a member of the NSF National Nnaotechnology Infrastructure Network

(NNIN). We would like to thank Jae H. Cho (NIST CNR, Gaithersburg, MD) for providing the combined model use within DANSE software package and Matthew Washbrough (NIST CNR, Gaithersburg, MD) for his help with the neutron scattering experiments. This work was done with the following collaborators: Chapter 4 collaborator Dr. Gregory Newbloom (UW, chemical engineering department) P3AT work. Chapter 5 collaborators Yuyin Xi (UW, chemical engineering department) electrochemistry experiment, Vance Jaeger and Prof. Jim Pfaendtner (UW, chemical engineering department) for the simulation of the organometallic salts. Chapter 6 collaborators Dr Kjersta Larson-Smith (the Boeing Company Research Division). Other collaborators Dr. Josh Cardiel and Prof. Amy Shen (UW, mechanical engineering department)

Para Eloisa

Chapter I

Introduction

Self-Assembly of Conjugated Polymers.

Polymeric materials are considered to be electrical insulators. Due to their chemistry and disorganized molecular structure, polymers do not transport charge very efficiently[1]. In the late 20th century a new generation of polymers caught the attention of researchers, conjugated polymers (CPs). CPs possess conjugated π-electrons. The resonance interactions between the π-bonds results in delocalized π-electron states[2]. The CPs have an energy band gap formed by the highest occupied molecular π orbital and the lowest unoccupied molecular π orbital, this gap is normally on the range of 1.5 eV to 3 eV for CPs (the range of visible light and the near infrared)[2]. The electron delocalization and the existence of the energy gap gives rise to the semiconducting behavior on these organic materials. CPs are versatile due to their unique optical and electronic properties, and because they can be used for applications such as photovoltaic devices, light-emitting diodes, transistors, organic sensors, and many more[3-6]. CPs can be designed to specific desired properties such as energy band gap and charge carrier mobility. These modifications can be achieved by the selection of the polymer backbone[7, 8]. Furthermore, the backbone can be decorated with alkyl chains in order to modulate the solubility of the polymer in organic solvents. Also, CPs and CP devices are potentially cheaper to mass produce due to the availability of the raw materials and their processability[9-12]. Although CPs possess several promising properties, uses for these materials are often limited by

inefficient charge transport[13]. CPs form complex microstructures that are embedded in an amorphous matrix. The disordered matrix causes low conductivity of the system by increasing the frequency of difficult charge carriers' hopping processes due to breaks in conjugation caused by bends and kinks in the backbone chain[2].

Several approaches can be taken in order to increase the charge transfer efficiency of CPs. Doping the polymers with metals or small molecules increases their conductivity[14]. However, doing so will alter the properties of the polymer by either degradation of the polymer itself or by significantly decreasing its solubility[15]. It has been shown that crystallization of the polymer can sometimes result in more efficient charge propagation[13, 16]. Moreover, crystallization facilitates the aggregation of the polymer into fibers, sheets and other organized multi-chain assemblies[17-19]. In concentrated solutions, such aggregates can also interconnect to form percolating organogels[20-22]. Organogel formation has been reported for different CPs such as poly(3-alkyl-thiophene) (P3ATs), poly(9,9 dialkyl fluorene) (PFAs) and poly(vinylene phenylene) (PVPs), showing that this is common behavior in these systems[18, 23, 24]. The formation of organogels is usually only possible in solvents of moderate polymer solubility. If the polymer is too soluble, the sample never aggregates to form gels. Oppositely, if the polymer is too insoluble in a specific solvent, it remains permanently associated with other chains so that it cannot fully dissolve and, therefore, cannot gel. Consequently, the gelation of conjugated polymer chains is usually induced by gradually decreasing the solubility of a conjugated polymer in solvents of modest quality by systematically altering the solvent composition (i.e. adding a miscible non-solvent) or by changing temperature.

The degree of aggregation and the structural characteristics of organogel networks (e.g. cross-sectional dimensions and fiber connectivity) formed from CPs are also strongly dependent on the specific conditions of the experimental system (e.g. polymer backbone chemistry, solvent type, molecular weight, concentration and gelation temperature). Ultimately, all of these parameters can individually affect the driving force for aggregation (i.e. supersaturation) and therefore change the kinetics of gelation. It has also been shown that the kinetics of gelation are critically important to determining the final structure and properties of these aggregates. In fact, the degree of supersaturation has been found to be one of the most important parameters in the description of organogel formation from small molecules[25, 26]. Therefore, the structure and properties of the polymer aggregates could be designed for specific organic electronic applications.[21, 27, 28]

The objective of this project is to study the aggregation of CPs. This study focuses on three different polymer backbones: poly(3-alkyl-thiophene) (P3ATs), poly(9,9 dialkyl fluorene) (PFAs) and poly(3, 4-ethylenedioxythiophene) (PEDOT). Specifically, the conditions to be studied are:

- The effect of solvent choice and temperature on poly(9,9 dioctyl fluorene) (PFO) organogels
- The effect of solvent quality and alkyl side chain length in P3ATs
- The effect of alkyl chain dopant on the self-assembly of PEDOT.

The study specifically aims to characterize the size, shape and crystallinity of the polymer aggregates as the self-assembly conditions are changed. This work also intends to

measure the effect that morphological, kinetic, and thermodynamic changes have over the rheological and electrical properties of the systems.

Synthesis of PEDOT:Surfactant Complexes.

The presence of isolated ions in non-polar media is difficult to achieve. The driving forces for the dissolution and dissociation of electrolytes in non-polar media are very different from those in aqueous solutions[29, 30]. The Bjerrum length in non-polar media is considerably large due to the low dielectric constant of the solvent. For this reason, the distance between ions needs to be significant in order to maintain a stable dispersion of the charge carriers. Charge stabilization is mainly achieved through the dispersion of a surfactant in the non-polar media[30]. The surfactant's head encapsulates the charge carriers; meanwhile, the hydrophobic organic tail prevents the charged groups from getting too close to each other, stabilizing the dispersion.

Incorporating metal ions into organic solvents makes possible their use in applications were their aqueous nature previously prevented it. Metal ions in organic solvent could be used for: electrolyzing an organic solvent[31, 32], developing organic solvent-based flow cells[33-35], and as oxidizing agent for reactions in organic solvents[36]. The last application is particularly important for CPs, since it would make it possible to use dispersed iron (III) ions to synthesize the polymers directly in organic solvents.

This work describes a facile way of synthesizing a metal-surfactant salt. This metal salt can be readily dispersed in non-polar solvents, stabilized by micelle formation. The behavior of the salt is probed while dispersed in different solvent types such as alcohols, aromatics, alkanes, and halogens. The effect of concentration, water content,

and aging is also studied using scattering and simulation techniques. Conductivity and electrochemical behavior of these salts are also explored.

Finally, iron(III) salts are used to synthesize PEDOT dispersible in organic solvents. The iron(III) salts also simultaneously dope the polymer with the surfactant that pairs the Iron (III) ion. In addition to doping the polymer, the surfactant also stabilizes the PEDOT dispersion by preventing uncontrollable aggregation through steric interactions. In this way it is possible to affect the polymer packing in dispersion by the dopant choice. This work uses microscopy techniques to observe the different structures formed by the polymer domains, as well as the difference in the conductivity and stability of the different PEDOT:surfactant complexes.

References

1. Riande, E.; R., D.-C., *Electrical Properties of Polymers*. Marcel Dekker: New York, 2004.
2. Strobl, G., *The Physics of Polymers*. Springer: New Yotk, 2007.
3. Guenes, S.; Neugebauer, H.; Sariciftci, N. S., Conjugated polymer-based organic solar cells. *Chemical Reviews* 2007, 107, (4), 1324-1338.
4. Bernius, M. T.; Inbasekaran, M.; O'Brien, J.; Wu, W. S., Progress with light-emitting polymers. *Advanced Materials* 2000, 12, (23), 1737-1750.
5. Horowitz, G., Organic field-effect transistors. *Advanced Materials* 1998, 10, (5), 365-377.
6. Goncalves, V. C.; Balogh, D. T., Optical VOCs detection using poly(3-alkylthiophenes) with different side-chain lengths. *Sensors and Actuators B-Chemical* 2009, 142, (1), 55-60.
7. Meyers, F.; Heeger, A. J.; Bredas, J. L., FINE TUNING OF THE BAND-GAP IN CONJUGATED POLYMERS VIA CONTROL OF BLOCK COPOLYMER SEQUENCES. *Journal of Chemical Physics* 1992, 97, (4), 2750-2758.
8. Roncali, J., Synthetic principles for bandgap control in linear pi-conjugated systems. *Chemical Reviews* 1997, 97, (1), 173-205.
9. Garnier, F.; Hajlaoui, R.; Yassar, A.; Srivastava, P., ALL-POLYMER FIELD-EFFECT TRANSISTOR REALIZED BY PRINTING TECHNIQUES. *Science* 1994, 265, (5179), 1684-1686.
10. Fuchigami, H.; Tsumura, A.; Koezuka, H., POLYTHIENYLENEVINYLENE THIN-FILM-TRANSISTOR WITH HIGH CARRIER MOBILITY. *Applied Physics Letters* 1993, 63, (10), 1372-1374.

11. Koezuka, H.; Tsumura, A.; Fuchigami, H.; Kuramoto, K., polythiophene field-effect transistor with polypyrrole worked as source and drain electrodes. *Applied Physics Letters* 1993, 62, (15), 1794-1796.
12. Assadi, A.; Svensson, C.; Willander, M.; Inganas, O., field-effect mobility of poly(3-hexylthiophene). *Applied Physics Letters* 1988, 53, (3), 195-197.
13. Sirringhaus, H.; Brown, P. J.; Friend, R. H.; Nielsen, M. M.; Bechgaard, K.; Langeveld-Voss, B. M. W.; Spiering, A. J. H.; Janssen, R. A. J.; Meijer, E. W.; Herwig, P.; de Leeuw, D. M., Two-dimensional charge transport in self-organized, high-mobility conjugated polymers. *Nature* 1999, 401, (6754), 685-688.
14. Martens, H. C. F.; Hulea, I. N.; Romijn, I.; Brom, H. B.; Pasveer, W. F.; Michels, M. A. J., Understanding the doping dependence of the conductivity of conjugated polymers: Dominant role of the increasing density of states and growing delocalization. *Physical Review B* 2003, 67, (12).
15. deLeeuw, D. M.; Simenon, M. M. J.; Brown, A. R.; Einerhand, R. E. F., Stability of n-type doped conducting polymers and consequences for polymeric microelectronic devices. *Synthetic Metals* 1997, 87, (1), 53-59.
16. Chang, J. F.; Sun, B. Q.; Breiby, D. W.; Nielsen, M. M.; Solling, T. I.; Giles, M.; McCulloch, I.; Sirringhaus, H., Enhanced mobility of poly(3-hexylthiophene) transistors by spin-coating from high-boiling-point solvents. *Chemistry of Materials* 2004, 16, (23), 4772-4776.
17. Knaapila, M.; Garamus, V. M.; Dias, F. B.; Almasy, L.; Galbrecht, F.; Charas, A.; Morgado, J.; Burrows, H. D.; Scherf, U.; Monkman, A. P., Influence of solvent quality on the self-organization of archetypical hairy rods - Branched and linear side chain polyfluorenes: Rodlike chains versus "beta-sheets" in solution. *Macromolecules* 2006, 39, (19), 6505-6512.
18. Samitsu, S.; Shimomura, T.; Ito, K., Nanofiber preparation by whisker method using solvent-soluble conducting polymers. *Thin Solid Films* 2008, 516, (9), 2478-2486.
19. Malik, S.; Jana, T.; Nandi, A. K., Thermoreversible gelation of regioregular poly(3-hexylthiophene) in xylene. *Macromolecules* 2001, 34, (2), 275-282.
20. Justino, L. L. G.; Luisa Ramos, M.; Knaapila, M.; Marques, A. T.; Kudla, C. J.; Scherf, U.; Almasy, L.; Schweins, R.; Burrows, H. D.; Monkman, A. P., Gel Formation and Interpolymer Alkyl Chain Interactions with Poly(9,9-dioctylfluorene-2,7-diyl) (PFO) in Toluene Solution: Results from NMR, SANS, DFT, and Semiempirical Calculations and Their Implications for PFO beta-Phase Formation. *Macromolecules* 2011, 44, (2), 334-343.
21. Newbloom, G. M.; Weigandt, K. M.; Pozzo, D. C., Electrical, Mechanical, and Structural Characterization of Self-Assembly in Poly(3-hexylthiophene) Organogel Networks. *Macromolecules* 2012, 45, (8), 3452-3462.
22. Newbloom, G. M.; Weigandt, K. M.; Pozzo, D. C., Structure and property development of poly(3-hexylthiophene) organogels probed with combined rheology, conductivity and small angle neutron scattering. *Soft Matter* 2012, 8, (34).

23. Chen, C. Y.; Chang, C. S.; Huang, S. W.; Chen, J. H.; Chen, H. L.; Su, C. L.; Chen, S. A., Phase-Separation-Induced Gelation of Poly(9,9-dioctylfluorene) Methylcyclohexane Solution. *Macromolecules* **2010,** 43, (9), 4346-4354.
24. Malik, S.; Nandi, A. K., Crystallization mechanism of regioregular poly(3-alkyl thiophene)s. *Journal of Polymer Science Part B-Polymer Physics* **2002,** 40, (18), 2073-2085.
25. Li, J. L.; Liu, X. Y.; Wang, R. Y.; Xiong, J. Y., Architecture of a biocompatible supramolecular material by supersaturation-driven fabrication of its fiber network. *Journal of Physical Chemistry B* **2005,** 109, (51), 24231-24235.
26. Li, J.-L.; Yuan, B.; Liu, X.-Y.; Xu, H.-Y., Microengineering of Supramolecular Soft Materials by Design of the Crystalline Fiber Networks. *Crystal Growth & Design* **2010,** 10, (6), 2699-2706.
27. Keum, J. K.; Xiao, K.; Ivanov, I. N.; Hong, K.; Browning, J. F.; Smith, G. S.; Shao, M.; Littrell, K. C.; Rondinone, A. J.; Andrew Payzant, E.; Chen, J.; Hensley, D. K., Solvent quality-induced nucleation and growth of parallelepiped nanorods in dilute poly(3-hexylthiophene) (P3HT) solution and the impact on the crystalline morphology of solution-cast thin film. *CrystEngComm* **2013,** 15, (6), 1114-1124.
28. Chang, M.-Y.; Huang, Y.-H.; Han, Y.-K., Aggregation, crystallization, and resistance properties of poly(3-hexylthiophene-2,5-diyl) solid films gel-cast from CHCl3/p-xylene mixed solvents. *Organic Electronics* **2014,** 15, (1), 251-259.
29. Beunis, F.; Strubbe, F.; Karvar, M.; Drobchak, O.; Brans, T.; Neyts, K., Inverse micelles as charge carriers in nonpolar liquids: Characterization with current measurements. *Current Opinion in Colloid & Interface Science* 18, (2), 129-136.
30. Dukhin, A.; Parlia, S., Ions, ion pairs and inverse micelles in non-polar media. *Current Opinion in Colloid & Interface Science* **2012,** 18, (2), 93-115.
31. Bond, A. M.; Fleischmann, M.; Robinson, J., Electrochemistry in Organic-Solvents Without Supporting Electrolyte Using Platinium Microelectrodes. *Journal of Electroanalytical Chemistry* **1984,** 168, (1-2), 299-312.
32. Hall, D. A.; Elving, P. J., voltammetry without background electrolyte - redox pattern of dpph in non-aqueous media. *Electrochimica Acta* **1967,** 12, (9), 1363-&.
33. Shinkle, A. A.; Pomaville, T. J.; Sleightholme, A. E. S.; Thompson, L. T.; Monroe, C. W., Solvents and supporting electrolytes for vanadium acetylacetonate flow batteries. *Journal of Power Sources* **2014,** 248, 1299-1305.
34. Xie, Z.; Liu, Q.; Chang, Z.; Zhang, X., The developments and challenges of cerium half-cell in zinc-cerium redox flow battery for energy storage. *Electrochimica Acta* **2013,** 90, 695-704.
35. Zhang, D.; Lan, H.; Li, Y., The application of a non-aqueous bis(acetylacetone)ethylenediamine cobalt electrolyte in redox flow battery. *Journal of Power Sources* **2012,** 217, 199-203.
36. Elschner, A.; Kirchmeyer, S.; Lovenich, W.; Merker, U.; Reuter, K., *PEDOT: Principles and Application of an Intrinsically Conductive Polymer*. CRC Press: Boca Raton, Fl, 2011.

Chapter II

Methodology.

Rheology.

Rheology studies the mechanical properties of materials. Rheology is mainly used in order to measure the robustness of materials and to predict their performance during processing or in specific applications.[1] Additionally, rheology can be used to calculate the flow properties of fluids and other soft materials.[2] Rheology specifically measures the relation between the quantity of force applied to a sample and the amount of deformation caused by said force.

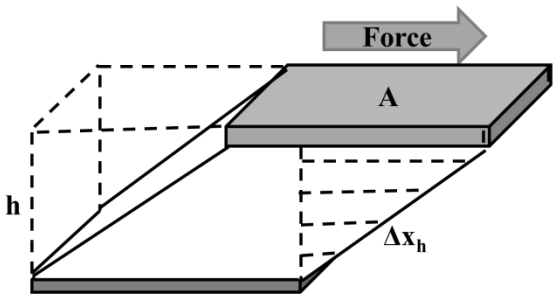

Figure 2.1: Schematic of a shear force applied to a sample. The parameters of height (h), area (A), force (F) and linear displacement (Δx_h) are the parameters used to calculate the rheological properties of the material.

$$\tau = \frac{F}{A} \qquad \text{(Eq. 2.1)}$$

$$\gamma = \frac{\Delta x_h}{h} \qquad \text{(Eq. 2.2)}$$

Figure 2.1 shows the physical representation of the applied force and the deformation of the probed material.[1] From the parameters in figure 2.1, shear stress and shear strain are defined in equations 2.1 and 2.2 respectively. Where τ is shear stress – is defined as the applied force (F) over the area (A) where the force is applied – and γ is the shear strain – defined as the linear displacement (Δx_h) over the gap thickness (h).

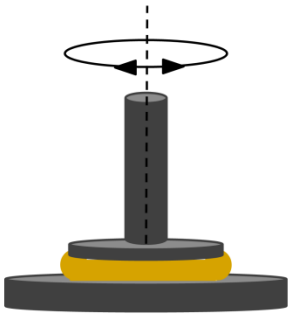

Figure 2.2: Schematic representation of the setup used for small amplitude oscillatory rheology.

In this work small amplitude oscillatory rheology is used to probe the gelation kinetics, structure and properties of intrinsically conductive polymer organogels. In this test a small sinusoidal oscillation of either strain or stress is applied at a constant frequency, while the complementary property is measured (figure 2.2). By doing this a plot similar to figure 2.3 can be obtained where stress and strain are tracked as the oscillation takes places. Based on the relative behavior of stress to strain, information about the nature of the material can be obtained. If the phase shift (δ from figure 2.3) is 0º, the strain and stress in the sample are synchronized, which means that the sample is comprised of a pure elastic material (i.e. solid). If the sample were a pure viscous material (i.e. liquid) the lag between strain and stress would be at a maximum causing δ to be 90º.[2] A δ value of $0º<\delta<90º$ indicates that the sample contains both elastic and vicious components; these materials are deemed viscoelastic materials.[2] For the scope of

this work, the viscoelasticity of the organogel networks arises from the elastic behavior of the polymer aggregates combined with the viscous nature of the solvent and dissolved polymer trapped within the solid domains.

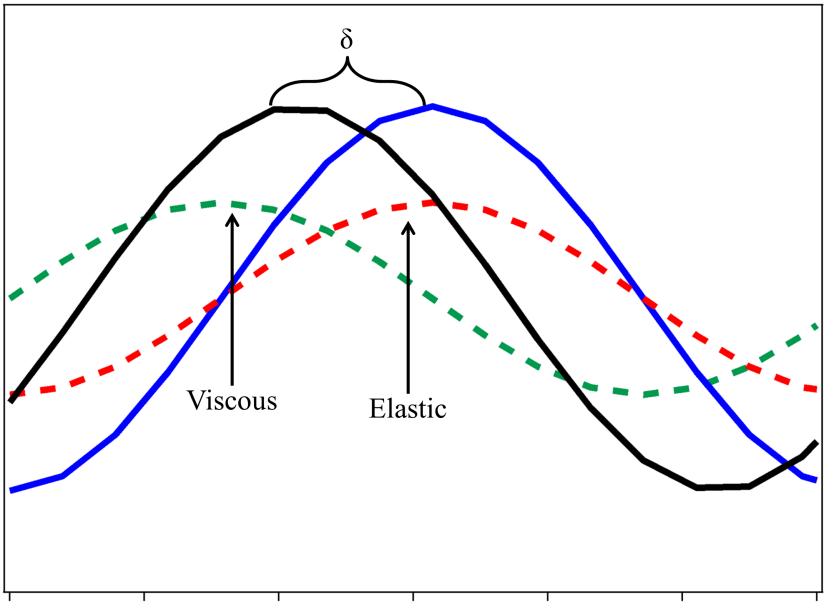

Figure 2.3: Representation of a stress and a strain curve. The black solid line represents the applied perturbation (either stress or strain) while the solid blue line is the system's response. The dashed lines represent the elastic and viscous components of the sample's response.

$$\tau = \gamma_0[G'\sin(\omega t) + G''\cos(\omega t)] \qquad \text{(Eq. 2.3)}$$

Equation 2.3 describes the strain-stress relation in a viscoelastic material. In this equation the stress (τ) and the strain amplitude (γ_0) are related by the storage modulus (G') and the loss modulus (G'') at any given frequency (ω) and time (t). The storage modulus quantifies the elastic response in the sample, while the loss modulus represents the viscous response. By measuring these two parameters it is possible to determine the

viscoelastic state of a sample. In a more elastic sample G'>G'' whereas in a more viscous system the opposite is true (i.e. G''>G')

In order to accurately study the viscoelastic properties of a system with small amplitude oscillatory rheology, two key parameters need to be taken into consideration: 1) the linear viscoelastic regime of the system and 2) the relaxation frequency of the materials.

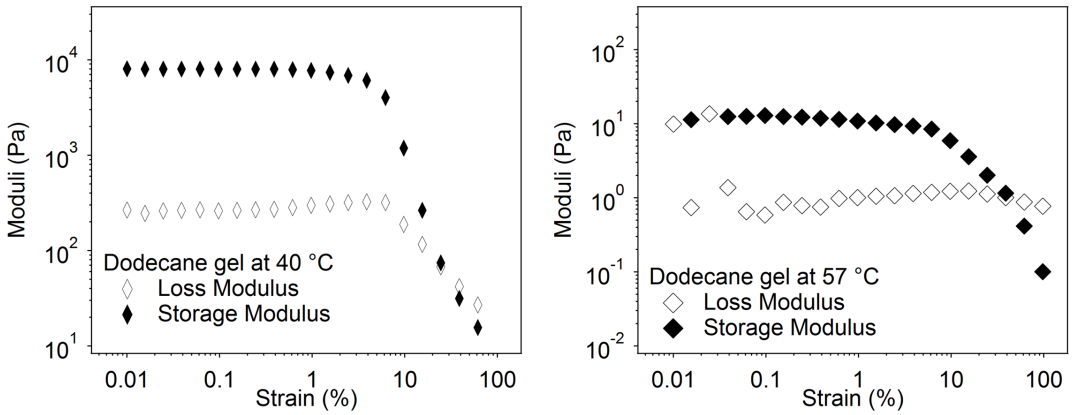

Figure 2.4: Strain sweeps of fully developed gels in in dodecane at two different temperatures. Based on these curves, a strain of 0.1% was chosen in order to be within the linear viscoelastic regime of the sample.

The linear viscoelastic regime is the section of strain/stress where the structure of the material is not being affected by the perturbation amplitude. Figure 2.4 show the storage and loss modulus of PFO organogel samples at different oscillatory strain. At small enough perturbation the material is probed without damaging its structure, and the magnitude of the moduli does not change. If the strain is increased too much, the organogel structure starts to break down, which translates in a rapid decrease in the magnitude of the moduli. It is very important to keep the perturbation strain within the

linear viscoelastic regime in order to prevent damaging the system as the measurement is being conducted.

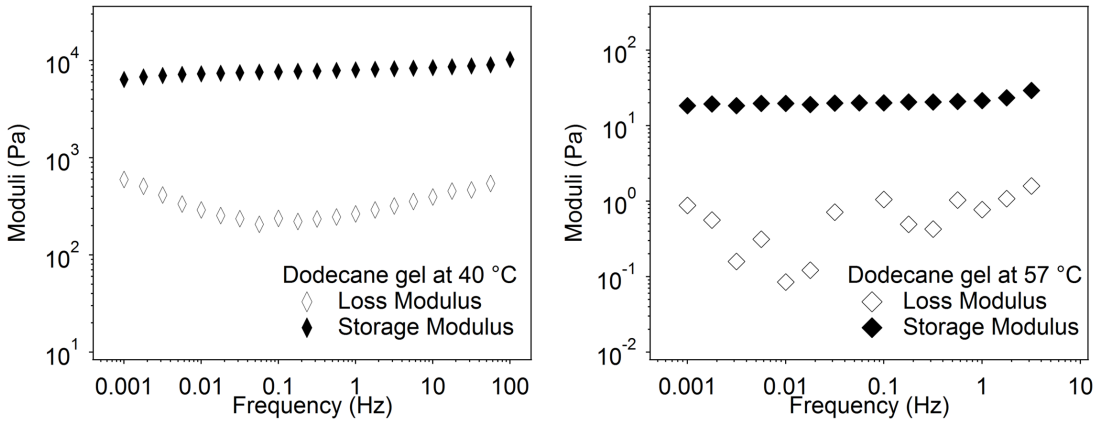

Figure 2.5: Frequency sweeps of fully developed gels in dodecane at two different temperatures. All the samples behave as gels during the entire frequency range.

The moduli behavior of a material as a function of frequency is another key parameter to test. In the organogels the magnitude of the storage modulus is higher than the loss modulus at the frequency probed. However, it is important to test if that behavior holds in a wide range of frequencies. If at a lower frequency the storage and the loss modulus were to flip this would indicate the presence of a relaxation frequency. This is a sign that the sample cannot be characterized as a gel but as a very viscous liquid. Figure 2.5 shows the moduli behavior of several PFO gels for a wide range of frequencies. It is observed that none of the samples show any cross-over in the frequency range probed.

Small Angle Scattering.

Small angle scattering techniques (SAS) are used to characterize the nano and micro scale morphology of materials. These techniques do not require extensive sample preparation unlike electron microscopy techniques (i.e. TEM, SEM). The lack of sample

manipulation, in addition to the non-invasiveness of the technique, makes SAS ideal techniques to study the in-situ morphology of colloidal and soft matter systems. In the present work, SAS are used to characterize the morphology of conjugated polymer organogels and metalorganic surfactants under various conditions.

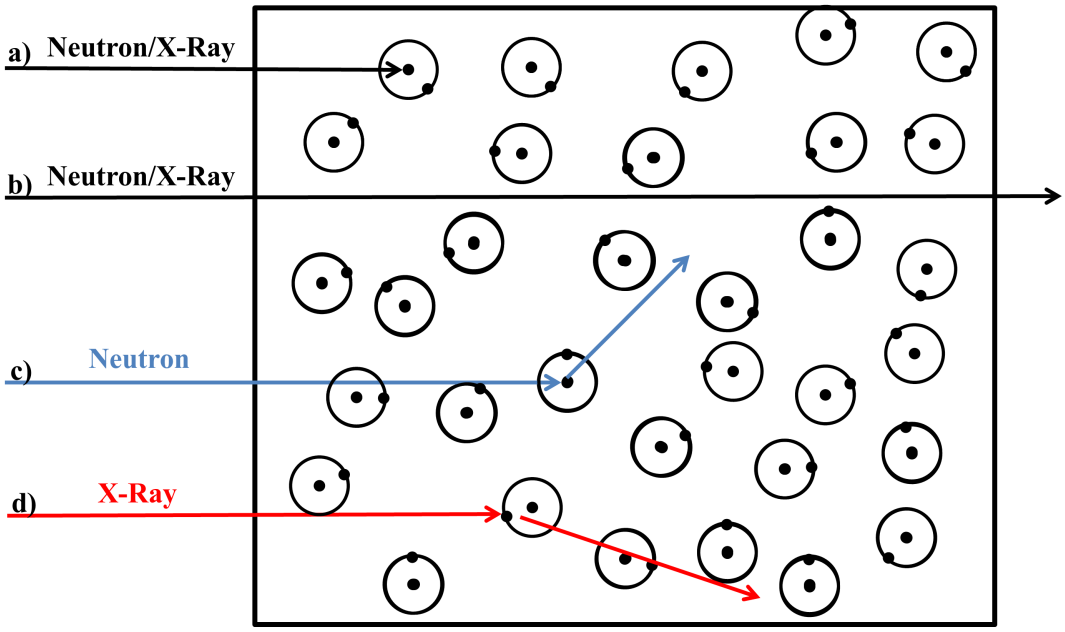

Figure 2.6: A schematic of the possible interaction of the neutron or X-ray incident beam with the sample. The neutron/X-ray can be a) absorbed, b) transmitted, c) nuclear scattering (neutrons) d) electron cloud scattering (X-Ray).

SAS techniques include neutron and X-ray scattering. Small angle neutron scattering (SANS) and small angle X-ray scattering (SAXS) follow similar principles.[3] A beam of either neutrons or X-rays is generated. The geometry of the beam is manipulated and it is guided to pass thru the sample to be analyzed. When the neutron/X-ray beam passes thru the sample, one of four interactions can occur. Some neutrons/X-rays are absorbed by the sample (figure 2.6 a). Most of the neutrons/X-rays are transmitted through and do not interact in any way with the sample (figure 2.6 b). Some of the

neutron/X-rays get scattered; their paths change after interacting with the sample. From these possible outcomes, elastic scattering is the one that provides information on the conformation of the molecules and aggregates of the samples.[3]

SAXS and SANS can be considered complimentary techniques. Neutrons interact with the samples via the atomic nuclei (figure 2.6 c), while the X-rays interact with the electron clouds via electromagnetic interactions (figure 2.6 d).[3] This translates to each technique having different resolutions for any given chemical elements. Furthermore, neutron scattering's ability to discriminate elements (i.e. scattering length) varies almost randomly. This is more noticeable in the case of hydrogen and deuterium where even though they are different isotopes of the same element, their scattering lengths vary from -3.739×10^{-13} cm for hydrogen to 6.671×10^{-13} cm for deuterium.[4] This high contrast between hydrogen and deuterium is commonly exploited to highlight sections of the samples in order to obtain more detailed information in the area of interest.[5] For example, in a polymer-organic solvent system, it is possible to use the deuterated version of the solvent (i.e. hydrogen substituted with deuterium) in order to highlight the conformation of the hydrogen-rich polymer.

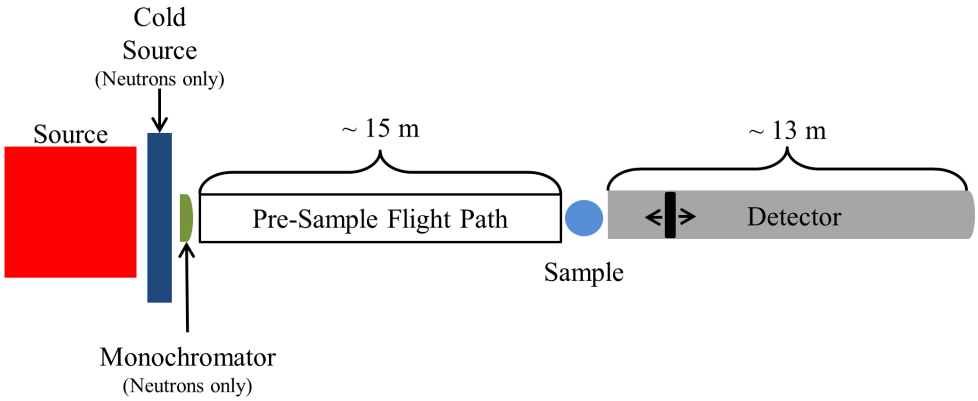

Figure 2.7: Schematic representation of the components on neutron and X-ray scattering instruments.

Figure 2.7 shows a schematic of a SAS instrument. Although the specifics vary depending on the technique and even from instrument to instrument, all of them share the same basic structure. The following section will describe the SANS setup used at the National Institute of Standards and Technology's Center for Neutron Research (NCNR).[5, 6] This facility is used for all the SANS experiments in this dissertation. A discussion for the SAXS instrument used in this work will follow, and it will highlight the parallels and differences between the two setups.

Neutron sources are nuclear reactors mainly based on the fission reaction of U-235. This makes the construction and maintenance of SANS instruments extremely expensive, and therefore it is necessary to use government-subsided facilities such as the NCNR.[5] The neutrons are passed thru liquid hydrogen or deuterium in order to decrease their energy. This section of the instrument is deemed the cold source, and this is done in order to increase the wavelength of the neutrons and improve the spatial resolution for scattering applications. The cold neutrons are passed through a monochromator that only lets through neutrons with a desired wavelength and wavelength spread. Then they are

passed through a series of apertures, which cut the beam into the desired size and shape. Regularly these apertures are circular in size and have different radii depending on the experimental configuration. The collimated beam interacts with the sample, and the transmitted and scattered neutrons are registered on a 2-D detector. The detector at the NCNR is mobile in order to obtain the neutron counts at different distances from the sample.[6] By changing the sample-to-detector distance, different scattered angles are made available; this allows the probing of a wider size range of the sample's conformation.

X-rays are formed using a vacuum tube, by colliding high-speed electrons with a metal target (for this study a copper source is used).[7] The X-ray generator is more affordable, compared to the neutron source, which makes SAXS instruments more accessible to researchers. Additionally SAXS equipment does not require a cold source nor a wavelength selector, since the wavelength of the X-ray depends on the metal from which they are created. The X-rays from the copper source have a wavelength of 0.15 nm^{-1}. The X-ray beam is collimated to a line-shape using a bent-multilayer mirror and a polished metal block. The line collimation setup is chosen in order to increase the X-ray flux hitting the sample and decrease the counting time required to get accurate results. After the X-rays interact with the sample they are recorded by a fixed 2-D detector, which records the scattering intensity in the entire angle range. The detector in the SAXS setup is not mobile.

$$q = 4\pi \frac{\sin(\theta/2)}{\lambda} \qquad \text{(Eq. 2.4)}$$

The 2-D scattering profile is converted to a 1-D scattering intensity vs. the scattering vector (q) profile, by integrating the counts at the different scattering angles.

The scattering vector is defined in equation 2.4 where θ is defined as the angle between the incident beam and the scattered neutron/X-ray and γ is the wavelength of neutron/X-rays.[3] The SANS data is corrected by accounting for background (environmental) radiation, and the scattering of the container holding the sample. The data is reduced into the 1-D plot using the NIST Igor-based macros.[8] The SAXS data is similarly corrected by accounting for the scattering of the empty container and reduced using the SAXSQuant software.

$$d = \frac{2\pi}{q} \qquad \text{(Eq. 2.5)}$$

The scattering vector typically has units of $Å^{-1}$. The unit of inverse length is due to the data being collected in reciprocal space. The real space equivalent of the q-vector can be estimated using Bragg's law (equation 2.5).[3] This is also the most basic form of data analysis, where the presence of intense peaks can be attributed to features of the corresponding size related to their position in the vector-q. The following sections will go into more sophisticated data analysis methods.

Standard plots.

Standard plots are the next step in the complexity of the data analysis of SAS. These consist of linear relations which are obtained by plotting a function of the scattering intensity (I(q)) versus a function of the scattering vector (q). There are many examples of standard plots that can be applied to scattering data. This section will describe the Guinier and the Porod plot that are the standard plots used in this work.

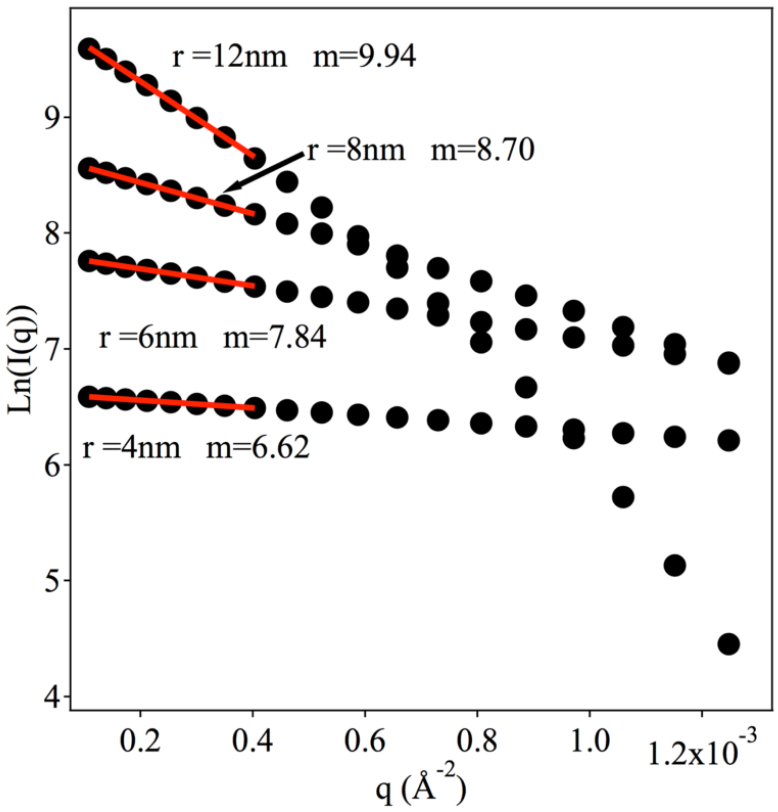

Figure 2.8: Guinier plot of the simulated scattering of spheres of different radii.

$$R_g^2 = 3m \qquad \text{(Eq. 2.6)}$$

The Guinier analysis is obtained by plotting the ln(I(q)) vs q^2.[3] The radius of gyration (R_g) can be obtained from the slope (m) of the linear region of the Guinier plot using equation 2.6. R_g describes the mass momentum of inertia distribution of the sample components, and the parameter is independent of the particle's shape. For this reason this analysis can be applied with limited knowledge of the conformation of the sample. Figure 2.8 shows the Guinier analysis of the simulated scattering of spherical particles of different sizes in order to illustrate the effect that incremental size increases have on the slope of the Guinier plot.

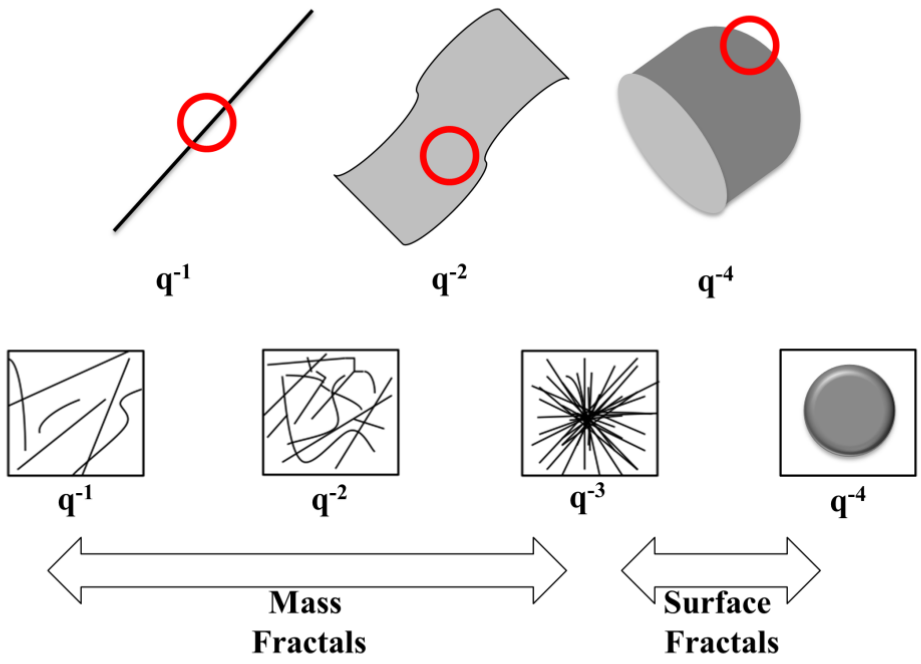

Figure 2.9: Cartoon representation of the possible conformation causing the different Porod exponents. In the case of the mass or surface fractals, values in between whole number exponents are very common and indicate an intermediate conformation between the fractals.

The Porod analysis is done by plotting the $\log_{10}(I(q))$ vs the $\log_{10}(q)$.[5] The slope obtained from this plot can be interpreted as the fractal dimension of the scattering objects. Figure 2.9 shows a cartoon representation of what the different slopes may indicate depending of the nature of the sample. This figure is adapted from figure 7 of Chapter 22 in the SANS Toolbox document.[5]

Form factor fitting.

$$I(q) = \varphi(\Delta SLD)^2 P(q) S(q) + bkg \quad \text{(Eq. 2.7)}$$

The shape of the I(q) vs q plot of the scattering profile is related to the conformation of the scattering elements. This conformational information can be

extracted from the plot by fitting a mathematical model to the data. Equation 2.7 shows the general relation between I(q) and q when the scattering data is represented in absolute scale, where ϕ is the volume fraction of the scattering particle, ΔSLD is the difference between the scattering length density of the particles and the media in which they are dispersed.[3] P(q) and S(q) are the form factor and the structure factor of the scattering bodies, respectively.[3] The structure factor (S(q)) accounts for the spatial correlations of the particles, however in the present study all the systems analyzed fall within the overlap concentration. This means that the contribution to the scattering profile from the structure factor is negligible (S(q)~1). Therefore the form factor is the only contributor to the shape of the scattering profiles while the magnitude can be affected by the volume fraction of the scattering particles and the differences in the scattering length densities.

Different form factors are used in the present work in order to analyze the scattering profiles of the different systems. The form factors used are core and shell sphere, ellipsoid and cylinder. These form factors describe a particle with different materials forming an inner and an outer layer. More information on the description and usage of these models can be found in chapter 6 and in the literature. For some of the systems, none of the shape-specific form factors properly describe the data. For these cases a shape-independent form factor is used in order to obtain information about the particle's dimensionality and characteristic size. The specific shape-independent form factor used in the present work is the Guinier-Porod model, about which more information can be found in the literature and in chapter 3. A model combining the Gaussian polymer and the parallelepiped form factors is also used. This model helps to track the transition of a system that initially behaves as a Gaussian polymer. In the system

the polymer strands start to interact among each other to form fibers with a rectangular cross-section. Additionally, the combined model can be used to probe how much of the material transitioned from one phase to the other by determining the contributions of both form factors to the scattering profile and then relating the contributions to the volume fractions of the material in the different conformations. This model was developed by Newbloom et al. and is used in chapter 4 of this thesis.

The data is analyzed using the DANSE SasView software. This fitting package already contains all the form factors used in the present work. Additionally the software package contains tools to readily combine two form factors which also facilitated the analysis of the organogel systems (chapter 4). DANSE SasView also accounts for the collimations (point and line) from the different instruments used. The embedded tools in the software mathematically modify the models in order to account for the incident beam collimation; this is a better alternative than accounting for beam collimation by data manipulation.

Transmission Electron Microscopy.

Transmission electron microcopy (TEM) is a technique that uses a beam of electron to image nano and micro scale elements of samples. TEM sends and electron beam to interact with the sample and then an image is formed from the electrons transmitted through the sample (figure 2.10).[9] The electron beam is normally passed thru three stages of lenses. The first stage is called the condenser lenses which control the shape of the electron beam. The shape of the beam is used to control the magnification and resolution of the images obtained from the instrument. The second set of lenses is called the objective stage. These lenses focused the beam coming of the sample. The projector lenses magnifies the electron beam into a fluoresce screen or into a charge-

coupled device camera for recording.[9] The configuration of the lenses can vary widely depending on the instrument since different manufactures use their own configuration.

Due to the small wavelengths of the electrons, TEM is able to image at significantly higher magnification than light microscopes. This enables the imagining of very small structures, in the order of a couple nanometers in size. This technique relies on the sample to have some degree of crystallinity in order to obtain a clear image at very high magnifications. For this work, which consists of polymer systems, the contrast of the organogel domains decreases as the samples is brought into focus. The decrease in contrast is due to the amorphous nature of the polymer domains. A better technique for polymer systems is scanning transmission electron microscopy (sTEM).[10] In sTEM the electron beam is focused into a small area using a second set of objective lenses right before the sample. The image is created as the sample is scanned with the focused beam. This produces images with amorphous materials. The drawback of sTEM is that, due to the concentrated of the electron beam, the sample can be damaged if a high intensity of electrons is used.

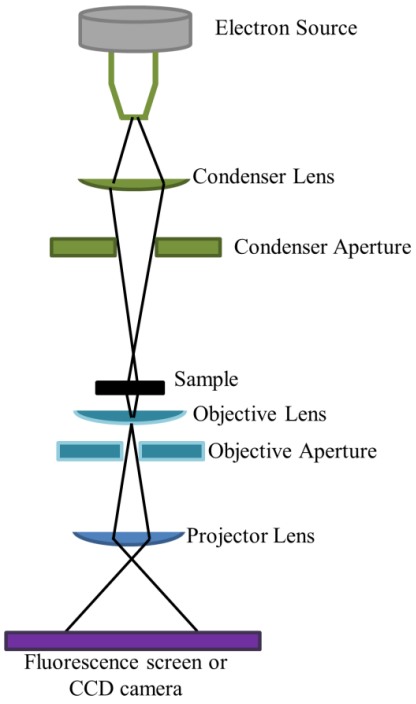

Figure 2.10: Schematic representation of the components on a transmission electron microscope.

A FEI (Hillsboro, OR) Tecnai G2 F20 transmission electron microscope (TEM) is used for scanning transmission electron microscopy (sTEM) operating at 200kV. An ultrathin, TEM copper grid with Formvar support (Ted Pella, Redding, CA) is used as support to image the samples. The sample is mounted into the grid by gently tapping the grid into the surface of the organogel, or in the case of the PEDOT dispersions by drop casting a small amount (~10μL) of the sample. Because of the thin nature of the transferred sample, the solvent evaporates rapidly under ambient conditions. TEM and STEM are limited to very thin and dried samples. This sample manipulation may cause the sample to change conformation from their native state. Additionally, the nature of the techniques only allows the proving of small sections of the samples, which limits the analysis of the sample to the judgement of the scientist.

References

1. Berg, J. C., *An Introduction to Interfaces and Colloids: The Bridge to Nanoscience*. World Scientific Publishing Co. Pte. Ltd.: Singapore, 2010.
2. Macosko, C. W., *Rheology Principles, Measurements, and Applications*. Wiley-VCH: New York City, NY, 1994.
3. Lindner, P., *Neutrons, X-Rays and Light: Scattering Methods Applied to Soft Condesed Matter.* Elsevier Science: Amsterdam, 2002.
4. Kienzle, P. Neutron activation and scattering calculator. http://www.ncnr.nist.gov/resources/activation/
5. Hammouda, B. Probing Nampscale Structures –The SANS Toolbox. http://www.ncnr.nist.gov/staff/hammouda/the_SANS_toolbox.pdf
6. Glinka, C. J.; Barker, J. G.; Hammouda, B.; Krueger, S.; Moyer, J. J.; Orts, W. J., The 30 m small-angle neutron scattering instruments at the National Institute of Standards and Technology. *Journal of Applied Crystallography* 1998, 31, 430-445.
7. *Instruction Manual SAXSess Small-Angle X-Ray Scattering System*. Anton Paar GmbH: Graz, Austria, 2010.
8. Kline, S. R., Reduction and analysis of SANS and USANS data using IGOR Pro. *Journal of Applied Crystallography* 2006, 39, 895-900.
9. Egerton, R. F., *Physical Principles of Electron Microscopy*. Springer US: 2005.
10. Wall, J. S.; Hainfeld, J. F., mass mapping with the scanning-transmission electron-microscope. *Annual Review of Biophysics and Biophysical Chemistry* 1986, 15, 355-376.

Chapter III

Effects of Supersaturation on the Structure and Properties of Poly(9,9 Dioctylfluorene) Organogels.

In this study we explore the gelation behavior of poly(9,9 dioctylfluorene) (PFO) in various organic solvents using rheology and small angle neutron scattering (SANS). The gelation of PFO has been previously studied in solvents such as methylcyclohexane and toluene. Scattering and spectroscopy techniques were primarily used to study gelation kinetics in these systems[1-6]. In these works, the small angle scattering of the PFO-solvent system transitions from a power-law dependence with an exponent of -1 for the fully-dissolved polymer solutions, to a -2 power-law exponent in the crystallized/gel state[5]. This change hints to an evolution of the polymer conformation from stiff rod-like polymer chains to sheet-like structures[5, 6]. The presence of the sheet polymer conformation is corroborated using UV-Vis absorption spectroscopy by the existence of a characteristic absorption peak at 437 nm[2]. It has been previously shown that these sheets facilitate the gelation of the PFO system[4]. However recent studies show that the abundance of this phase is small compared to the quantity of the overall polymer aggregates and the crystalline domains are trapped within amorphous macroscopic aggregates[3]. The present work studies the changes occurring in the mesoscopic structure

of PFO gels as a function of variations in the solution conditions in which they are formed. The main focus of the study is to systematically explore differences over rheological, and structural properties produce by controlling the driving force of aggregation.

Experimental Methods.

Materials.

Poly (9,9 dioctylfluorenyl-2,7-diyl) (PFO) is purchased from Sigma Aldrich (St Louis, MO). The polymer has a molecular weight of 35,500 g/mol and a PDI of 2.6, as measured by GPC using polystyrene standards. The hydrogenated solvents, toluene, o-dichlorobenzene, dodecane, m-xylene, and mesitylene, are purchased from Sigma Aldrich and are used as received. Fully deuterated solvents, used in neutron scattering experiments, are purchased from Cambridge Isotopes (Andover, MA) and are also used as received. The concentration of all solutions is kept at 30 mg of PFO per 1 ml of solvent. In order to fully dissolve the polymer in each solvent, the mixture is agitated and heated to 85 °C. In dodecane, it was necessary to heat the sample up to 100 °C due to the poor solvent quality.

Scanning Transmission Electron Microscopy (sTEM).

A FEI (Hillsboro, OR) Tecnai G3 F20 transmission electron microscope (TEM) is used for scanning transmission electron microscopy (sTEM). The samples are prepared by adding 0.5 ml of the fully dissolved PFO mixtures into a capped glass vial for gel formation. To form the gels, samples containing m-xylene, toluene and mesitylene are left in the freezer at -20 °C overnight. Samples in o-dichlorobezene where formed in a

Peltier dry bath set to -15 °C overnight. Dodecane, which is a very poor solvent for PFO, is allowed to form gels at 25 °C also overnight. In order to mount samples on TEM grids, 2 ml of each solvent is added after gelation into corresponding vials and the sample is subsequently fractured by agitation. A drop of the fractured fluid dispersion is then deposited on an ultrathin, TEM copper grid with carbon support (Ted Pella, Redding, CA), and it is allowed to dry overnight before analysis.

Small Amplitude Oscillatory Rheology.

An Anton Paar (Ashland, VA) MCR 301 stress controlled rheometer is used with a parallel plate geometry of 25 mm in diameter and 0.4 mm gap between the plates. The gelation of the solutions is tracked while applying a sinusoidal strain of amplitude 0.1% at a constant frequency of 1 Hz. Under these conditions, all samples are well within the linear viscoelastic regime when the gel is fully formed [supplemental information]. The temperature of the sample is accurately controlled with Peltier devices on both plates. The samples are loaded, into the rheometer immediately after heating so that the polymer is in a fully dissolved fluid state. The rheometer plates are also pre-heated to a temperature that is high enough for the gel to not form instantaneously upon contact (i.e. 60 °C for dodecane samples and 25 °C for all other solvents). To prevent sample evaporation, an immiscible perfluorinated solvent Fomblin Y LVAC 25/6 from Sigma-Aldrich (St Louis, MO) is placed around the entire circumference of the plates sealing all of the exposed edges of the samples. The sample is then quickly quenched, using a rate of approximately 15 °C/minute, to the desired final temperature (-20 °C for toluene, m-xylene, mesitylene; -15 °C for o-dichlorobenzene; and various temperatures for dodecane). For PFO dissolved in dodecane, the samples are heated to 100 °C for 1 minute

immediately after loading, in order to ensure that they are fully dissolved before quenching and commencing the experiment.

Small Angle Neutron Scattering (SANS).

Small angle neutron scattering (SANS) experiments are performed at the Center for Neutron Research at the National Institute of Standards and Technology (NIST) in Gaithersburg, Maryland. The SANS experiments are performed using both the NG3 and NG7 instruments. SANS is performed using a standard configuration to cover a wide range of wavevector values ($0.002 < q < 0.3$ Å^{-1})[7], using wavelengths of 5.5, 6 and 8.09 Å. The data is reduced and corrected by accounting for background radiation and scattering from the sample cell. The data is also normalized to an absolute scale by measuring the incident neutron flux[8]. In addition, ultra-small angle neutron scattering (USANS) experiments are performed using the perfect crystal diffractometer BT5 at the NIST-NCNR[9]. This increases the total q range to $3x10^{-5}$ Å^{-1} so that micrometer sized features can also be probed. For each measurement, the samples are taken directly from the SANS instrument (NG3 or NG7) and placed into BT5 so that identical and fully equilibrated structures are probed. Samples for neutron scattering are prepared by loading the fully dissolved polymer (hot) into a demountable titanium cell. The solution is then heated again inside the cell in order to fully re-dissolve the sample. Mixtures of PFO in d-xylene, and d-toluene are allowed to gel overnight at -20 °C while the sample in o-dichlorobenzene is allowed to gel overnight at -15 °C to prevent freezing of the solvent. Five samples of PFO in d-dodecane are also allowed to gel overnight at 25°C, 32 °C, 40 °C, 50 °C and 60 °C. Gels formed in d-dodecane mixtures are exposed to the beam at the same temperatures in which they are formed. All other samples are run at 20 °C. All

USANS measurements are performed at room temperature. Reduction of the data is performed using the standard NIST Igor-based macros[8]. Analysis and model fitting is also performed using the NIST Igor-based analysis software and the DANSE SansView software[8]. The models, fitted to the data, are modified to account for the different collimation of the systems using the tools available in the software packages. Corrections for incoherent scattering are also performed by assuming that, at the largest measurable scattering vectors ($q > 2$ Å^{-1}), the scattering intensity is dominated by a flat incoherent background signal.

Poly(9,9 Dicotylfluorene) Gel Formation.

The driving force for conjugated polymer (CP) self-assembly is the strong π- π interactions along the backbone. These interactions cause the polymer strands to stack with each other, and eventually become fibrillar, or sheet-like structures depending on the polymer's properties (as will be later discussed in chapters II and III). At high enough concentrations (3-5 wt%), the polymeric domains grow to form a network of interconnected fiber or sheets. These networks trap solvent within the polymer-rich regions, giving the sample a gel-like behavior at the macroscopic level.

For the present study, the gelation behavior of poly(9,9 dioctylfluorene) (PFO) (Sigma Aldrich, St Louis, MO) is probed. Gelation is achieved by dissolving the polymer in a good solvent and then shifting the quality of the solvent in order to induce self-assembly. The solvent quality shift is done by heating the sample to 80ºC and then cooling it down, thus forming the gel. The temperature of gelation and cooling rates were changed based on the instrument and property probed.

PFO has a molecular weight of 35,500 g/mol and a PDI of 2.6, as measured by GPC using polystyrene standards. The hydrogenated solvents, toluene, o-dichlorobenzene, dodecane, m-xylene, and mesitylene, (Sigma Aldrich) are used as received. Fully deuterated solvents, used in neutron scattering experiments (Cambridge Isotopes, Andover, MA) are also used as received. The concentration of all solutions is kept at 30 mg of PFO per 1 ml of solvent. In order to fully dissolve the polymer in each solvent, the mixture is agitated and heated to 85 °C. In dodecane, it was necessary to heat the sample up to 100 °C due to the poor solvent quality.

Poly(9,9 Dioctylfluorene) Gels.

The solvents used in this study cover a wide range of solvent quality for PFO. Toluene, m-xylene, mesitylene, and o-dichlorobenzene are relatively good solvents and solutions need to be cooled to very low temperatures to induce gelation. In order to gel within the time frame of 24 hours, these samples need to cool down to at least -20 °C; otherwise the gels take several days to form. In contrast, samples dissolved in dodecane only require temperatures below 60 ºC to form stiff gels. Our studies show that fast gelation is generally observed in simple alkane solutions at modest temperatures while a very slow gelation is observed in aromatic solvents where temperatures need to be substantially lower. The gelation kinetics of PFO dissolved in different aromatic solvents also varies significantly depending on the functional groups that are attached to the aromatic rings. Functional groups, such as chlorine (o-dichlorobenzene), nitrogen (pyridine) or sulfur (thiophene), result in gelation at higher temperatures and in shorter periods of time when compared to aromatics having simple alkane-functional groups (toluene, xylenes, mesitylene).

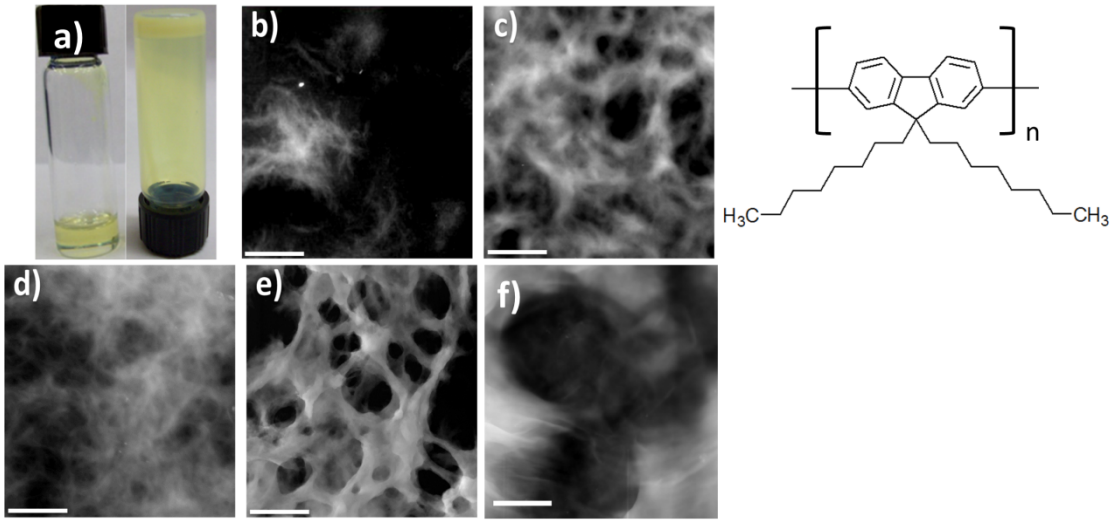

Figure 3.1: a) Photograph of a 30 mg/ml PFO, in m-xylene, system before and after gelation. sTEM images of PFO structures formed in b) toluene, c) m-xylene, d) mesitylene, e) dodecane, f) o-dichlorobenzene. Scale bars are 2 µm. All samples are gelled overnight and fractured in order to mount on the TEM grids. Additional sTEM images of all the systems can be found on the supplemental information. The chemical structure of PFO is also shown.

Figure 3.1 a) shows a picture of a typical sample of PFO dissolved in m-xylene before and after gelation. Upon gelation, samples typically become cloudy and opaque due to increased light scattering indicating the formation of large structural features. Figures 3.1b-f) show sTEM images of PFO gels formed in toluene, m-xylene, mesitylene, dodecane and o-dichlorobenze respectively, the gels are all prepared as indicated in the method section. These images clearly reveal different structures formed by the same polymer when it is gelled in different solvents. Samples gelled in toluene and mesitylene (3.1b and d) appear to be formed from the agglomeration of very small fibers that frequently form larger spherulItic domains. The structure of gels formed in m-xylene (3.1c) and dodecane (3.1e) and o-dichlorobenzene (3.1f) appear to be formed by sheets

and, in these cases, larger pores are formed. Additional sTEM images are also provided in the supplemental information.

Rheological Behavior of Poly(9,9 Dioctylfluorene) Gels.

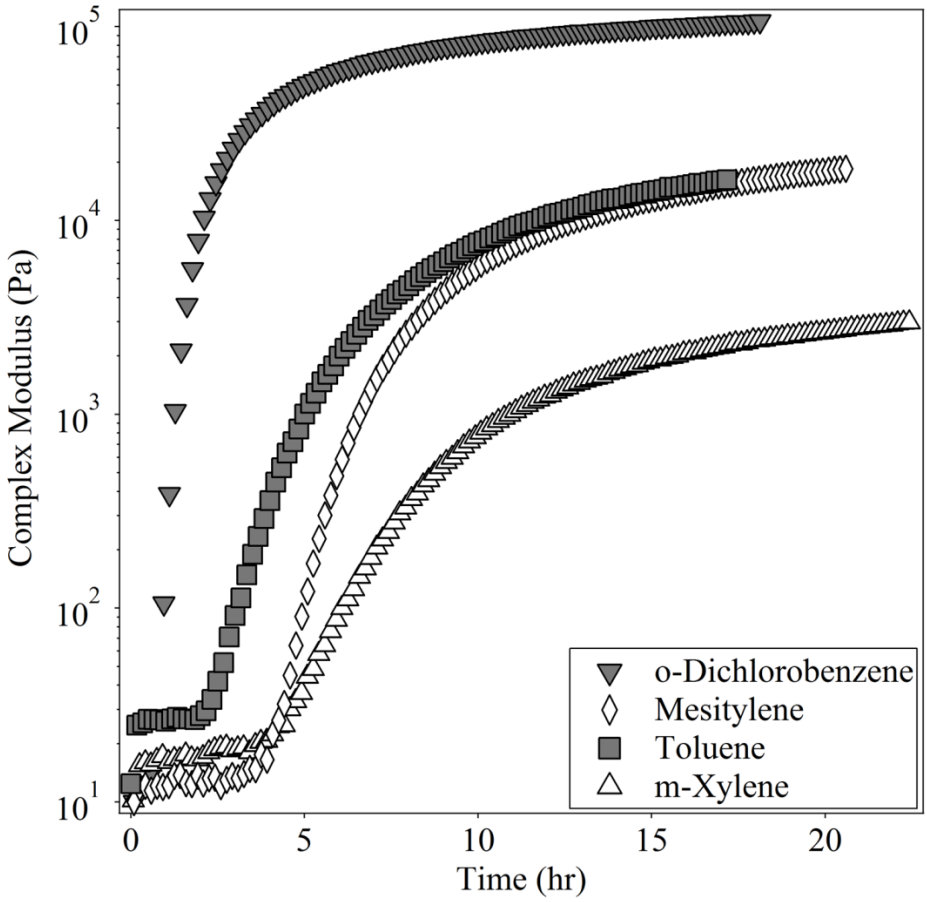

Figure 3.2: Comparison of gelation kinetics of PFO in different aromatic solvents. The temperature is held constant in each run at -20 °C for the gel formed in m-xylene, mesitylene and toluene and at -15 °C for o-dichlorobenzene.

Figure 3.2 shows the gelation kinetics of PFO in different solvents and the change in complex modulus (G*) that is observed as a function of time (for frequency and strain sweeps of the system, that shows the samples gel behavior and their linear viscoelastic regime, please refer to appendix A). The increase in complex modulus is caused by the aggregation of polymer chains to form interconnected nanoscale domains that can transduce stress throughout the sample. From this data, it is clear that o-dichlorobenzene is the worst aromatic solvent for PFO because gelation occurs the fastest, within one hour from the beginning of the run, even though it is held at a higher temperature (-15 ºC) than the other aromatic solvents (-20 ºC). Toluene appears to be the next poorest solvent followed by mesitylene, which has a gelation time that is very similar to m-xylene. However, as gelation progresses, the complex modulus of the mesitylene sample increases above that of m-xylene and it eventually matches the complex modulus of the sample formed in toluene. Gels can be stronger either because a larger percentage of polymer chains aggregate to form fibers in the network, or because stronger connections are formed between these domains.

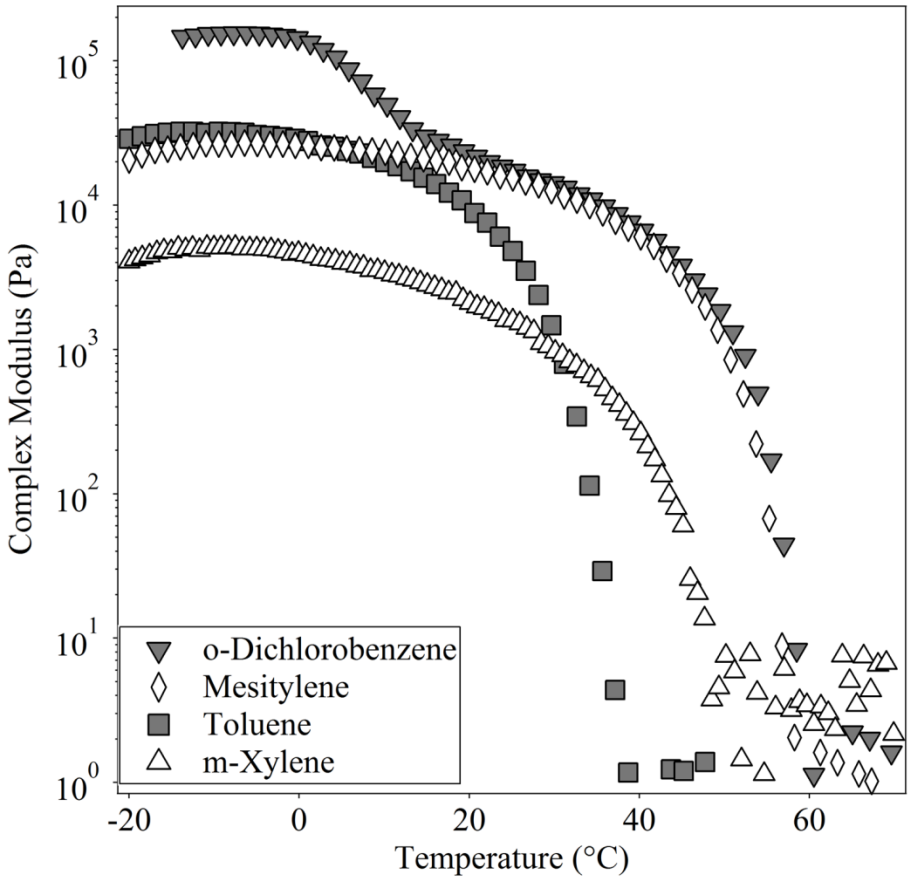

Figure 3.3: Dissolution curves for PFO gels formed in different solvents at -20 °C for mesitylene, toluene and m-xylene and -15 °C for o-dichlorobenzene. The heating rate is 1ºC/min.

Figure 3.3 shows gel dissolution curves (heating) for the PFO organogel samples that are formed in different aromatic solvents. The heating data also suggests that o-dichlorobenzene is the worst solvent because it requires temperatures in excess of 60 ºC for the gel to fully dissolve. Samples formed in mesitylene also require high temperatures to fully dissolve the polymer. In contrast, samples formed in m-xylene only require approximately 50 ºC to fully dissolve. PFO organogels formed in toluene show the smaller hysteresis, since they are among the fastest forming gels and dissolve at the lowest temperature (T_{dis} ~ 40 ºC). When all of these samples are heated from their low

gelation temperature to room temperature (~25ºC), the gels retain a significant amount of elasticity suggesting that the network structures are largely maintained. In the case of o-dichlorobenzene, there is an evident two-step decay of the complex modulus that does not appear in any of the other solvents. This observation is fully reproducible but, at this time, we are unable to fully explain the nature of the first transition step. It is presumed that the second step is related to the same dissolution process that PFO gels undergo in the other solvents.

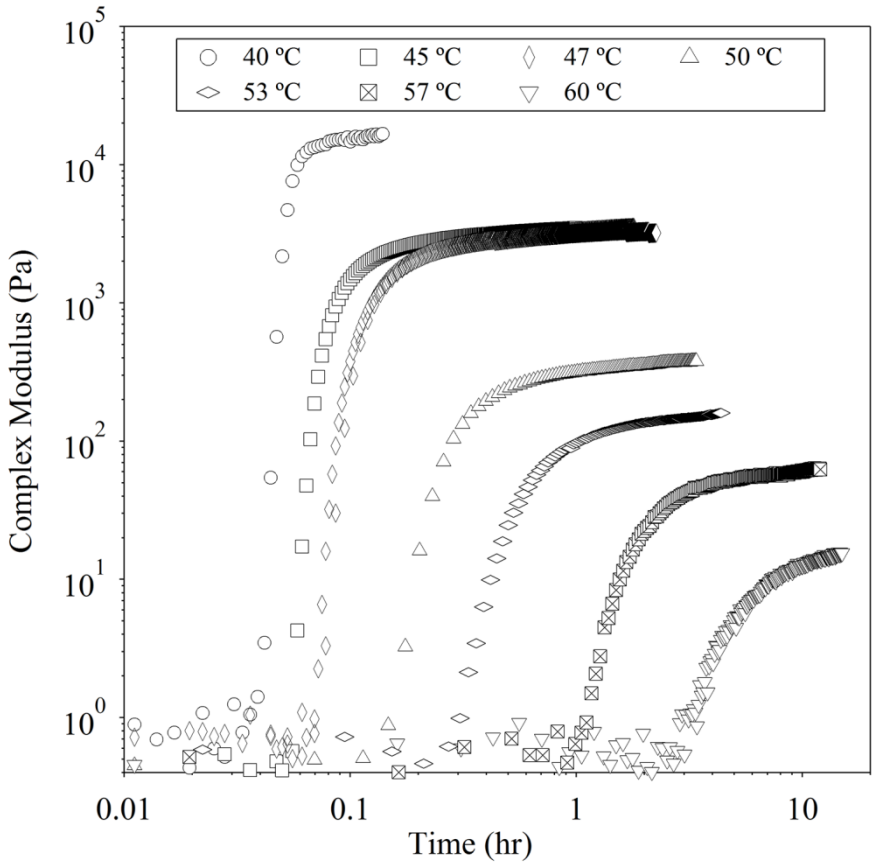

Figure 11: Complex modulus (G*) of PFO samples formed in dodecane, gelled isothermally at different temperatures.

Using a similar approach, the gelation of PFO at different temperatures is also analyzed using small amplitude oscillatory rheology. We take advantage of the poor solvent quality of dodecane to induce gelation of PFO over a range of temperatures (40 to 60 ºC) in order to probe the evolution of the gel structure at different levels of supersaturation. Figure 3.4 shows the gelation runs of PFO in dodecane. At low temperatures, the onset of gel formation occurs over a few minutes due to the high driving force for inducing gelation (i.e. high supersaturation of the system). As the temperature increases, the onset time systematically decreases to the range of several hours due to the lowering of the degree of supersaturation. Figure 3.5 shows that the behavior of the complex modulus of the systems is also very similar when probing at much lower perturbation frequencies (0.01 Hz), indicating that the gelation of the system is independent of the perturbation frequency of the measurement The temperature that is used to drive the aggregation also affects the final elasticity of the gels (G*) after gelation is complete. Weaker gels are formed at higher temperatures or lower levels of supersaturation. Similar behavior is also observed with samples formed in different solvents (Figure 3.2). In general, the systems that gel faster are also the ones forming the stronger gels.

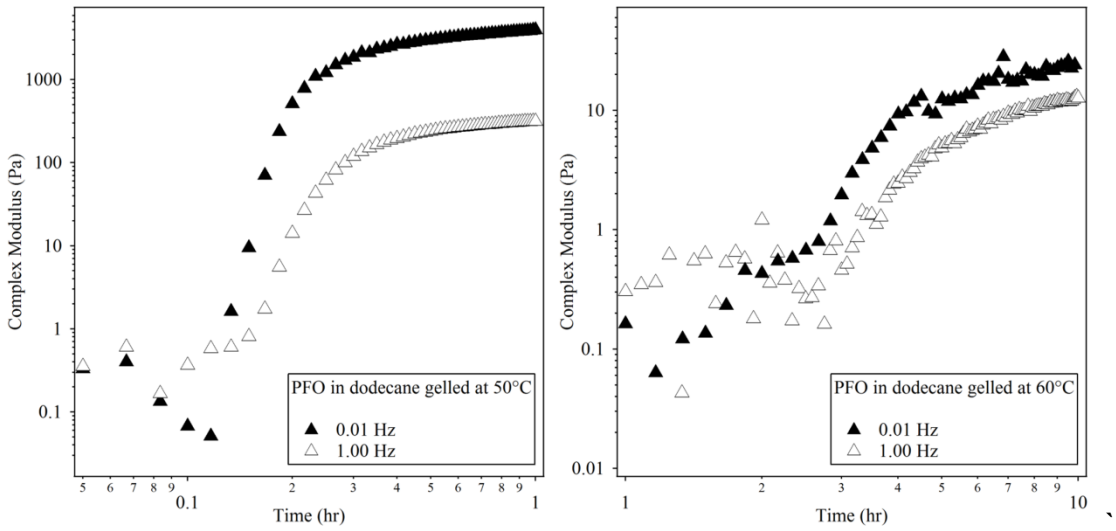

Figure 3.5: Gelation kinetics of a PFO dodecane system produced at two different temperatures: left 50°C, right 60°C. The gelation kinetics of these samples is probed using two different perturbation frequencies, 0.01 and 1 Hz. The time of gelation is basically the same at both probe frequencies. However, the maximum complex modulus increased at lower frequencies for both temperatures.

Small Angle Neutron Scattering of Poly(9,9 Dioctylfluorene) Gels.

Figure 3.6 shows the USANS scattering profile for the PFO gels formed in different solvents and at different temperatures. At low q, the scattering experiment probes the larger features of the network structure. In this q-range, a Guinier plateau region appears for all the gels indicating that a characteristic structural feature of micrometer size is present in all samples. However, the sample of PFO that is gelled in dodecane at room temperature also shows a second uptake after the Guinier region that does not appear in any other sample. A fit to the Guinier equation (equation 3.1) is applied to all samples over this portion of the profiles[10].

$$I(q) = \phi \Delta\rho^2 \exp\left[\frac{-q^2 R_g^2}{3}\right] \quad \text{(Eq. 3.1)}$$

The radius of gyration (R_g) characterizing the largest features of the PFO networks is obtained from this analysis and the results are included in Table 3.1 for the different solvent samples. A trend is observed of increasing feature size for the aggregates formed at higher supersaturation (i.e. decreased R_g as gelation temperature decreases).

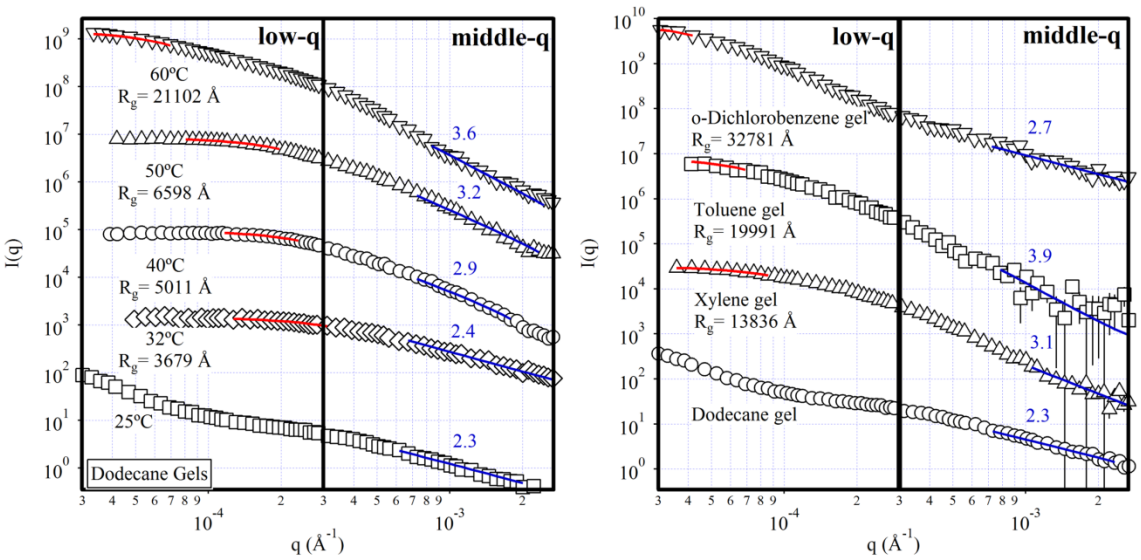

Figure 3.6 Left: USANS profiles (smeared) of the PFO gels formed at different temperatures in d-dodecane. Right: USANS profiles corresponding to the samples formed in different solvents; d-toluene (-20 °C), d-xylene(-20 °C), o-dichlorobenzene (-15 °C) and d-dodecane (25 °C). The solid lines correspond to fits to the Guinier equation and the values of R_g are also provided. Curves are shifter vertically for added clarity.

Power-law dependencies (i.e. linear region in log-log plot) also appear in the q-range corresponding to 6.0×10^{-4} to 4.0×10^{-3} $Å^{-1}$ (middle-q region) for all PFO gel samples

with exponents ranging in value from -2.3 to -3.6 (figure 3.6 and 3.7). These values are characteristic of sharp interfaces being formed in the samples between regions with clearly different values of scattering length density. This suggests that the networks (polymer-rich regions) can be well segregated from polymer-poor solvent regions between them (i.e. a heterogeneous polymer distribution) and that this segregation varies with solvent and conditions used for gelation[11]. There is a clear trend of decreasing power-law exponent as the supersaturation of the system increases. For example, there are higher power-law exponents when the temperatures increase in dodecane gels and the exponents of the PFO gels formed in o-dichlorobenzene are also smaller than those of gels formed in m-xylene. All power-law exponent values are also listed in table 3.1.

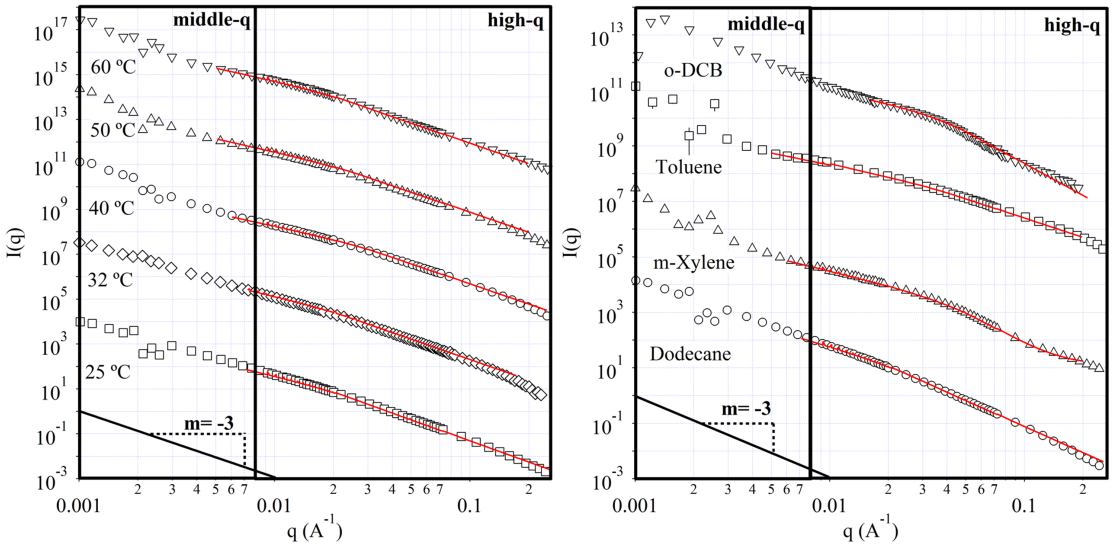

Figure 3.7: Left: SANS scattering profiles of the gels formed at different temperatures in d-dodecane. Right: profiles corresponding to the samples formed in different solvents. The solid, red lines are fits obtained from the Guinier-Porod model. The parameters obtained from these fits are listed in Table 3.1.

Over the SANS q-range of $4x10^{-3}$ and $5x10^{-2}$ $Å^{-1}$ (high-q), the formation of a characteristic 'knee' is evident in all the gel samples (figure 3.7). This 'knee' is also observed in P3HT organogel samples and it can be related to the cross-sectional geometry of the building blocks of the networks (e.g. nanofibers or nanosheets). The q dependence of the scattering in this region generally fluctuates from power-law exponents of -3 to -2. At the lower end, this can be characteristic of the organization of PFO polymer chains into sheet-like two-dimensional structures[5, 6]. However, fractal network structures are also know give power-law exponents in this range. Finally, at high-q the scattering intensity rapidly decreases toward zero after the incoherent background is subtracted as discussed in the experimental section.

The model use to analyze the data in the high-q region (0.07 $Å^{-1} < q < 0.2$ $Å^{-1}$) is the Guinier-Porod model. This shape-independent form factor is used to analytically obtain the dimensionality and characteristic length scale of asymmetric objects that are characterized by a smooth transition from a Guinier region to a Porod region[12].

The Guinier-Porod model uses the following form factors:

$$I(q)\begin{cases}\phi\Delta\rho^2 \exp\left[\dfrac{-q^2R_g^2}{3-s}\right] & \text{for } q \le Q_1 \\ \dfrac{D}{q^m} & \text{for } q \ge Q_1\end{cases} \qquad \text{(Eq. 3.2)}$$

where ϕ is the volume fraction of the polymer, $\Delta\rho$ is the difference in scattering length density (solvent vs. domain), R_g is the radius of gyration of the system, s is a dimensionality parameter, and m is the slope at high q. D and Q_1 are defined as follows:

$$D = \phi \Delta \rho^2 \exp\left[\frac{-Q_l^2 R_g^2}{3-s}\right] Q_l^{(m-s)} \qquad \text{(Eq. 3.3)}$$

$$Q_l = \frac{1}{R_g}\sqrt{\frac{(m-s)(3-s)}{2}} \qquad \text{(Eq. 3.4)}$$

By defining Q_l as shown in equation 3.4, the continuity of the Guinier and Porod functions and their slopes is enforced. The incoherent background is subtracted from the data before fitting with equation 3.1.

The dimensionality parameter *s* is used to estimate the dimension of the primary scattering objects. The parameter *s* modifies the standard Guinier formula so that it is also possible to fit asymmetric objects such as rods and platelets[13]. When *s*=0 the standard Guinier formula is recovered, indicating objects with a globular or 3-D structure. If *s*=1, the model indicates the presence of rods, and lamellar structures for *s*=2. It is important to point out that this model is still valid for intermediate shapes between spheres and rods, and between rods and platelets[8].

Table 3.1: Parameters obtained from the fits to the neutron scattering data.

Table 3.1:	o-Dichlorobenzene	Toluene	m-Xylene
R_g from Guinier-Porod model	2.7 ± 0.1	1.9 ± 0.1	2.1 ± 0.1
High-q Power Law Exponent [m]	3.8	2.3	3.8
Dimensional Parameter [s] [10]	1.5	1.4	1.7
Low-q Power Law Exponent	2.7	3.9	3.1
Network R_g (nm)	3278 ± 132	1999 ± 101	1383 ± 34

Dodecane					
Temperature	25 °C	32 °C	40 °C	50 °C	60 °C
R_g from Guinier-Porod model (nm)	3.1 ± 0.1	3.0 ± 0.1	2.2 ± 0.1	2.6 ± 0.1	3.3 ± 0.1
High-q Power Law Exponent [m]	3.1	3.0	3.0	2.9	3.0
Dimensional Parameter [s]	2.0	2.0	1.9	1.9	1.9
Low-q Power Law Exponent	2.3	2.4	2.9	3.2	3.6
Network R_g (nm)	N/A	367 ± 19	501 ± 10	659 ± 8	2110 ± 16

Supersaturation Effect on the Structure and Properties of the Poly(9,9 Dioctylfluorene) Gels.

Controlling the driving force for aggregation of PFO strands is achieved by using different solvents or by allowing gel formation to occur at different temperatures. The sTEM images (figure 3.1) show marked differences in the morphology of the resulting samples. The neutron scattering results (table 3.1) also validate the differences of the micron-scale morphology for gels formed with different gelling conditions. The samples also present different rheological behavior at the different supersaturation levels. The gels formed at a high level of supersaturation have a higher modulus than the ones formed at lower levels. This may be due to more polymer chains going from the dissolved state into the aggregated state or to a change in the morphology of the networked domains. The fraction of dissolved polymer that remains after gelation is also measured by adding solvent to a gelled sample, physically breaking the gel, centrifuging the solids out and performing spectroscopic analysis of the remaining dissolved material. UV-vis absorbance is used to estimate how much polymer remained dissolved after gelation under different conditions. We find that virtually all the polymer is aggregated in all samples independently of the conditions at which the gel is formed. Therefore, the differences in rheological properties are most likely due to the different conformation of the polymers in the networked structures and not to differences in the number of chains that are gelled.

In order to better quantify the effect of supersaturation on the kinetics of gel formation, a model derived by Liu and coworkers using Avrami theory of phase change is applied to the rheological data of the different PFO organogel systems [14].

$$X_{cr}(t) = \frac{G(t) - G_0}{G_f - G_0} \quad \text{(Eq. 3.5)}$$

Equation 3.5 relates the extent of aggregation X_{cr} (i.e. how far gelation has progressed from the initial dissolved state) using the temporal evolution of the complex modulus $G(t)$. G_0, and G_f correspond to the initial and final complex modulus respectively. The value of G_f is assumed to be the complex modulus when it has stopped from evolving in any meaningful way, at this point the sample is assumed to be fully developed. This method has been previously used to quantify the effect of solvent quality on the self-assembly of P3HT organogels[15].

By monitoring the isothermal change over time, we obtain parameters describing the kinetics of network growth using equation 3.6, where t_g is the onset time of gelation, k^o is the rate growth constant and D_f is the fractal dimension of the system.

$$\ln\left[1 - X_{cr}(t)\right] = -k^{\circ}\left(t - t_g\right)^{Df} \quad \text{(Eq. 3.6)}$$

From the rheology, the parameters t_g, G_0, G_f are known and, by using these values to constrain the fit, it is possible to obtain a value for the fractal dimension (D_f). A D_f of 1 indicates that the networks are growing at a characteristic rate corresponding to one-dimensional aggregates (i.e. straight fibers). Values ranging between 1-2 indicate bifurcated or branching fiber growth, between 2-3 indicate spherulitic or sheet-like

structures, and a D_f value of 3 indicates that the system is growing at an equivalent rate in all directions (i.e. 3-dimensional growth).

Figure 3.8 shows the fits to the kinetic model using the rheological data. The parameters obtained from the fits indicate that the system with the highest fractal dimension is o-dichlorobenzene gel (2.49), followed by mesitylene and toluene PFO samples (2.18 and 2.19), and finally the gel formed in m-xylene (1.89). These results show an inverse correlation of this fractal dimension with solvent quality. It is important to point out that these fractal dimensions are also more correlated to the maximum storage modulus of the system than to the onset time for gelation (Figure 3.2). The same trend can also be observed for the variable temperature experiments. As dodecane becomes a better solvent for PFO (i.e. by raising the temperature), the fractal dimension obtained from rheology steadily decreases (Figure 3.8).

The nanostructure of the gel is also affected by the extent of supersaturation. Previous work has shown a drastic change in network structures formed by P3HT in different solvents[16]. The sTEM images also reveal important structural differences of PFO aggregates in different solvents. There is also general consistency between the sTEM images (Figure 3.1) and the rheological behavior of the samples (Figure 3.2). Dodecane samples, at room temperature, appear to be the strongest of the gels, and on the sTEM images they appear to be formed out of thicker networked domains. The complex modulus of all dodecane samples are reported at temperatures that are way above room temperature and, despite this, they are still comparable with the modulus of the gel samples formed in other solvents. Gels formed in mesitylene and toluene appear to be composed of very similar structures, and they both present a comparable complex

modulus. In contrast, the structure of PFO gels formed in m-xylene does not resemble any of the other samples, even though the complex modulus has similar values (Figures 3.1 and 3.2). Furthermore, out of all the aromatic solvents, gels formed from o-dichlorobenzene are stronger and result in more dense sheet-like structures. Since sTEM requires removal of solvent and it cannot characterize the smallest features of the gels, we use SANS and USANS to explore variations in the structure of the gels without altering its natural state.

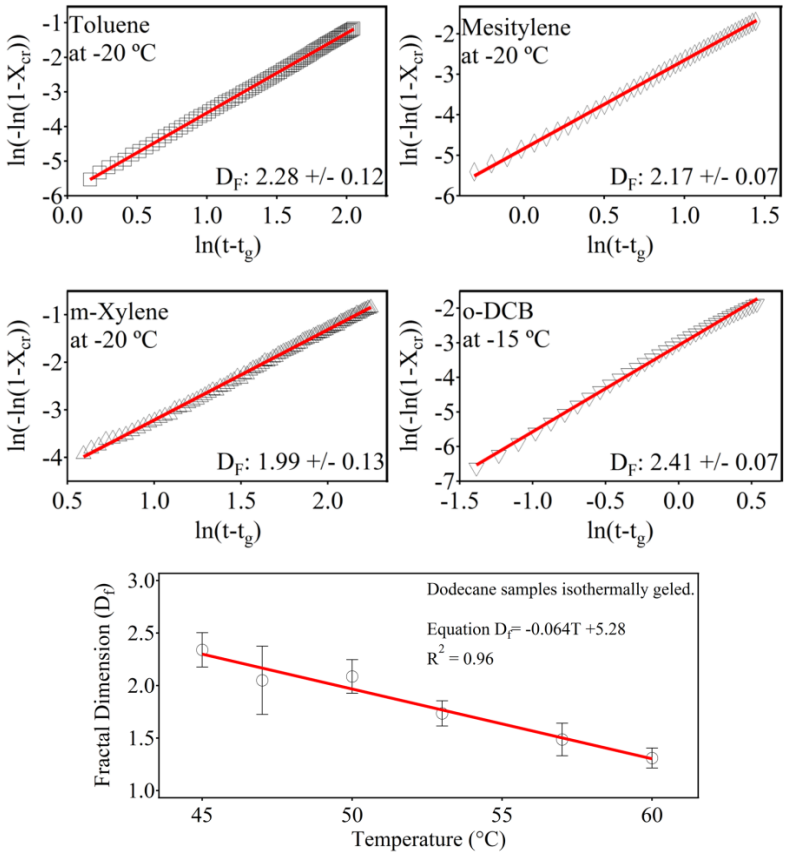

Figure 3.8: Top graphs: Representative Avrami curves for each of the aromatic solvent systems. The solid red lines are the fits obtained using Liu's model for gelation. Bottom graph: Fractal dimension as a function of temperature for dodecane gels. The fractal dimension was obtained by fitting Liu's model to the data.

In order to obtain the scattering profile of the structure of fully developed gels, the samples are maintained at their respective gelation temperatures (o-dichlorobenzene - 15°C, toluene and m-xylene -20°C, dodecane at various temperatures) for at least 12 hours. This amount of time ensures that the gel is close to be fully developed as indicated by figures 3.2 and 3.4, since the complex modulus of any the systems does not increase much more after that amount of time has passed. The Guinier region in the USANS regime (figure 3.6) reveals structures formed at micron-sized length scales. Based on the similar length scales, these are also the larger features (i.e. phase separation) that are observed in the sTEM images. In the temperature study (figure 3.6 left), there is a clear trend of the Guinier plateau to shift to lower q as the temperature is raised. This means that there are larger features formed when the supersaturation of the system decreases. This can be explained by the decrease in number of growing nucleation centers due to the lower driving force for aggregation. The decreased growth rate also leaves more polymer chains available to increase the size of the few growing network domains. At lower temperatures (higher supersaturation), many more nucleation centers grow in parallel and trap more polymer chains leading to the formation of denser but also smaller domains. In samples formed in different solvents (figure 3.6 right) the opposite trend appears to occur. When the supersaturation of the sample is lower, based on gelation time (rheology), smaller network domains are created. This suggests that specific solvent-polymer interactions may also be present and could greatly influence the structure of the resulting organogels.

The Guinier region at low q is followed by a power-law region for all the samples (figures 3.6 and 3.7, $\sim 3 \times 10^{-4} < q < 4 \times 10^{-3}$ Å^{-1}). The magnitude of the power-law

exponent in this region (i.e. the slope in the log-log plot) is found to be inversely proportional to the supersaturation level of the system for both the temperature and the solvent studies. A higher slope (closer to -4) indicates a clear network-solvent interface is present in the samples. This is possibly explained by considering the aggregation of 2D sheet-like domains. At high supersaturation this process is very chaotic and fast, causing a more disordered stacking of the polymer domains (bottom panels in figure 3.9). In contrast, at low supersaturation the aggregation process is slower allowing the polymer to stack more effectively and to grow into longer networked domains (top panels in figure 3.9).

At high q, the scattering describes the shape of the smallest building blocks in the network. In order to quantify the effect of supersaturation on PFO organogels, a form factor model is used to fit the scattering profiles in this region. We also note that form factors of different shapes (i.e. lamellar, parallelepiped, flexible elliptical cylinder) did not accurately describe the scattering profiles for any of the gels. The sTEM images also do not provide an adequate insight into the shape of the smallest building blocks because of the lack of sufficient resolution to adequately probe the polymer conformation at these length scales. For these reasons, a shape-independent form factor is used to fit the scattering profiles of the different organogel samples. The Guinier-Porod model is chosen for this purpose[8]. This way it is possible to quantify and compare the difference of the shape of polymer aggregates formed under different gelation conditions.

Figure 3.7 shows the scattering data for all 8 samples with their corresponding fits. The parameters obtained from these fits are also listed in table 3.1. It is obvious from the results that neither solvent nor temperature significantly affects the radius of gyration

of the smallest building blocks in any meaningful way. This parameter stays constant between 2 and 3 nm for all the samples, even when a wide range of supersaturation is used. The constant value for this parameter is also consistent with a characteristic length that is likely controlled by the molecular properties of the polymer such as the contour length or the characteristic thickness of polymer strands that are stacked together. Similar observations are also made on a P3HT system, where the width and thickness of the fiber does not change with the solvent choice or solid concentration[15]. This suggests that the shapes and sizes of the organogel building blocks heavily depend on the polymer molecular characteristics.

The dimensionality parameter (s) approaches 2 for most of the samples. As explained previously, a dimensionality of 2 indicates the presence of sheet-like or lamellar structures. This is consistent with previous SANS studies performed on the PFO system[5, 6]. However, as the supersaturation of the system is lowered in the solvent study, this dimensionality parameter also shifts towards lower values. Values between 1 and 2 indicate intermediate shapes between platelets and stiff cylinders. The change in dimensionality is due to the ordered aggregation that is caused by a decrease in supersaturation. The lack of a similar shift in the temperature study once more suggests that this change is likely due to the specific influence the solvent on the polymer.

The high-q slope (figure 2.6, $0.04 < q < 0.15$ Å^{-1}) seems to also be affected by solvent choice. The value of this slope varies widely with solvent, but it again stays constant in the temperature study suggesting that it is related to specific interactions of the polymer with the solvents and not just to gelation kinetics. The slope in this region of q describes the molecular-scale polymer-solvent interface. A slope of -4 indicates a clear,

discrete, and smooth interface between a solvent and the polymer domains (Porod behavior). The deviation from the -4 slope could indicate entrapment of solvent molecules within the polymer aggregates, which increases surface roughness and causes fluctuation in scattering length density at the interface. This entrapment is likely influenced by specific solvent-polymer interactions, and therefore would vary as a function of the solvent, but not as a function of the system's supersaturation. Nevertheless, it is important to point out that there is uncertainty in some of these values because the fits do not follow this portion of the data very closely for all of the samples and the incoherent scattering obscures the data at very high q (>0.15 $Å^{-1}$).

The self-assembly of PFO chains in organic solvents is clearly driven by the supersaturation of the system. This is probed by changing both the solvent type and/or the temperature that is used to drive isothermal gelation. The effect of varying the solvent type is highly complex because it can involve specific physical and chemical interactions between the polymer and the solvent molecules that are difficult to characterize at the length scales probed with these experiments. On the other hand, the temperature study keeps these molecular interactions constant, affecting only the aggregation kinetics. When there is only one factor controlling the extent of supersaturation (i.e. temperature variation study), there is a clear trend linking the onset time of gelation t_g to the maximum complex modulus G^* (Figure 3.4). When the gels start forming earlier, the maximum complex modulus is higher. However, when there is not a complete control over all the factors driving aggregation, such as in the case of the solvent study, these trends do not always hold. For example, the gelation of PFO in mesitylene (Figure 3.2) is considerably delayed when compared to the same sample in toluene even though its

complex modulus eventually increases to a similar value. Also, the dissolution curves (Figure 3.3) do not show the same solvent quality trend as the gelation curves (figure 3.2). Finally, the radius of gyration obtained from the USANS data (figure 3.6) also does not show the same trends for the solvent experiments as it does for the temperature study. This is again likely caused by differences in the molecular interactions that develop between the different solvents and the PFO chains in each case.

Figure 3.9 illustrates the general differences found for aggregation as the supersaturation of the system changes. Several nucleation centers are created in the samples when supersaturation is high (e.g. low temperature or bad solvent). The presence of many nucleation centers that grow simultaneously and very fast inhibits the growth of well-connected network domains. The result is a high fractal dimension and a heterogeneous sample. On the other hand, low supersaturation (e.g. high temperature or good solvents) inhibits the formation of nucleation centers in the sample. This leaves more polymer chains available for growth leading to a more organized and interconnected network. Low supersaturation makes aggregation less chaotic, minimizing defects that lead to the development of bifurcations or branches in the structure. Therefore, for these samples the fractal dimension of the system approaches 1-D growth. Using these extremes as a reference, it is possible to deduce a degree of supersaturation that will promote the growth of domains (i.e. prevent the simultaneous formation of a large number of nucleation centers), but at the same time facilitate interconnection of domains to create pathways for charge transport.

The different PFO-solvent systems are characterized by the schematic description shown in figure 3.9. At high supersaturation (i.e. higher driving force of gel formation),

the shift of the Guinier plateau to higher-q (figure 3.6) indicates the presence of smaller subdomains. As the supersaturation of the system decreases (i.e. lowering the driving force of aggregation) the power law exponent at low-q systematically approaches -4 and the formation of larger subdomains is evident in R_g. The rheological analysis also supports this picture of the system, by showing a trend of increasing fractal dimension as the system's supersaturation increased (figure 3.9). Low fractal dimension and larger domains are expected for ordered 1-D growth while high fractal dimension and small domains are expected for fast and chaotic growth.

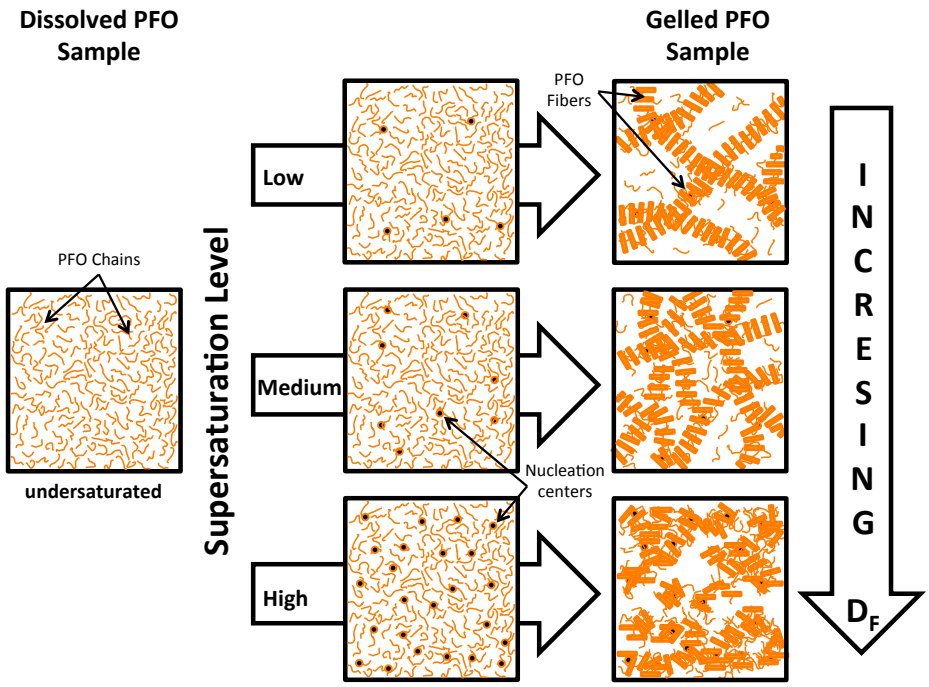

Figure 3.9: Schematic description of the network conformations at different supersaturation levels. At low supersaturation (top) there are fewer nucleation centers formed. At high supersaturation (bottom) there is a high density of nucleation centers and fast growth causing the polymer to disorderly aggregate.

When the conductivity of the sol and gel systems is measured, it turned out to be lower than the resolution of the instrument (Agilent E4980A Santa Clara, CA). Figure 3.10 shows that upon gelation, the conductivity of the gels did not show an increase above the instrumental noise level. This is in direct contrast to findings in other studies involving different conjugated polymers[15, 17]. This may be due to differences on the intrinsic conductivity of the polymers or differences in the type of crystallization. WAXS data of a dry PFO gel shows several crystal peaks characteristic of the α phase of PFO.[18] At the same time, the solid fraction of the PFO gels in all solvents is found to be very high so that the lower conductivity is not caused by a low fraction of PFO in the network phase[3]. This shows that aggregation and gelation of conjugated polymers does not necessarily cause a large increase in electrical conductivity. In contrast, P3HT organogels are formed from interconnected and highly crystalline nanowires (WAXS also supplemental information) leading to a drastic increase in conductivity[16]. Figure 3.3 shows a decrease in the complex modulus of fully formed gels when the temperature is raised. This implies that the gel structure fractures or breaks into smaller domains before the polymer chains fully disassociate from each other and the sample re-dissolves.

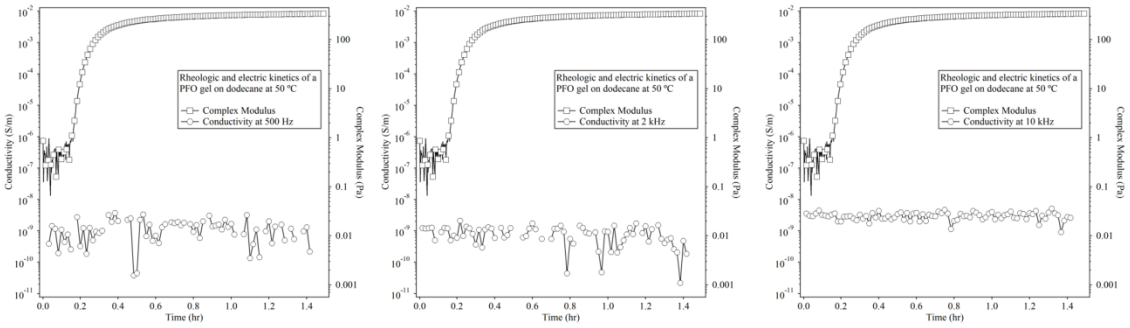

Figure 3.10: Simultaneous electrical and rheological measurements of a PFO sample in dodecane gelled at 50°C. The conductivity of the sample was tracked using round electrodes with 50 mm in diameter and a

gap separation of 0.2 mm. The voltage perturbation used was 1 V, and three different frequencies were probed 0.5, 2 and 10 kHz. The conductivity did not show any measurable change as the sample transitions from sol to gel at any of the probed frequencies.

Conclusions

The gelation of a PFO system is characterized over different degrees of supersaturation and structural and rheological properties are quantified. In order to vary supersaturation, different solvents and temperatures are used to induce gelation of the polymer. It is found that supersaturation directly affects the gelation kinetics of the system and the overall morphology and structure of the networks. This study reveals a strong dependency of the rheological properties of the samples with the gelation conditions. sTEM and neutron scattering experiments show significant differences in the structure of the larger (micron-size) network features when gels are formed in different solvents and at different temperatures. The rheological fractal dimension is clearly affected by the level of supersaturation of the system further indicating a change in the network structure. In contrast, supersaturation plays a minor role in the structure of the smallest building blocks of the networks. This is analogous to the behavior of other conjugated polymer gels (e.g. P3HT) where molecular parameters control these features. In PFO, gelation does not appear to significantly increase the conductivity of the sample. This is again contrasting to other conjugated polymer systems (e.g. P3HT).

References

1. Chen, C. Y.; Chang, C. S.; Huang, S. W.; Chen, J. H.; Chen, H. L.; Su, C. L.; Chen, S. A., Phase-Separation-Induced Gelation of Poly(9,9-dioctylfluorene) Methylcyclohexane Solution. *Macromolecules* 2010, 43, (9), 4346-4354.

2. Chen, J.-H.; Chang, C.-S.; Chang, Y.-X.; Chen, C.-Y.; Chen, H.-L.; Chen, S.-A., Gelation and Its Effect on the Photophysical Behavior of Poly(9,9-dioctylfluorene-2,7-diyl) in Toluene. *Macromolecules* 2009, 42, (4), 1306-1314.
3. Huang, L.; Huang, X.; Sun, G.; Gu, C.; Lu, D.; Ma, Y., Study of beta phase and Chains Aggregation Degrees in Poly(9,9-dioctylfluorene) (PFO) Solution. *Journal of Physical Chemistry C* 2012, 116, (14), 7993-7999.
4. Knaapila, M.; Bright, D. W.; Stepanyan, R.; Torkkeli, M.; Almasy, L.; Schweins, R.; Vainio, U.; Preis, E.; Galbrecht, F.; Scherf, U.; Monkman, A. P., Network structure of polyfluorene sheets as a function of alkyl side chain length. *Physical Review E* 2011, 83, (5).
5. Knaapila, M.; Garamus, V. M.; Dias, F. B.; Almasy, L.; Galbrecht, F.; Charas, A.; Morgado, J.; Burrows, H. D.; Scherf, U.; Monkman, A. P., Influence of solvent quality on the self-organization of archetypical hairy rods - Branched and linear side chain polyfluorenes: Rodlike chains versus "beta-sheets" in solution. *Macromolecules* 2006, 39, (19), 6505-6512.
6. Knaapila, M.; Stepanyan, R.; Torkkeli, M.; Garamus, V. M.; Galbrecht, F.; Nehls, B. S.; Preis, E.; Scherf, U.; Monkman, A. P., Control over phase behavior and solution structure of hairy-rod polyfluorene by means of side-chain length and branching. *Physical Review E* 2008, 77, (5).
7. Glinka, C. J.; Barker, J. G.; Hammouda, B.; Krueger, S.; Moyer, J. J.; Orts, W. J., The 30 m small-angle neutron scattering instruments at the National Institute of Standards and Technology. *Journal of Applied Crystallography* 1998, 31, 430-445.
8. Kline, S. R., Reduction and analysis of SANS and USANS data using IGOR Pro. *Journal of Applied Crystallography* 2006, 39, 895-900.
9. Barker, J. G.; Glinka, C. J.; Moyer, J. J.; Kim, M. H.; Drews, A. R.; Agamalian, M., Design and performance of a thermal-neutron double-crystal diffractometer for USANS at NIST. *Journal of Applied Crystallography* 2005, 38, 1004-1011.
10. Guinier, A.; Fournet, G., *"Small-Angle Scattering of X-Rays"*. John Wiley and Sons: New York, 1955.
11. Hecht, A. M.; Duplessix, R.; Geissler, E., structural inhomogeneities in the range 2.5-2500 a in polyacrylamide gels. *Macromolecules* 1985, 18, (11), 2167-2173.
12. Lindner, P.; Zemb, T., *Neutrons, X-rays and Light: Scattering Methods Applied to Soft Condensend Matter*. North Holland: Amsterdam, 2002.
13. Glatter, O.; Kratky, O., *Glatter, O.; Kratky, O*. Glatter, O.; Kratky, O: New York, 1982.
14. Li, J.-L.; Liu, X.-Y., Architecture of Supramolecular Soft Functional Materials: From Understanding to Micro-/Nanoscale Engineering. *Advanced Functional Materials* 2010, 20, (19), 3196-3216.
15. Newbloom, G. M.; Weigandt, K. M.; Pozzo, D. C., Electrical, Mechanical, and Structural Characterization of Self-Assembly in Poly(3-hexylthiophene) Organogel Networks. *Macromolecules* 2012, 45, (8), 3452-3462.
16. Newbloom, G. M.; Kim, F. S.; Jenekhe, S. A.; Pozzo, D. C., Mesoscale Morphology and Charge Transport in Colloidal Networks of Poly(3-hexylthiophene). *Macromolecules* 2012, 44, (10), 3801-3809.

17. Newbloom, G. M.; Weigandt, K. M.; Pozzo, D. C., Structure and property development of poly(3-hexylthiophene) organogels probed with combined rheology, conductivity and small angle neutron scattering. *Soft Matter* 2012, 8, (34).
18. Chen, S. H.; Chou, H. L.; Su, A. C.; Chen, S. A., Molecular packing in crystalline poly(9,9-di-n-octyl-2,7-fluorlene). *Macromolecules* 2004, 37, (18), 6833-6838.

Chapter IV

Structure-Property Engineering of Poly(3-Alkylthiophenes) Through Solvent Mixtures

The aggregation of conjugated polymers is a recurring phenomena and appears on different polymer backbones. The previous chapter described the self-assembly of Poly(9,9 dioctylfluorene) (PFO). It also described the effect of temperature and solvent choice on the structure of the aggregates. Unfortunately PFO's conductivity is too low to quantify any changes on the conductivity caused by the self-assembly. P3ATs are another family of polymer that have showed self-assembly and gelation. This family of polymer also has a higher conductivity, and therefore can be used to track the changes induced by the different self-assembly conditions.

Recently, features such as the size and crystallinity of fibers as well as the extent of branching and the orientation of the fiber network have been characterized and shown to increase conductivity on poly(3-hexylthiophene) systems.[1-4] Furthermore, it is also known that thin films made from organogels produce higher charge mobility when compared to films cast from polymer solutions.[2, 5] It has been shown that the conductivity of P3HT films can increase by several orders of magnitude when polymer gels are formed[5]. The formation of fiber networks in P3HT can facilitate charge transport by two different mechanisms. First, a coil-to-rod transition causes a substantial increase in conjugation-length of the individual polymer strands and this improves intra-chain charge

propagation. Secondly, the reduced distance between stacked polymer chains (i.e. due to pi-pi stacking) that form the fibers and nanostructures facilitates inter-chain charge hoping events that also increase charge conduction. However, despite these increases in conductivity, it has also been determined that controlling the structure and connectivity of the organogel networks is critically important to take full advantage of this approach to enhance electronic properties[3, 6].

In this work the effect of alkyl chain and supersaturation on the structure and properties of the organogels is probed. In the alkyl chain study, three P3ATs with varying chain length are used. The alkyl chain lengths used are hexyl, octyl and dodecyl. Supersaturation is controlled by changing the solvent quality of the system. In this study the solvent quality is varied by mixing a good solvent for the polymer (dichlorobenze) with a poor solvent (dodecane). The structural information of the gel is obtained using small angle neutron scattering. The mechanical and electrical properties of the gels are also measured using oscillatory rheology and dielectric spectroscopy. We demonstrate that changes in both alkyl chain length and supersaturation are effective means for the modification of structure and properties. These results represent a step forward towards controlling the self-assembly of conjugated polymer.

Experimental Methods.

Materials.

Two lots of regioregular poly(3-hexylthiophene) (P3HT), one lot of regioregular poly(3-octylthiophene) (P3OT) and one lot of regioregular poly(3-dodecylthiophene) (P3DDT) are used as received from Rieke Metals (Lincoln, NE). The molecular weight (

M_w^{chain}), polydispersity index (PDI) and regioregularity (*RR*) for all of these polymers is shown in Table 4.1. The average contour length (L_c) of the polymer is calculated using Equation 4.1 and listed in Table 4.1.

$$L_c = \frac{M_w^{chain}}{M_w^{monomer}} \cdot L_{monomer} \quad \text{(Eq 4.1)}$$

The molecular weight of a monomer unit ($M_w^{monomer}$) is 166.3 g/mol for P3HT, 194.3 g/mol for P3OT and 250.4 g/mol for P3DDT while the length of a single monomer unit ($L_{monomer}$) is constant at 1.9 Å.[25, 26]

Hydrogenated solvents 1,2-dichlorobenzene (DCB) and n-dodecane are purchased from Sigma-Aldrich (St. Louis, MO) and used as received. Deuterated solvents are used to decrease the incoherent scattering background and increase the scattering contrast in SANS and USANS experiments. D4-1,2-dichlorobenzene (D > 99%) was purchased from Cambridge Isotopes (Tewksbury, MA) and D26-Dodecane (D > 98%) is purchased from Sigma-Aldrich. Both were used as received.

Sample Preparation.

All samples are prepared by adding 30 mg/mL P3AT to a mixture of 1,2-dichlorobenzene and dodecane. Samples are then heated above 80 ºC until all visible signs of polymer powder (black) had disappeared and a bright orange solution remained. All solvent mixture percentages in this work are by weight.

Neutron Scattering.

Small Angle Neutron Scattering (SANS) and Ultra-Small Angle Neutron Scattering (USANS) experiments are performed at the National Institute of Standards and

Technology Center for Neutron Research (NIST CNR) in Gaithersburg, MD. SANS measurements are performed on the NG3 beamline at three detector positions, for equilibrium samples, to obtain the scattering intensity, *I(q)*, over a wide *q*-range ($0.002 < q$ (Å^{-1}) < 0.4), while kinetic measurements (e.g. dielectric-SANS) used only two detector positions for a more limited *q*-range with higher flux ($0.006 < q$ (Å^{-1}) < 0.4).[27] The total scattering is normalized to the incident beam flux, corrected for empty cell scattering and 2D profiles were then converted to 1D profiles using standard methods.[28]

Equilibrium samples are measured in 1 mm pathlength demountable cells with quartz windows. Kinetic experiments simultaneously measuring AC dielectric properties and SANS (e.g. dielectric-SANS) are performed in using electrically insulated demountable cell with a 1 mm pathlength and stainless steel windows also serving as electrodes. More details regarding this sample environment are found elsewhere.[4] Sample cells are loaded with a hot polymer solution (~80 °C) before being rapidly quenched (> 10 °C/min) in the beamline to experimental temperatures. Counting times are started when an identical cell, filled with ethylene glycol, located in the same sample environment as the sample reaches the experimental temperature. In line with recent work, samples are run twice at different detector distances, reduced to 1D profiles and then stitched together based on the elapsed time.[4] Point-by-point matching is utilized to associate the dielectric and SANS data. USANS measurements are performed on the BT5 perfect crystal diffractometer extending the *q*-range to 5×10^{-5} Å^{-1} for equilibrium organogel samples. The data is reduced and desmeared using Igor-based macros developed by NIST.[7] All model fitting is performed using DANSE SASView software.[8]

Dielectric Spectroscopy.

AC dielectric spectroscopy measurements are performed using an Agilent e4980a LCR Meter. A perturbation voltage of 600 mV, within the linear impedance response range, and a frequency range of 20 Hz – 2 MHz are used for all samples.[11, 12] Reported conductivities are calculated at a frequency of 2 kHz and all measurements are performed between stainless steel plates. No intentional molecular dopants are utilized to enhance the reported conductive properties of the samples.

Rheology.

Oscillatory rheology measurements are performed on an Anton Paar MCR 301 stress controlled rheometer using a 25 mm parallel plate geometry. Unless otherwise stated, a frequency of 1 Hz, 0.4 mm gap and 0.25% perturbation strain (in the linear viscoelastic regime for P3HT gels), are used for all measurements.[3, 4] A fully dissolved polymer solution (~ 80 °C) is loaded into the pre-heated (40 °C) sample gap. The solution is rapidly cooled to induce gelation after which a thin layer of fluorinated non-conductive oleophobic liquid (Fomblin Y 25/6) is added to the edge of the geometry in order to prevent evaporation at elevated temperatures. The gel is then reheated to 80 °C to fully dissolve the gel prior to starting the experiment. Temperature sweeps are performed using a cooling rate of 1 °C/min while kinetic experiments are performed by rapidly quenching (> 40 °C/min) the sample.

Scanning Transmission Electron Microscopy.

Small quantities of organogels formed at 20 °C are transferred to copper grids with Formvar supports by gently touching the grid to the surface of the gel without

applying pressure. Because of the thin nature of the transferred sample, the solvent evaporates rapidly under ambient conditions. Scanning transmission electron microscopy (sTEM) images are obtained with a FEI Technai G2 F20 transmission electron microscope operating at 200 kV.

P3ATs Gel Formation.

Table 4.1. Properties of poly(3-alkylthiophene)s including molecular weight (M_w^{chain}), polydispersity index (PDI), and regioregularity (*RR*).

	Type	M_w^{chain} **(g/mol)**	**PDI**	***RR***
P3HT (Low M_w)	Sepiolid P200	21,000	1.6	95%
P3HT (High M_w)	4002-E	53,000	2.3	92%
P3OT	4003-E	83,000	1.9	91%
P3DDT	4005-E	51,000	1.8	92%

For the gelation of P3ATs, hydrogenated solvents, 1,2-dichlorobenzene (DCB) and n-dodecane (Sigma-Aldrich), are used as received. Deuterated solvents are used to decrease the incoherent scattering background and increase the scattering contrast in SANS and USANS experiments. D4-1,2-dichlorobenzene and D26-dodecane (Sigma-Aldrich) are used as received. All samples are prepared by adding 30 mg/mL P3AT to a mixture of deuterated 1,2-dichlorobenzene and dodecane. Samples are then heated above 80 ºC until all visible signs of polymer powder (black) had disappeared and only a bright orange solution remained. For this portion of the research, the kinetics of aggregation is controlled by using different ratios of a good and bad solvents for P3AT such as o-

dichlorobenzene and dodecane, respectively. All solvent mixture percentages in this work are by weight. Two lots of regioregular poly(3-hexylthiophene) (P3HT), one lot of regioregular poly(3-octylthiophene) (P3OT) and one lot of regioregular poly(3-dodecylthiophene) (P3DDT) were used as received from Rieke Metals (Lincoln, NE). The molecular weight (M_w^{chain}), polydispersity index (PDI) and regioregularity (*RR*) for all of these polymers is shown in Table 4.1.

Self-assembly in solution for conjugated polymers is driven by a reduction in solubility induced through changes in temperature or the addition of a miscible non-solvent.[2, 9-11] Variability in shape and structure are common for different conjugated polymers assembled in solution.[1-4, 12-18] This is largely dependent on the specific chemistry of the backbone and side chains, the regioregularity, molecular weight and the solvent environment during crystallization. Self-assembled regioregular poly(3-alkylthiophene)s (RR-P3ATs) have been shown to form long fibers (a.k.a. whiskers, nanowires or ribbons) with high aspect ratio and rectangular cross-section.[9, 14, 19] When assembled at moderately high concentrations (> 5 mg/mL) these fibers will percolate to form weak interconnected organogels.[2-5, 13, 15, 17, 20-29]

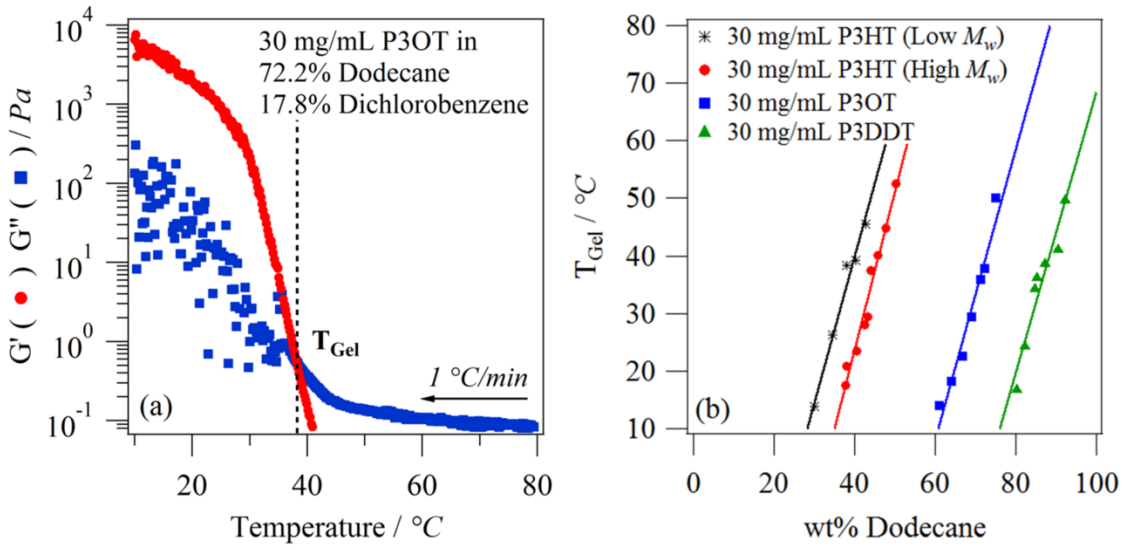

Figure 4.1: Left: Characteristic rheological curve of the gelation of a P3AT sample. The sample shown is a 30 mg/ml P3OT dissolved in a 72.2% dodecane solvent mixture. The dashed line marks the T_{gel} temperature, which in this case is defined as the temperature in which the storage modulus surpasses the loss modulus. Right: Gelation temperature is plotted against dodecane content in the solvent mixture for different P3ATs (all measured at a cooling rate of 1 °C/min). Linear fits are also shown with nearly identical slopes.

Figure 4.1a shows the rheological response of a typical P3AT in solution during a slow cooling ramp (1 °C/min). When the temperature gets low enough the storage modulus (elastic, G') surpasses the loss modulus (viscous, G''). The point at which G'=G'' is commonly known as the gel point because it corresponds well with mechanical percolation and gelation. The temperature at which this occurs will be referred as T_{Gel}. P3AT self-assembly is both a kinetic and thermodynamic process and therefore T_{Gel} will be dependent on experimental conditions such as the cooling rate. In this work, the cooling rate was held constant for all samples. Figure 3.1b shows that T_{Gel} varies linearly

as a function of dodecane content for each alkyl chain length when all experimental conditions are held constant.

Alkyl side are necessary to entropically facilitate the dissolution of the typically rigid polymer backbones of conjugated polymers.[30, 31] Longer alkyl chains (e.g. P3DDT) add more entropy and result in higher polymer solubility than short alkyl chain lengths (e.g. P3HT). Figure 4.1b also shows a difference in solubility between P3HT batches. In this case, it is as a result of differences in molecular weight. It is well known that polymers with higher M_w are generally less soluble and in this study there is a difference of 250% between these two batches (Table 4.1). There is also an unexpected, but distinctly linear, trend between dodecane content and gelation temperature for all P3ATs. The slopes are similar: low M_w P3HT (253 ± 24 °C/dodecane wt%), high M_w P3HT (274 ± 19 °C/dodecane wt%), P3OT (251 ± 22 °C/dodecane wt%) and P3DDT (244 ± 31 °C/dodecane wt%) suggesting that dodecane content may influence the solubility of the thiophene backbone by changing the solvent's polarizability.

P3AT Gel Small Angle Neutron Scattering.

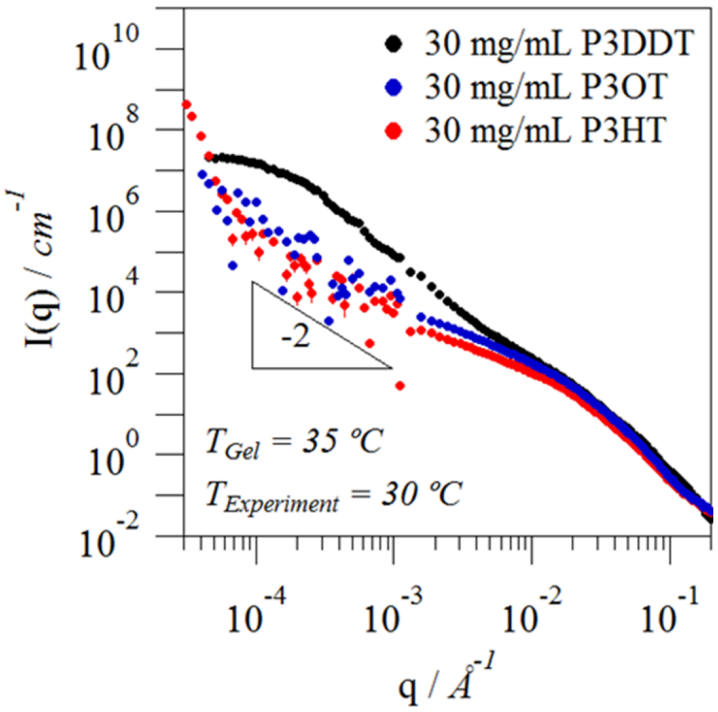

Figure 4.2: Combined SANS and USANS (desmeared) profiles of high Mw P3HT in 43.9% dodecane/56.1% DCB, P3OT in 71.3% dodecane/28.7% DCB and P3DDT in 84.7% dodecane/15.3% DCB self-assembled for 24 hours at 30 °C.

Figure 4.2 shows SANS and USANS profiles for 30 mg/mL P3AT organogels self-assembled in deuterated solvent mixtures. Solvent mixtures were selected for each polymer to achieve a T_{Gel} of 35 °C. This corresponded to 43.9 wt% dodecane/56.1 wt% DCB for P3HT (high M_w), 71.3 wt% dodecane/28.7 wt% DCB for P3OT and 84.7 wt% dodecane/15.3 wt% DCB for P3DDT based on Figure 4.1. The SANS portion of the data can be fitted to a combined parallelepiped and polymer excluded volume form factors model[32].

Dissolved P3AT chains are represented by a model for polymers with excluded volume effects ($P_{PExV}(q)$).[3, 4, 33] P3AT fibers with rectangular cross-section are modeled using a parallelepiped ($P_{PP}(q)$) form factor.[2-4, 28, 34] This combined model applies a mass balance on P3AT, limited by the total volume fraction of polymer in solution (ϕ_v), to determine the cross-sectional dimensions of the growing fibers (a and b) and to account for the fraction of P3AT that exists in fiber form (Ψ_f) at any given time. Equation 4.2 describes the scattering intensity (I) as a function of the scattering vector (q) for the model:

$$I(q) = \phi_v \psi_f (\Delta\rho_{PP})^2 P_{PP}(q) + \phi_v (1-\psi_f)(\Delta\rho_{PExV})^2 P_{PExV}(q) \qquad \text{(Eq 4.2)}$$

where, $\Delta\rho_{PP}$ is the scattering contrast between the solvent mixture and P3AT fibers and $\Delta\rho_{PExV}$ is the scattering contrast between the solvent mixture and the dissolved P3AT chains.[3, 4]

By fixing most variables in the model (Equation 3.1) to known or independently measured values, only three unknown parameters remain: fraction of polymer in fiber from (Ψ_f), fiber thickness (a), and fiber width (b). Each profile is fit with this model enabling the accurate extraction of these parameters as a function of time. Previous studies have shown that the parallelepiped model is only valid over a limited q-range ($q >$ 0.009 Å^{-1}), because the branched network starts to dominate the scattering at low-q ($q <$ 0.009 Å^{-1}).[2-4]

The fits show high M_w P3HT fibers with an average width of 23.4 nm and thickness of 4.4 nm, P3OT fibers with an average width of 26.1 nm and thickness of 4.6 nm, and P3DDT fiber with an average width of 22.2 nm and thickness of 4.9 nm. The lattice parameters of non-intercalating P3AT fibers can be used to estimate that high *Mw* P3HT and P3OT fibers are on average between 2 – 3 chains thick, while P3DDT fibers are on average 2 chains thick.[35] The scattering profiles show that P3HT and P3OT have similar network structures over $10^{-4} < q$ (Å^{-1}) $< 10^{-2}$, corresponding to a region of real space dimensions of 63 nm – 6.3 μm. In contrast, the scattering profile of the P3DDT gel at low q (USANS range) has a larger slope suggestive of a denser network structure. It also shows a turnover characteristic of finite domains with a radius of gyration of approximately 1.2 μm based a Guinier fit.[2, 3] At $q < 10^{-4}$ Å^{-1}, the scattering of P3HT and P3OT also start to differ. The profile of the P3OT organogel has a fairly constant slope at low q but there is a turn-over to a larger slope for the P3HT organogel. This is suggestive of a slightly more heterogeneous network structure for P3HT organogels when compared to P3OT for the largest length scales (> 10 μm).[2, 3]

Dielectric Behavior of P3AT Samples During Gelation.

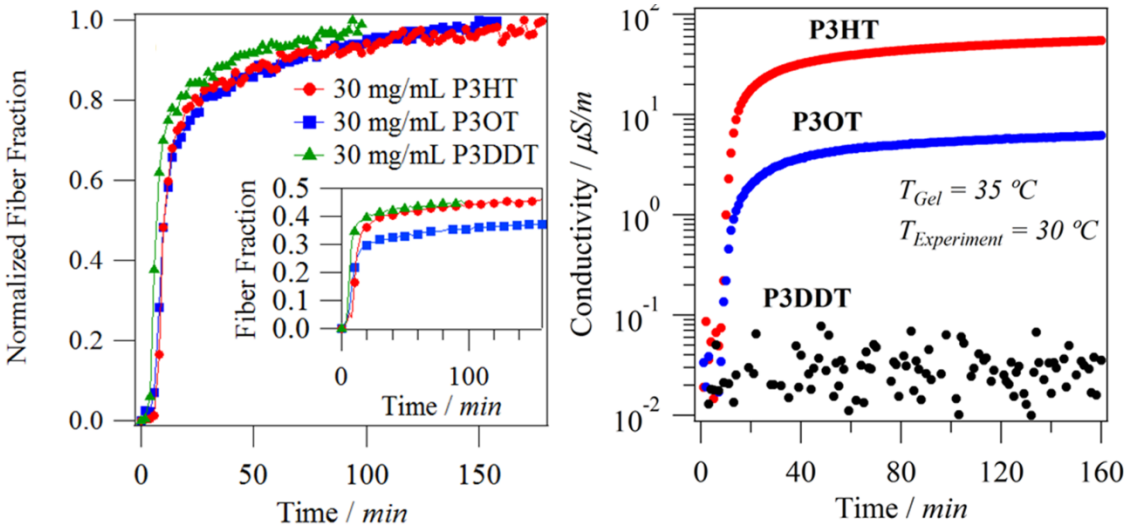

Figure 4.3: Left: Fraction of P3AT in fiber extracted from a SANS model fit for 30 mg/mL high M_w P3HT in 43.9 wt% dodecane/56.1 wt% DCB, 30 mg/mL P3OT in 71.3 wt% dodecane/28.7 wt% DCB and 30 mg/mL P3DDT in 84.7 wt% dodecane/15.3 wt% DCB, normalized to the maximum fiber fraction. The inset image shows the non-normalized fiber fraction as a function of time. Right: Conductivity from simultaneous dielectric-SANS experiments for 30 mg/mL P3ATs in the same solvent mixtures as listed above.

The dielectric evolution of the P3AT samples is tracked while the organogel forms and is being exposed to the neutron beam. These dielectric-SANS experiments are performed using an electrically insulated demountable cell with a 1 mm pathlength and stainless steel windows also serving as electrodes. More details regarding this sample environment are found elsewhere.[4] Sample cells were loaded with a hot polymer solution (~ 80 °C) before being rapidly quenched (> 10 °C/min) in the beamline to experimental temperatures. Experiments were started when samples reached experimental temperatures as judged by an identical cell that was filled with ethylene glycol that was in the same

temperature control block. In line with recent work, samples were run twice at different detector distances, reduced to 1D profiles and then stitched together based on the elapsed time.[4] Point-by-point matching was utilized to associate the dielectric and SANS data.

Figure 4.3 left shows the kinetics of self-assembly for P3AT gels by plotting the normalized fiber fraction (Ψ_f) over time. It shows that kinetically, the gels form in a very similar fashion where almost 80% of self-assembly occurs within the first 30 minutes and then reduces to a much slower rate. The similar self-assembly kinetics for variable alkyl chain lengths indicates that the driving force is also similar. Even though the driving force for self-assembly is similar, the final conductivity of the gels varies by orders of magnitude (figure 4.3 right). Furthermore, the conductivity of the P3DDT sample does not change during self-assembly. The differences in magnitude of the conductivity at similar fiber fractions are due, in part, to the difference in alkyl chain length. Charge hoping between thiophene layers, a transport mechanism in conjugated polymer networks, will be less likely for longer alkyl chains.[36] For P3DDT the changes in conductivity are either below the resolution of the measurement or even more fibers would be needed to achieve percolation.

Induce Supersaturation Changes on the Organogel Structure and Properties Using Different Good/Poor Solvent Ratios.

It is possible to engineer the structure and properties of organogels through changes in the content of poor-solvent in the mixture for any polymer. The theory that links gelation kinetics to supersaturation and branching fibrillar network structure has been established by Li *et al*.[37] Chapter 3 shows that, for organogels of poly(9,9-

dioctylfluorene) (PFO), increased supersaturation resulted in denser, branched networks. Figure 4.4 shows that a similar trend exists for low M_w P3HT organogels.

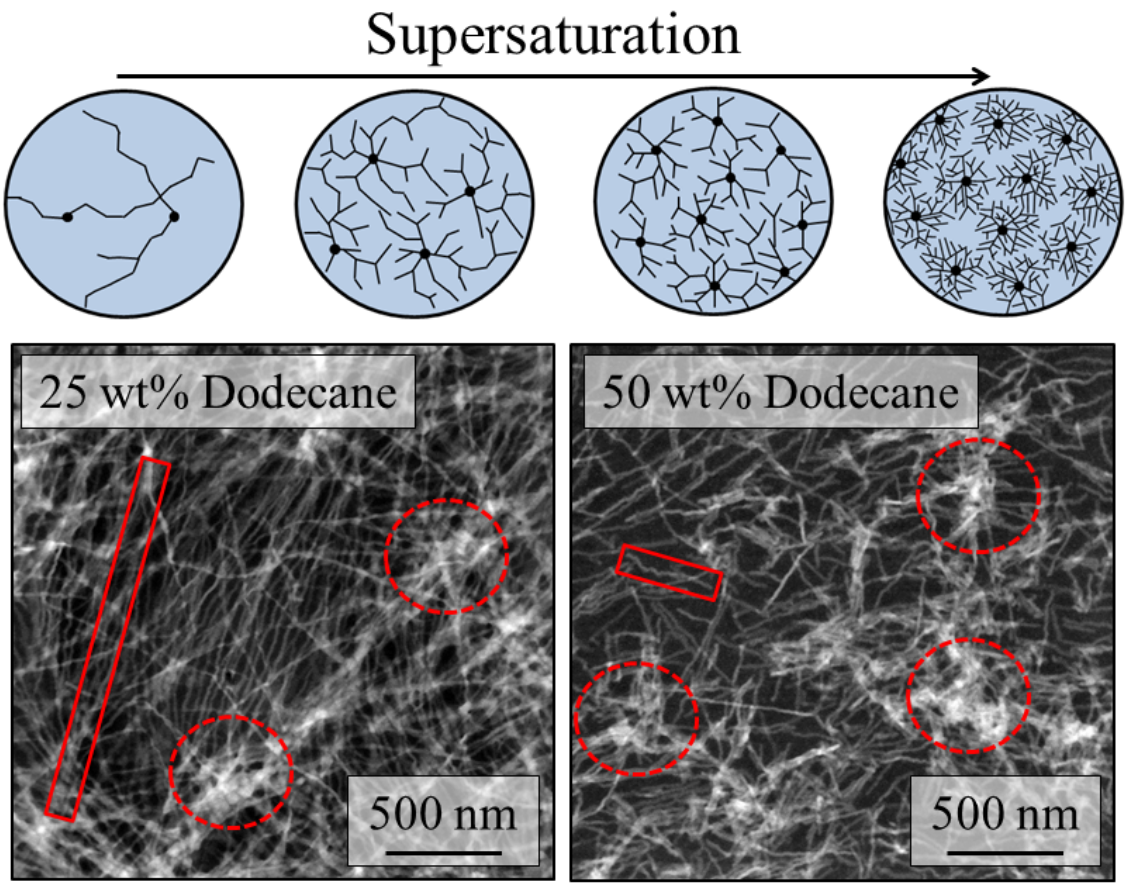

Figure 4.4: Top: Schematics showing the correlation between solvent-quality and fiber branching as proposed by Li et al.[86] Bottom: Scanning transmission electron microscopy (sTEM) images of 30 mg/mL low Mw P3HT organogels isothermally self-assembled to equilibrium in 1,2-dichlorobenzene/dodecane solvent mixtures at 20 °C. Samples were allowed to evaporate prior to imaging. Fiber length is highlighted with a solid box and dense fiber regions are highlighted with a dashed circle.

sTEM images of low M_w P3HT organogel networks formed in different solvent/non-solvent mixture ratios as shown in Figure 4.4. As the ratio of dodecane increases so does the driving force for polymer self-assembly. The SANS results in Figure 4.5 show that more fibers are formed as a result of increasing dodecane ratio.

However, Figure 4.4 shows that the structure of the fiber network also changes. At a dodecane ratio of 25 wt%, sTEM images show predominantly long, overlapping fibers (> 3 μm). This is in contrast to gels formed in a 50 wt% dodecane ratio which show shorter, more branched fiber networks often with less than 1 μm fiber length before branching or splitting occurs. Furthermore, low M_w P3HT fiber networks formed at high dodecane ratios also show an increased frequency of dense heterogeneous regions. The structural trends seen in these sTEM images are well described by the theory for supersaturation of organogelators where a higher driving force for self-assembly results in more nucleation centers and lattice mismatches that lead to higher branching frequency.[37]

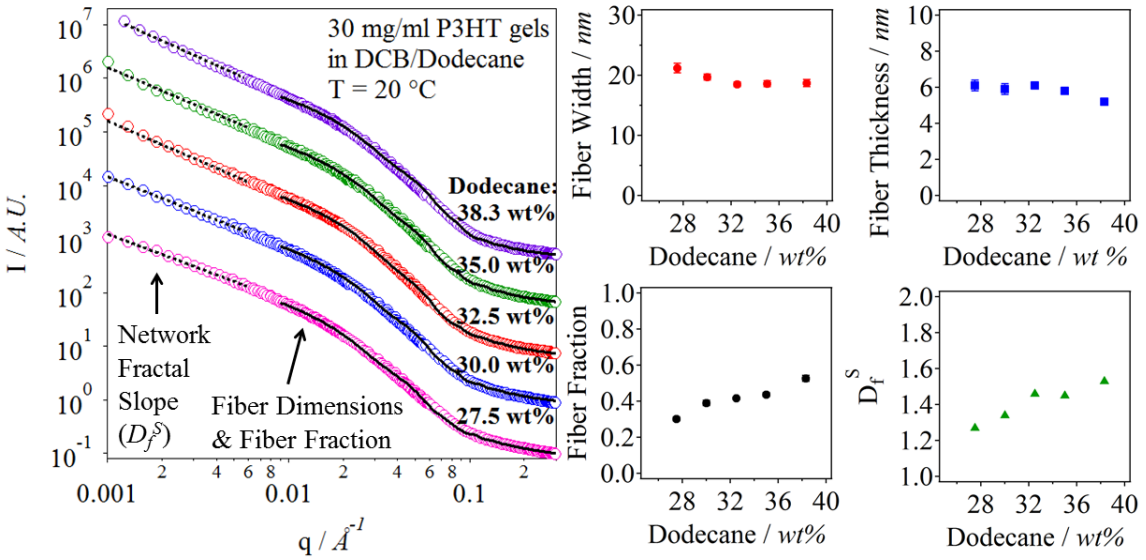

Figure 4.5: SANS profiles and corresponding fits, both shifted for clarity, of 30 mg/mL low Mw P3HT in dodecane/1,2-dichlorobenzene solvent mixtures self-assembled for at least 24 hours at 20 °C. Fiber width, fiber thickness and fiber fraction are extracted from SANS using Equation 2. The network fractal dimension (D_f^S) is extracted using a power law fit of the SANS profiles from 0.001 < q (Å^{-1}) < 0.006 shown as a dashed black line.

Figure 4.5 shows the SANS profiles, fit with Equation 4.2, of fully formed low M_w P3HT organogels in different solvent ratios. As previously demonstrated, changes in

driving force for P3HT organogel self-assembly has little impact on the cross-sectional shape of the fibers.[3] In this case, the fiber thickness and width are nearly identical with an average width of ~ 20 nm and an average thickness of ~6 nm, which corresponds to three polymer chains without interdigitation.[35] At low-q ($q < 0.006$ Å^{-1}), SANS profiles are also fit with a power law equation to extract a fractal dimension for this length scale (D_f^S). The fractal dimension arises from inter-fiber correlations that develop over a size range of 100 – 600 nm. The D_f^S results in Figure 4.5 show a similar trend to the sTEM images, where increasing dodecane ratio results in more dense fiber network structures with $D_f^S = 1.27$ for low M_w P3HT in 27.5 wt% dodecane and $D_f^S = 1.53$ for low M_w P3HT in 38.3 wt% dodecane.

Figure 4.6 shows the USANS profiles corresponding to some of the SANS profiles in Figure 4.5. This measurement characterizes a size range of 250 nm to 20 μm that is primarily influenced by the network structure. All of the USANS profiles, except for the low M_w P3HT gel in 27.5 wt% dodecane, show a turnover at low-q that is similar to the P3DDT gel in Figure 4.2. This indicates the formation of a more heterogeneous structure at these length scales as illustrated in the inset diagram in Figure 4.6. The turnover can be fit with the Guinier equation to determine a radius of gyration of these domains. The radius of gyration was found to be 5.1 μm, 1.3 μm, 1.1 μm for 30 mg/mL low M_w P3HT in 30 wt%, 32.5 wt% and 38.3 wt% dodecane. This is in agreement with the trend in Figure 4.4 that shows that gels formed in solvents with higher dodecane content have more nucleation centers and smaller network domains.

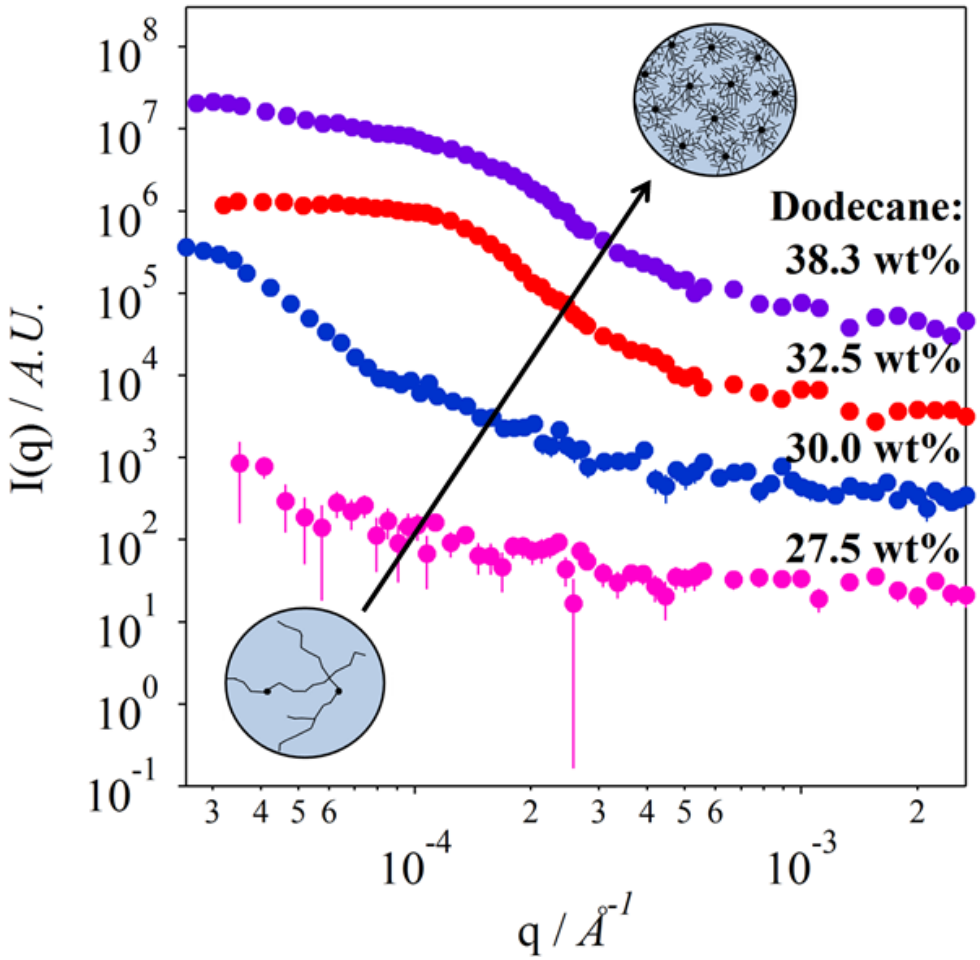

Figure 4.6: Smeared USANS profiles of 30 mg/mL low Mw P3HT in 1,2-dichlorobenzene/dodecane solvent mixtures self-assembled for at least 24 hours at 20 °C.

The properties and self-assembly kinetics are also affected by the solvent ratio. Figure 4.7 shows the isothermal rheology kinetics of P3HT gels formed in different solvent mixture ratios. The complex modulus (G^*), where $G^* = \sqrt{(G')^2 + (G'')^2}$, is plotted as a function of time after the temperature reaches 20 °C. As expected, all samples start as viscous polymer solutions before the modulus rapidly increases, indicating gelation. The initial gelation time decreases as the fraction of dodecane

increases. Furthermore, the final modulus of the gel increases with increasing dodecane fraction for samples with dodecane fractions of 25 – 30 wt%. However, the final modulus for samples with more than 30 wt% dodecane decreases again. This same trend is observed in the final conductivity of the P3AT organogels (Figure 4.8). A maximum in conductivity was also observed by Zhu and coworkers who studied P3HT solution phase self-assembly with solvent mixtures (chlorobenzene/anisole), but did not ascribe this behavior to structural features.[18] The structural data from SANS, USANS and sTEM indicate that this peak in modulus and conductivity is a result of competing factors between increasing fiber fraction and increasing network heterogeneity or branching. Gels formed at low dodecane fractions form fewer fibers (Figure 4.5) but these fibers tend to be longer (Figure 4.4) and a more homogeneous network structure is formed (Figure 4.6). In contrast, with very high dodecane fractions, gels contain more fibers (Figure 4.5) but these tend to be highly branched (Figure 4.4) and more heterogeneous which is detrimental to conductivity (Figure 4.6). This leads to a maximum conductivity when there is a relatively large number of fibers but where these also form homogeneous interconnected networks. Finally, difference in conductivities (Figure 4.8) of more than order of magnitude demonstrate that solvent/poor-solvent ratios are important engineering parameters to optimize the performance and structure of networks in organic electronic devices.

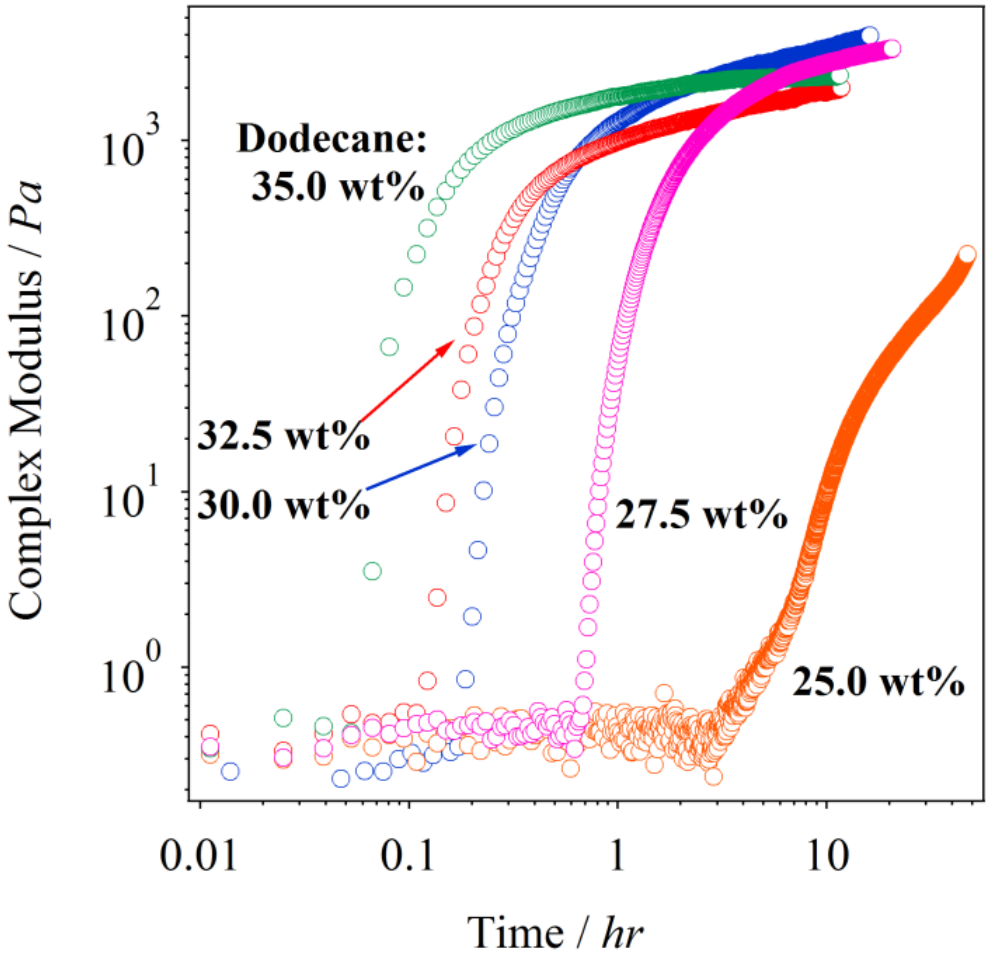

Figure 4.7: Oscillatory rheology of 30 mg/mL low Mw P3HT in 1,2-dichlorobenzene/dodecane solvent mixtures during isothermal gelation at 20 °C.

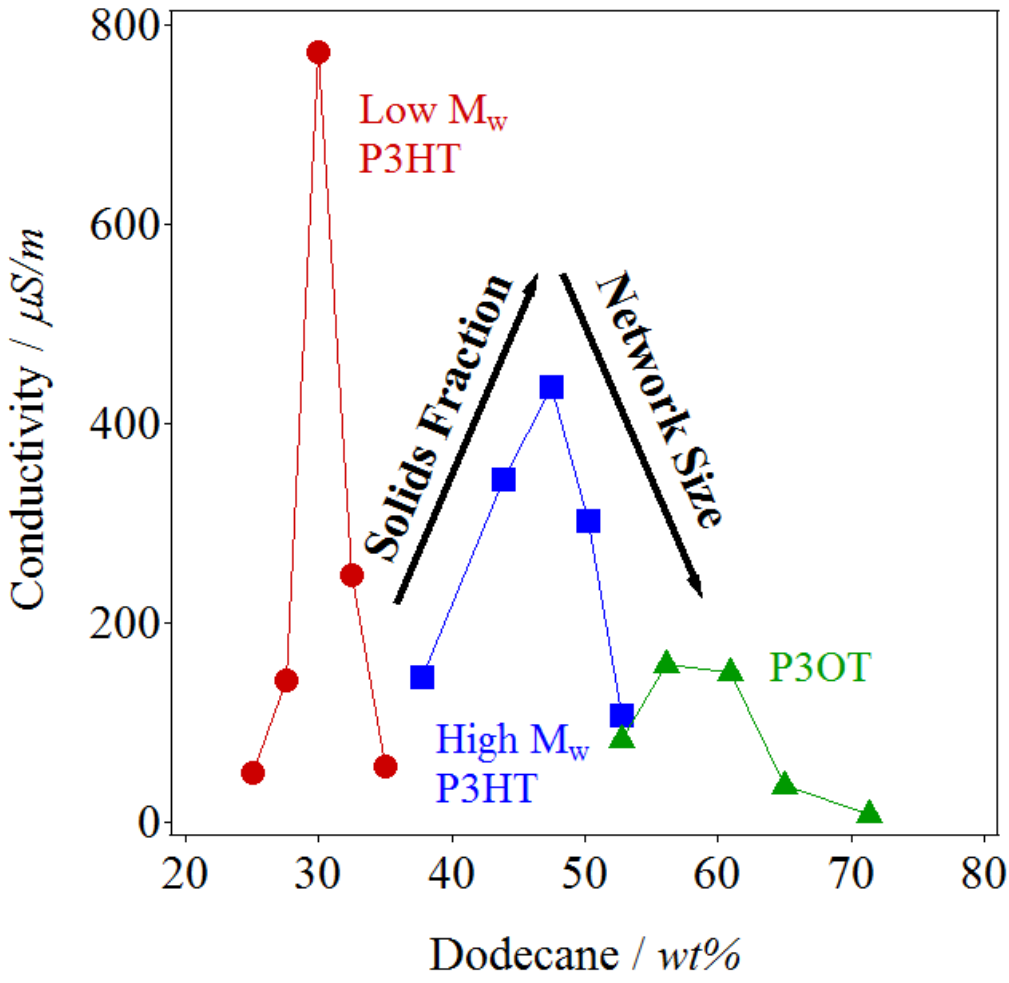

Figure 4.8: Conductivity of 30 mg/mL low M_w P3HT, high M_w P3HT and P3OT organogels self-assembled to equilibrium at 20 °C in 1,2-dichlorobenzene/dodecane solvent mixtures.

Thin Film Deposition of Organogels.

The organogel mesostructure, which arises from the formation of polymer aggregates, increases the elasticity of the system, making it difficult to coat uniform films. [21, 38, 39] For this reason, the formation of these organogels has been linked to poor performance in devices, even when the mesotructure and electric properties of the polymeric domains increase the suitability of the polymer for their applications. This has

led to the development of numerous methodologies to produce uniform coatings from gels. These methods involve either the freezing, sonicating, or emulsifying the gel structure.[21 40 39] All of these organogel coating methods have yielded promising results for organic electronics, but each has stages that can damage the interconnected structure or introduce insulating molecules.

In this study, we present a facile route towards controlling poly(3-alkylthiophene) (P3AT) gelation while allowing for the formation of uniform thin-film gels at room temperature. We utilize low volatility solvent/poor-solvent mixtures to control supersaturation (i.e. driving force for gelation) while reducing the influence of solvent evaporation effects. The structure of the gels is characterized using scanning transmission electron microscopy (sTEM).

The potential for forming interconnected networks in thin-film organic electronics has long been suggested but the elastic mechanical nature of organogels is incompatible with traditional coating processes (e.g. spin-coating).[38] Figure 4.9 demonstrates a novel approach for forming organogels in thin-films using solvent/non-solvent mixtures with low vapor pressures. The pictures demonstrate thermoreversible gelation in bulk and in thin-films for P3HT. Gelation in thin films that are deposited as liquids is only possible because the vapor pressures of the two solvents are low enough to slow down evaporation while gelation proceeds. 1,2-dichlorobenzene (DCB) has a vapor pressure of 1.4 mm Hg at 20 °C, while n-dodecane has a vapor pressure of 0.1 mm Hg at 20 °C.[41] These thin-films can be dried under vacuum in approximately 24 hours or they can be rinsed with a miscible non-solvent of higher volatility (e.g. hexane) after the gel is fully formed. Figure 10 shows films formed using drop-casting from the dissolved liquid

state. We have also used this method to produce thin-films with blade coating, screen printing and spin coating.

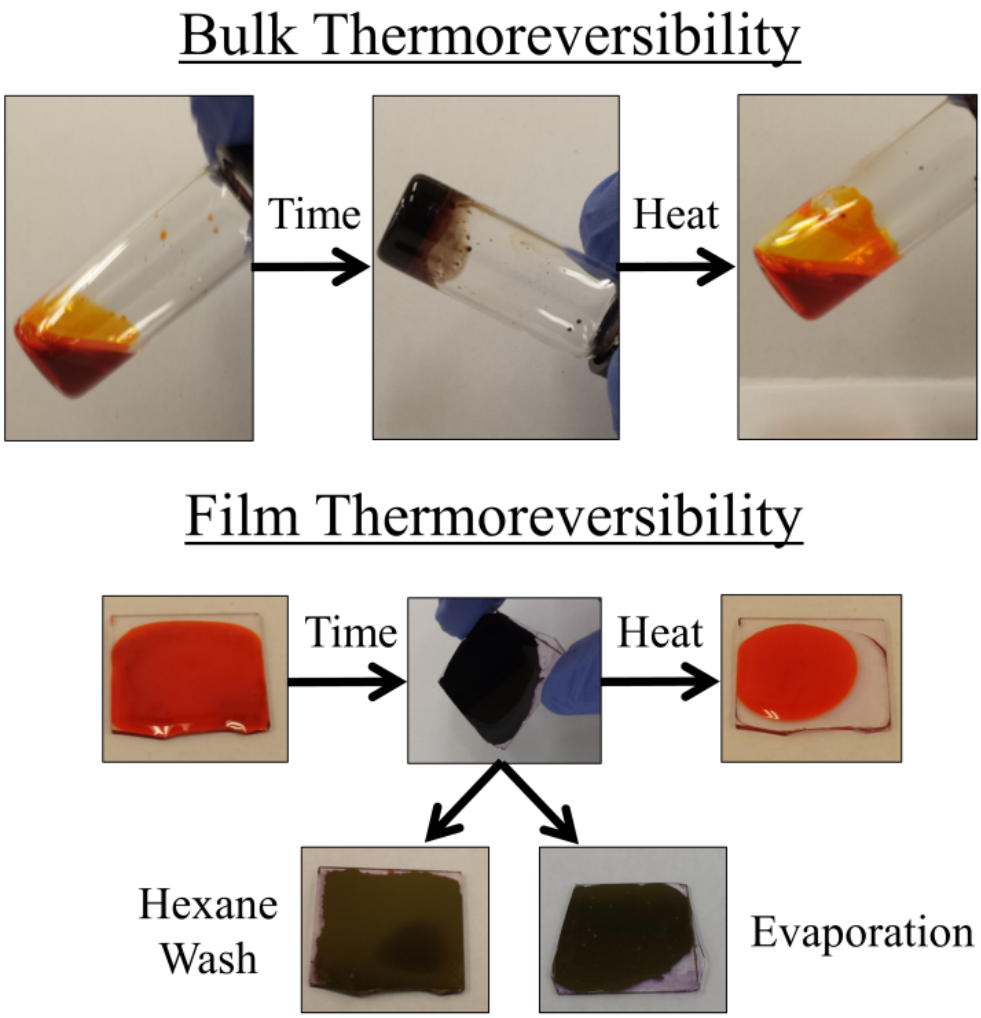

Figure 4.9: Pictures of 30 mg/mL low M_w P3HT in a solvent mixture of 70 wt% 1,2-dichlorobenzene and 30 wt% dodecane. Top images represent bulk gelation while bottom images represent gels formed in a film. The left image on top and bottom is a fully dissolved P3HT solution after heating. Over time the solutions, in bulk or coated, self-assemble into P3HT organogels that can be re-heated again to re-dissolve the gel and form orange solutions. The two lower images are of organogel films that were dried by evaporation and through a hexane rinse.

Figure 4.10 shows scanning electron microscopy (SEM) images of P3HT films casted by using spin coating (Figure 4.10 a) and doctor blading (Figure 4.10 b). This films are casted by controlling the kinetics of gelation in such a way that it will gel faster than the evaporation of the solvents, but slow enough so that the increase in viscosity does not affect the film casting process. The end results are homogenous films like the ones shown as insert in figure 4.10.

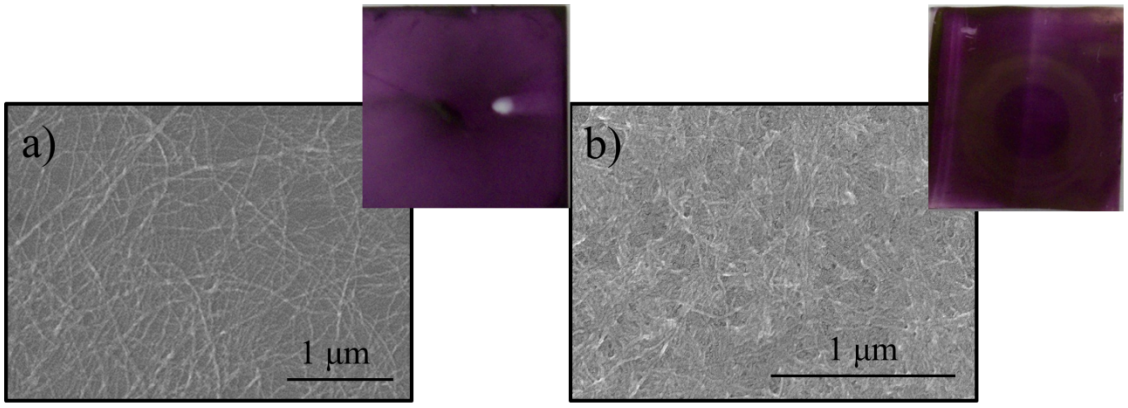

Figure 4.10: SEM images of P3HT organogels coated on a glass substrate. The films are deposited using spin casting (a) and doctor blading (b). The inserts are pictures of the films that were imaged.

Conclusions.

We have demonstrated that low volatility solvent/poor-solvent mixtures can be used to engineer the structure and properties of poly(3-alkylthiophene) (P3AT) organogels. Furthermore, we showed that the low volatility of the solvent mixture could be utilized to achieve thermoreversible gelation in a thin-film environment and at room temperature. These findings enable the facile design and application of organogels of conjugated polymers with desired structure and properties for use in organic electronics. We demonstrated that the use of dodecane and 1,2-dichlorobenzene allowed for gelation over of a wide range of alkyl chain lengths. We determined that differences in insulating alkyl chain length led to drastically different properties even when self-assembly kinetics were very similar. We also showed that increasing dodecane fraction leads to faster self-assembly kinetics for P3HT organogels. The resultant organogel structures could be described by invoking a well-known nucleation and growth theory. sTEM, SANS and USANS all showed that higher dodecane ratios led to more branching and smaller network sizes. A peak in the conductivity of fully formed low M_w P3HT gels was found to be the result of a competition between the number of fibers and the network size and it is likely these same parameters that lead to the conductivity peaks in the high M_w P3HT and P3OT gels. These results demonstrate that simple and tunable parameters, such as alkyl chain structure and solvent ratio, can have drastic effects on the properties of conjugated polymer organogels. Moreover, this work presents a novel way to incorporate this range of engineering control into the final application of thin-film electronic devices.

References

1. de la Iglesia, P.; Pozzo, D. C., Effects of supersaturation on the structure and properties of poly(9,9-dioctylfluorene) organogels. *Soft Matter* 2013, 9, (47), 11214-11224.
2. Newbloom, G.; Kim, F.; Jenekhe, S.; Pozzo, D., Mesoscale Morphology and Charge Transport in Colloidal Networks of Poly(3-hexylthiophene). *Macromolecules* 2011, 3801-3809.
3. Newbloom, G. M.; Weigandt, K. M.; Pozzo, D. C., Electrical, Mechanical, and Structural Characterization of Self-Assembly in Poly(3-hexylthiophene) Organogel Networks. *Macromolecules* 2012, 45, (8), 3452-3462.
4. Newbloom, G. M.; Weigandt, K. M.; Pozzo, D. C., Structure and property development of poly(3-hexylthiophene) organogels probed with combined rheology, conductivity and small angle neutron scattering. *Soft Matter* 2012, 8, (34), 8854-8864.
5. Malik, S.; Jana, T.; Nandi, A. K., Thermoreversible gelation of regioregular poly(3-hexylthiophene) in xylene. *Macromolecules* 2001, 34, (2), 275-282.
6. Newbloom, G. M.; Weigandt, K. M.; Pozzo, D. C., Structure and property development of poly(3-hexylthiophene) organogels probed with combined rheology, conductivity and small angle neutron scattering. *Soft Matter* 2012, 8, (34).
7. Barker, J. G.; Glinka, C. J.; Moyer, J. J.; Kim, M. H.; Drews, A. R.; Agamalian, M., Design and performance of a thermal-neutron double-crystal diffractometer for USANS at NIST. *Journal of Applied Crystallography* 2005, 38, 1004-1011.
8. Butler, P.; Alina, G.; Hernandez, R. C.; Doucer, M.; Jackson, A.; Kienzle, P.; Kline, S. R.; Zhou, J. SASView for Small Angle Scattering Analysis. http://www.sasview.org/.
9. Oosterbaan, W. D.; Bolsée, J.-C.; Gadisa, A.; Vrindts, V.; Bertho, S.; D'Haen, J.; Cleij, T. J.; Lutsen, L.; McNeill, C. R.; Thomsen, L.; Manca, J. V.; Vanderzande, D., Alkyl-Chain-Length-Independent Hole Mobility via Morphological Control with Poly(3-alkylthiophene) Nanofibers. *Advanced Functional Materials* 2010, 20, (5), 792-802.
10. Samitsu, S.; Shimomura, T.; Heike, S.; Hashizume, T.; Ito, K., Effective Production of Poly(3-alkylthiophene) Nanofibers by means of Whisker Method using Anisole Solvent: Structural, Optical, and Electrical Properties. *Macromolecules* 2008, 41, (21), 8000-8010.
11. Samitsu, S.; Shimomura, T.; Ito, K., Nanofiber preparation by whisker method using solvent-soluble conducting polymers. *Thin Solid Films* 2008, 516, (9), 2478-2486.
12. Alcazar, D.; Wang, F.; Swager, T. M.; Thomas, E. L., Gel Processing for Highly Oriented Conjugated Polymer Films. *Macromolecules* 2008, 41, (24), 9863-9868.
13. Berson, S.; De Bettignies, R.; Bailly, S.; Guillerez, S., Poly (3-hexylthiophene) fibers for photovoltaic applications. *Advanced Functional Materials* 2007, 17, (8), 1377-1384.

14. Liu, J.; Arif, M.; Zou, J.; Khondaker, S. I.; Zhai, L., Controlling Poly(3-hexylthiophene) Crystal Dimension: Nanowhiskers and Nanoribbons. *Macromolecules* 2009, 42, (24), 9390-9393.
15. Kim, F. S.; Jenekhe, S. A., Charge Transport in Poly(3-butylthiophene) Nanowires and Their Nanocomposites with an Insulating Polymer. *Macromolecules* 2012, 45, (18), 7514-7519.
16. Szymanski, C.; Wu, C.; Hooper, J.; Salazar, M. A.; Perdomo, A.; Dukes, A.; McNeill, J., Single Molecule Nanoparticles of the Conjugated Polymer MEH−PPV, Preparation and Characterization by Near-Field Scanning Optical Microscopy. *The Journal of Physical Chemistry B* 2005, 109, (18), 8543-8546.
17. Yu, Z.; Fang, J.; Yan, H.; Zhang, Y.; Lu, K.; Wei, Z., Self-Assembly of Well-Defined Poly(3-hexylthiophene) Nanostructures toward the Structure–Property Relationship Determination of Polymer Solar Cells. *The Journal of Physical Chemistry C* 2012, 116, (45), 23858-23863.
18. Zhu, Z.; Wei, B.; Wang, J., Self-assembly of poly(3-hexylthiophene) nanowire networks by a mixed-solvent approach for organic field-effect transistors. *physica status solidi (RRL) – Rapid Research Letters* 2013, n/a-n/a.
19. Samitsu, S.; Shimomura, T.; Heike, S.; Hashizume, T.; Ito, K., Field-Effect Carrier Transport in Poly(3-alkylthiophene) Nanofiber Networks and Isolated Nanofibers. *Macromolecules* 2010, 43, 7891-7894.
20. Chen, J.-Y.; Hsu, F.-C.; Sung, Y.-M.; Chen, Y.-F., Enhanced charge transport in hybrid polymer/ZnO-nanorod solar cells assisted by conductive small molecules. *Journal of Materials Chemistry* 2012, 22, (31), 15726-15731.
21. Huang, P.-T. C., Yao-Sheng Chou, Cheng-Wei, Preparation of porous poly(3-hexylthiophene) by freeze-dry method and its application to organic photovoltaics. *Journal of Applied Polymer Science* 2011.
22. Huang, W.; Huang, P.; Han, Y.; Lee, C.; Hsieh, T.; Chang, M., Aggregation and Gelation Effects on the Performance of Poly(3-hexylthiophene)/Fullerene Solar Cells. *Macromolecules* 2008, 7485-7489.
23. Malik, S.; Nandi, A. K., Thermodynamic and structural investigation of thermoreversible poly(3-dodecylthiophene) gels in the three isomers of xylene. *Journal of Physical Chemistry B* 2004, 108, (2), 597-604.
24. Sobkowicz, M. J.; Jones, R. L.; Kline, R. J.; DeLongchamp, D. M., Effect of Fullerenes on Crystallization-Induced Aggregation in Polymer Photovoltaics Casting Solutions. *Macromolecules* 2011, 45, (2), 1046-1055.
25. Xu, W.; Li, L.; Tang, H.; Li, H.; Zhao, X.; Yang, X., Solvent-Induced Crystallization of Poly(3-dodecylthiophene): Morphology and Kinetics. *The Journal of Physical Chemistry B* 2011, 115, (20), 6412-6420.
26. Xu, W.; Tang, H.; Lv, H.; Li, J.; Zhao, X.; Li, H.; Wang, N.; Yang, X., Sol-gel transition of poly(3-hexylthiophene) revealed by capillary measurements: phase behaviors, gelation kinetics and the formation mechanism. *Soft Matter* 2012, 8, (3), 726-733.
27. Chang, M.-Y.; Huang, Y.-H.; Han, Y.-K., Aggregation, crystallization, and resistance properties of poly(3-hexylthiophene-2,5-diyl) solid films gel-cast from CHCl3/p-xylene mixed solvents. *Organic Electronics* 2014, 15, (1), 251-259.

28. Keum, J. K.; Xiao, K.; Ivanov, I. N.; Hong, K.; Browning, J. F.; Smith, G. S.; Shao, M.; Littrell, K. C.; Rondinone, A. J.; Andrew Payzant, E.; Chen, J.; Hensley, D. K., Solvent quality-induced nucleation and growth of parallelepiped nanorods in dilute poly(3-hexylthiophene) (P3HT) solution and the impact on the crystalline morphology of solution-cast thin film. *CrystEngComm* 2013, 15, (6), 1114-1124.
29. Seidler, N.; Lazzerini, G. M.; Destri, G. L.; Marletta, G.; Cacialli, F., Enhanced crystallinity and film retention of P3HT thin-films for efficient organic solar cells by use of preformed nanofibers in solution. *Journal of Materials Chemistry C* 2013, 1, 7748-7757.
30. Ballauff, M., Phase equilibria in rodlike systems with flexible side chains. *Macromolecules* 1986, 19, (5), 1366-1374.
31. Schweizer, K. S., Order–disorder transitions of π-conjugated polymers in condensed phases. I. General theory. *The Journal of Chemical Physics* 1986, 85, (2), 1156-1175.
32. Newbloom, G. M.; Kim, F. S.; Jenekhe, S. A.; Pozzo, D. C., Mesoscale Morphology and Charge Transport in Colloidal Networks of Poly(3-hexylthiophene). *Macromolecules* 2012, 44, (10), 3801-3809.
33. Hammouda, B., SANS from Heterogeneous Polymer Mixtures - A Unified Overview. *Advances in Polymer Science* 1993, 87-133.
34. Mittelbach, P., *Acta Physica Austriaca* 1961, 14, 185-211.
35. Prosa, T.; Winokur, M.; Moulton, J.; Smith, P.; Heeger, A., X-Ray Structural Studies of Poly(3-alkylthiophenes) - An Example of an Inverse Comb. *Macromolecules* 1992, 4364-4372.
36. Lan, Y.-K.; Huang, C.-I., A Theoretical Study of the Charge Transfer Behavior of the Highly Regioregular Poly-3-hexylthiophene in the Ordered State. *The Journal of Physical Chemistry B* 2008, 112, (47), 14857-14862.
37. Li, J.; Yuan, B.; Liu, X.; Xu, H., Microengineering of Supramolecular Soft Materials by Design of the Crystalline Fiber Networks. *Crystal Growth & Design* 2010, 2699-2706.
38. Koppe, M.; Brabec, C.; Heiml, S.; Schausberger, A.; Duffy, W.; Heeney, M.; McCulloch, I., Influence of Molecular Weight Distribution on the Gelation of P3HT and Its Impact on the Photovoltaic Performance. *Macromolecules* 2009, 42, 4661-4666.
39. Richards, J. J.; Weigandt, K. M.; Pozzo, D. C., Aqueous dispersions of colloidal poly(3-hexylthiophene) gel particles with high internal porosity. *Journal of Colloid and Interface Science* 2011, 364, (2), 341-350.
40. Kim, B.-G.; Jeong, E. J.; Park, H. J.; Bilby, D.; Guo, L. J.; Kim, J., Effect of Polymer Aggregation on the Open Circuit Voltage in Organic Photovoltaic Cells: Aggregation-Induced Conjugated Polymer Gel and its Application for Preventing Open Circuit Voltage Drop. *Acs Applied Materials & Interfaces* 2011, 3, (3), 674-680.
41. *Handbook of Chemistry and Physics: 83rd Edition*. CRC Press LLC: Davers, MA, 2002.

Chapter V

Structure Characterization and Properties of Metal-Surfactant Complexes Dispersed in Organic Solvents

In order to make the synthesis of poly(3,4-ethylenedioxythiophene) (PEDOT) possible in organic solvents, it is necessary to develop a method to integrate the reactants in an organic solvent dispersion. The synthesis route chosen for the PEDOT polymerization is shown in equation 5.1[1]. Using this synthesis route, iron (III) ions will oxidize the EDOT monomers and subsequently come together to form the polymer chains. Meanwhile, the iron(III) gets reduced into iron(II). In order to polymerize PEDOT in the an organic solvent, it is necessary to create a stable dispersion of the iron(III) ions. Metal ions are not soluble in solvents with low polarity[2]. For this reason, it is necessary to synthesize a complex that pairs the metal ions with an anionic surfactant in order to stabilize the ions in solution and make the PEDOT polymerization possible.

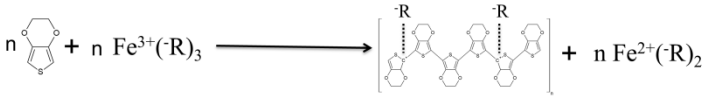

(Eq. 5.1)

Surfactants are frequently added to apolar solvents to fulfill roles such as lubrication, particle dispersion and to increase electric conductivity.[3] Micellization of surfactants that are soluble in apolar environments has been reported since 1953.[4] In contrast with aqueous micellization, which is usually driven by an increase in the entropy of water,[5] strong intermolecular forces between the hydrophilic sections of the surfactant

molecules drive aggregation into micelles when the solvent has a low dielectric constant.[6] Micelles in apolar media have hydrophobic tails exposed towards the solvent, shielding the cores that contain the polar head groups of the surfactant, the surfactant counterions and any water molecules that may be present in the system.[3, 5] Because of this, these structures are frequently termed 'inverse' micelles. Micellization in apolar media is strongly dependent on the type of surfactant, solvent and the quantity of residual water that is present.[7] These parameters affect the critical micelle concentration (CMC) and the degree of surfactant dissociation.[7]

Inverse micelles are known to stabilize ions in apolar media. Due to the low dielectric constants of the solvents, Coulombic attraction in apolar media can affect ions over long distances (i.e. a dielectric constant of ~2 causes the Bjerrum length to reach up to 30 nm, compared to the 0.7 nm in aqueous media).[3, 8, 9] Furthermore, in the case of micelles that carry a net charge, steric interactions from the bulky surfactant tails keeps them separated enough to prevent interactions.[9]

Commercial surfactants such as TWEEN, OLOA and SPAN readily produce inverse micelles when dispersed in apolar media.[10-13] These surfactants share the characteristic of having long and bulky aliphatic chains. Unfortunately, a complete understanding of the mechanisms that lead to self-assembly in apolar solvents is challenging due to the ill-defined chemical composition of these commercial products.[7] For example, depending on the surfactant and the solvent, the aggregation number of changes gradually as the surfactant concentration increases.[2, 7] In these cases a critical micelle concentration (CMC) is difficult to determine accurately and the distribution of micelle sizes is also very broad. Other systems, such as sodium dioctyl sulfosuccinate

(Na:AOT), behave more similar to aqueous micelles and their aggregation number is independent of concentration.[7] Yet, the aggregation number of Na:AOT is also strongly dependent on the solvent.[14] Usually, single-tailed surfactants such as sodium dodecyl benzene sulfonate (Na:DBSo) and sodium dodecyl sulfate (Na:DSa) are incapable of self-assembly in apolar solvents due to their very low solubility.

It has been previously shown that it is possible to introduce stable, multivalent, metallic ions in apolar media by pairing them with amphiphilic surfactant tails.[15] Several multivalent metal surfactant complexes have been investigated including Mg^{2+}, Ca^{2+}, Co^{2+}, Cu^{2+}, Al^{3+}, Gd^{3+}, Fe^{3+}, and Ho^{3+}.[16-26] Depending on the metal ion, the conformation of the inverse micelles can be spherical, ellipsoidal or cylindrical. The hydrated radius of the core of these inverse micelles, also referred to as microemulsions, is also affected by the metal ion. The size of the hydrated core radius modifies the curvature and alters the shape and size of the metal-surfactant complexes.[26] Metal ions also alter the properties of the systems enabling use in applications such as templates for metallic nanoparticles,[27-29] catalysis,[30] luminescence,[23] and nanomagnets,[16, 31, 32] among others.

The present work is a systematic study of the behavior of dioctyl sulfosuccinate (AOT) and dodecylbenzene sulfonate (DBSo) when associated with several multivalent metal ions. Specifically, it focuses on the structure and properties of these surfactants while self-assembling in toluene and methanol that act as model organic solvents of variable polarity. Metal ions investigated include aluminum (Al), iron (Fe) and vanadium (V). Electrochemical and charge transport properties of surfactants are also reported. While electrical properties of AOT attached to multivalent metal ions have been reported in the past,[9, 33] the present work provides detailed structural analyses of self-assembly and

also extends the types of metals that have been synthesized and analyzed. Redox activity of metal ions in these complexes is also probed. Typically, measuring electrochemical activity in solvents with low dielectric constants, such as toluene, is challenging due to the low conductivity of the medium and the low concentrations of active species that can be achieved.[34] Here, surfactant complexes significantly increase conductivity to show redox activity for iron and vanadium ions in toluene. Metal complexes with DBSo are also synthesized and analyzed for the first time. The self-assembly, structure and properties of DBSo complexes with multivalent metal ions has not been reported in the past.

The structure of metal-surfactant complexes is evaluated in-depth with small angle neutron and X-ray scattering (SANS, SAXS) as well as with molecular dynamic (MD) simulations. By correlating experimental and computational results a detailed picture of the structure of the complexes is achieved. These results provide detailed information on the effects that each of the variables has on the structure and properties. The structural evolution as a function of time and water content is also tracked to assess their long-term stability.

Materials and Methods

Synthesis of organometallic complex.

Sodium dodecyl benzene sulfonate, dioctyl sulfosuccinate sodium and sodium dodecyl sulfate are purchased from Sigma-Aldrich (St Louis, MO) and used as received. Vanadium III chloride, iron III chloride and aluminum III chloride are also purchased from Sigma-Aldrich. Metal chlorides are dispersed in deionized water and filtered before

use. The surfactant is dissolved in water (figure 5.1 a) and metal chloride is added slowly to the surfactant solution while stirring (figure 5.1 b) until a precipitate forms (figure 5.1 c). The precipitate is filtered out and thoroughly washed with water in order to remove sodium, chlorine and any unreacted surfactant or metal ions. The product is dried at room temperature for at least 24 h in a watch glass under vacuum (figure 5.1 d). After drying, the organometallic complex is transferred to a vial and stored under vacuum until used.

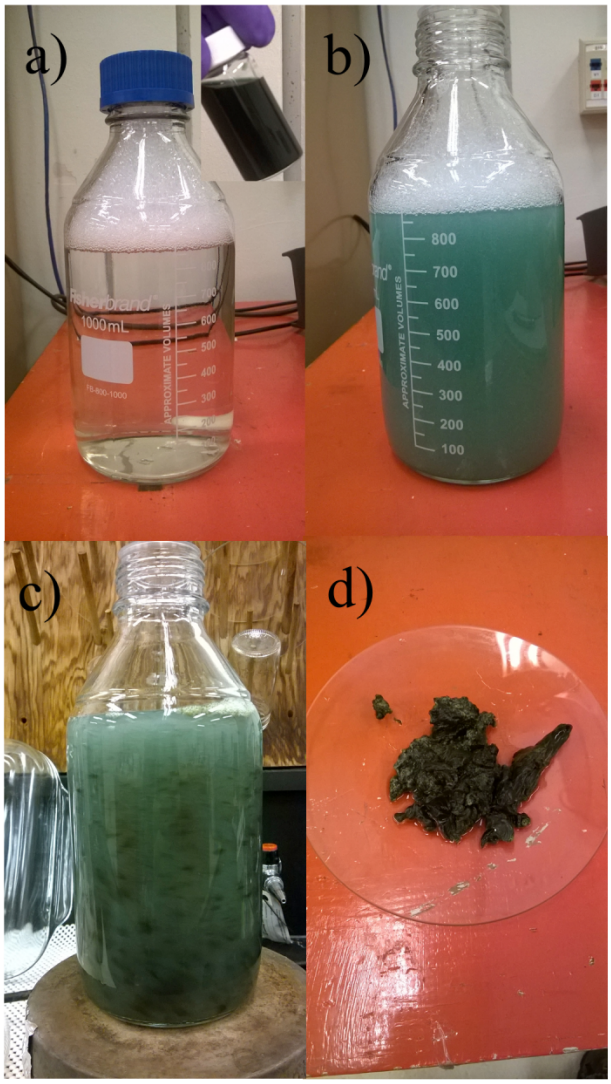

Figure 5.1: Pictures of the stages of the synthesis of the organometallic salt V:DBSo. a) Shows the sodium dodecylbenzene sulfonate (SDBS) detergent dissolved in water at a concentration of 7 g/L.

Insert a) Vanadium chloride solution in water, on a concentration that exceeds the amount of the vanadium necessary to achieve full reaction (~22 g/L). b) State of the SDBS dispersion after partial addition of the vanadium solution. At this point in the procedure, enough vanadium has been added to form V:DBSo salt insoluble in water, but not enough to make the salt fully aggregate. c) State of the sample after the entire vanadium solution is added. The resulted organometallic salt forms big aggregates that could be easily separated by filtration. d) Picture shows the filtered and dried V:DBSo.

X-ray Photoelectron Spectroscopy

X-ray Photoelectron Spectroscopy (XPS) is performed at the surface analysis recharge center (SARC) at the University of Washington. The Surface Science Instruments (Mumbai, India) S-Probe is used. The instrument uses an Al Kα X-ray source. The area probed is approximately 800 μm in diameter using a pass energy of 150 eV. Detailed scans are taken of the regions where the metal (iron, vanadium or aluminum), sulfur, sodium and chlorine energy peaks appear in order to obtain a higher resolution on the content of these elements. Samples are prepared by spin casting a 50 mM dispersion of the organometallic complex in toluene over a glass substrate. At least three depositions are performed for each sample. The films are placed under vacuum overnight to ensure the evaporation of the solvent, and to prevent the formation of bubbles when the samples are placed in the instrument chamber.

Small angle scattering.

Neutron and X-ray scattering is performed on 50 mM dispersions of the salts in various solvents. Small angle neutron scattering (SANS) is performed at the National Institute of Standards and Technology (NIST) Center for Neutron Research. The experiment is performed on the NGB-30 instrument, using a standard configuration to

cover a wide range of wave-vector values ($0.002 < q < 0.3$ Å^{-1})[35] with wavelengths of 6 and 8.4 Å. Organometallic complexes for SANS are dispersed in deuterated versions of the solvents (Cambridge Isotopes, Tewksbury, MA) in order to decrease the scattering background and to increase the contrast between the solvent and the organometallic complex. All samples are exposed to the neutron beam using demountable Ti cells with quartz windows and a 1 mm path length. The data is reduced and corrected by accounting for background radiation and scattering from the empty cell. The data is also normalized to an absolute scale by measuring the incident neutron flux. Data reduction is performed using the standard NIST Igor-based macros.[36]

Small angle X-ray scattering (SAXS) is performed on exactly the same samples, two weeks after the SANS experiments. A small angle X-ray Scattering (SAXS) instrument (Anton-Paar, Graz, Austria) with a line-collimation system using a Cu Kα source with a wavelength of 1.54 Å is used. Fujifilm (Greenwood, SC) image plates and a Perkin-Elmer Cyclone (Covina, CA) image plate reader are used to acquire the data. The SAXSQuant software is used to reduce the two dimensional data to a one-dimensional, intensity (I) versus scattering vector (q) plot.

Cyclic Voltammetry

The cyclic voltammetry (CV) characteristics are measured with a Reference 600 potentiostat (Gamry Instruments, Warminster, PA) by using a traditional three-electrode configuration on a C3 cell stand (BASi, West Lafayette, IN). Glassy carbon is used as working electrode and a platinum wire as the counter electrode. The quasi reference electrode is prepared by immersing a silver wire into 0.1 M ferrocene and 0.1 M tetrahexylamonium bromide (THABr) (Sigma-Aldrich) dispersed in toluene. The

measured sample is composed of the organometallic complexes dispersed in toluene at different concentrations. 0.5 M of THABr is used as a supporting electrolyte. The experiments are conducted by using a 100 mV/s scan rate with argon purging at room temperature. Reference to standard hydrogen electrode (SHE) is achieved by comparing the redox potential of our reference electrode to reported values of the redox potential of ferrocene in DMSO.[34]

Conductivity

Conductivity is measured by placing approximately 0.25 mL of an organometallic complex dispersion between two stainless steel electrodes with dimensions 25 mm in diameter and 0.5 mm gap between them. The concentration of the dispersion is varied from 0.5 to 500 mM in toluene and 0.01 to 50 mM in methanol. A DC bias of 1 V is applied using an Agilent e4980a LCR Meter (Santa Clara, CA). The temperature of the system is held constant at 25°C.

Molecular Dynamic Simulations

Molecular dynamics simulations are conducted to gain insight into the atomic scale structure of the organometallic complexes. All systems contain 8 Fe^{3+} ions and 24 surfactant molecules in a cubic box with a side length of 8.0 nm filled with organic solvent. The four systems that are considered are: (a) Fe:AOT in toluene, (b) Fe:AOT in methanol, (c) Fe:DBSo in toluene and (d) Fe:DBSo in methanol. The initial configuration of the simulation is generated with Packmol.[36] System details appear in Table S1. The general AMBER force field is used to describe surfactant and solvent molecules.[37] Electrostatic point charges are developed by fitting to HF/6-31G(d) electronic structure

calculations in Gaussian 09 with the RESP method in antechamber. The Fe^{3+} Lennard-Jones parameters are taken from the literature,[38] and the charge is assumed to be +3e. GROMACS 4.6 is used to perform MD calculations. Lennard-Jones potentials are shifted to zero at 1.2 nm. Particle mesh Ewald summation is used for long-range electrostatics with periodic boundary conditions. Bonds are constrained with the LINCS algorithm in order to allow for an integration timestep of 2 fs. All simulations are kept at 310 K by the application of a stochastic velocity-rescaling thermostat. Systems are first minimized over 10,000 steps with the steepest descent method, pressure is then equilibrated to 1 bar with a 20 ns simulation with a Berendsen barostat, and subsequent production runs of 200 ns in length use the Parrinello-Rahman barostat at the same pressure.

Table 5.1: Number of molecules of each type in the simulation boxes. After pressure equilibration cubic box-side length ranges from 6.8 to 7.8 nm depending on the system. Density fluctuates are small after equilibration.

	Number of molecules			
Molecule	**DBSo-Methanol**	**DBSo-Toluene**	**AOT-Methanol**	**AOT-Toluene**
DBSo	24	24	-	-
AOT	-	-	24	24
Fe^{3+}	8	8	8	8
Methanol	4470	-	4470	-
Toluene	-	2448	-	2448

Synthesis, Elemental Conformation and Solvent Compatibility.

AOT, DBSo and dodecyl sulfate (DSa) complexes with the three metal ions (aluminum, iron and vanadium) are synthesized as described in the methods section of this manuscript. The complexes are dried and stored under vacuum after the synthesis in order to decrease the amount of water trapped within them as much as possible, however no extra steps are taken to reduce the water content any further. Because the synthesis is performed in water and because metallic ions are hygroscopic, the complexes contain a finite amount of water before being dispersed in any solvent. Water content of the salts dried under vacuum or at least 24 hours is measure by using Karl-Fischer titration. The amount of water ($w=[H_2O]/[Surfactant]$) varies depending of the surfactant used. For DBSo complex w is 0.6 while for AOT complex w is as high as 2. Based on the w values, the amount of water in the salts is considered low.[15]

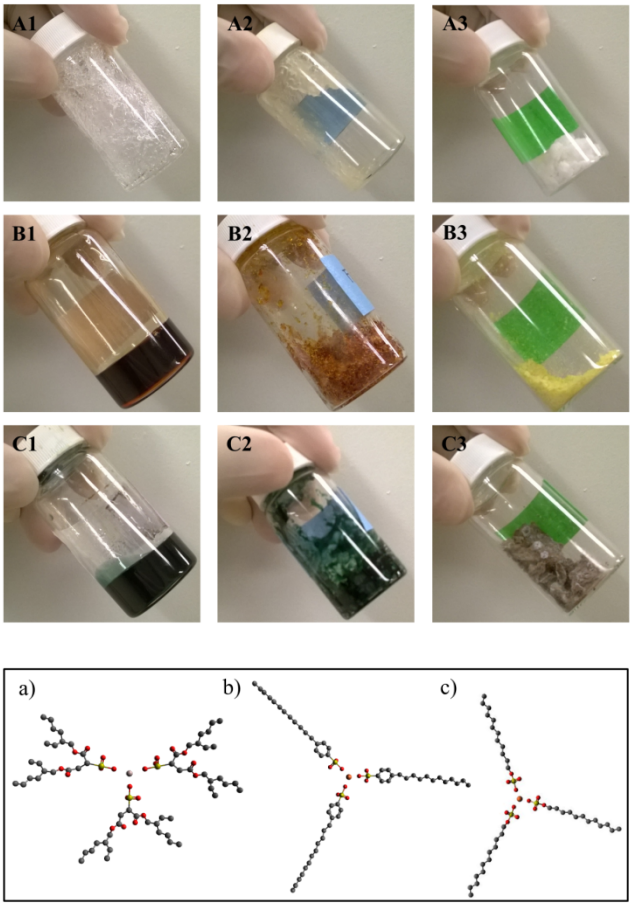

Figure 5.2: Pictures of the purified and dried organometallic complexes. The samples in row A are aluminum, row B iron and row C vanadium complexes. Column 1 contains AOT, column 2 is DBSo and column 3 contains DSa complexes.

Figure 5.2 shows pictures of the purified and dried organometallic complexes. The samples on the top row are aluminum-based, middle row iron-based and bottom row vanadium-based complexes. Column 1 contains metals paired with AOT, column 2 paired with DBSo and column 3 contains DSa complexes. Notice the different colors of the samples depending on which metal is used. Aluminum produces white/transparent complexes, iron-based complexes turn out to be orange/yellow, and the use of vanadium results in a green/lavender hue. The surfactant pair plays a major role in the physical conformation of the organometallic complexes. AOT complexes result in a very viscous

paste that can be readily dispersed in various organic solvents, and AOT-metal complexes behave like a liquid relaxing in the vial when left undisturbed. DBSo complexes result in a waxy solid that also disperses in various organic solvents. Finally, DSa results in a powder that can only be dispersed in alcohols, which shows how big of an effect the surfactant tail plays in the complex interactions. DSa seems to facilitate the ordering of the metal-surfactant salts, a situation that cannot be reversed by the apolar solvent alone. However, when the DSa complexes in toluene are heated to 75ºC, the solubility of the complex increases and ultimately forms dispersions similar to the ones obtained with AOT and DBSo (figure 5.3). The mixture of the salt in toluene close to room temperature has visible aggregates and it has a yellow coloration, its SAXS profile contains a rapid increase in the intensity at low-q which corroborates the presence of big aggregates. The profile also contains a series of peaks at high-q, these peaks indicate the presence of crystalline domains in the sample. The high crystallinity of the salts is most likely the reason for the poor solubility of the complex in toluene, since the solvent probably does not have a mechanism to disrupt the crystals. As the temperature of the sample is increased there is a decrease in the slope at low-q and the peaks at high-q start to disappear. At 75 ºC the crystallinity peaks fully disappear and the low-q behavior is similar to other iron complexes. The appearance of the mixture also changes, going from a cloudy yellow mixture to an orange and clear (without visible aggregates) dispersion. The cartoons at the bottom of figure 5.2 show the hypothesized molecular structure of the surfactant, and the ratio in which the surfactant molecules interact with the metallic ion.

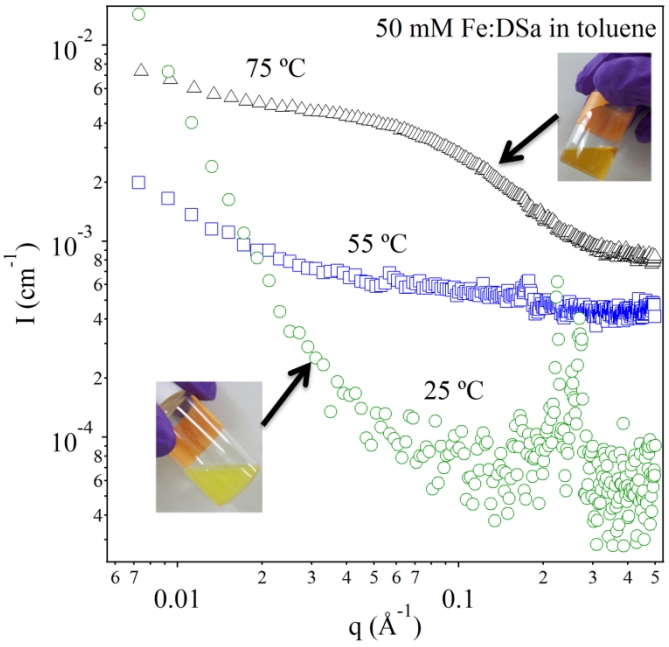

Figure 5.3: Small angle x-ray scattering of Fe:DSa dispersed in toluene at three different temperatures. The insert pictures represent the state of the dispersion at 25°C and 75°C.

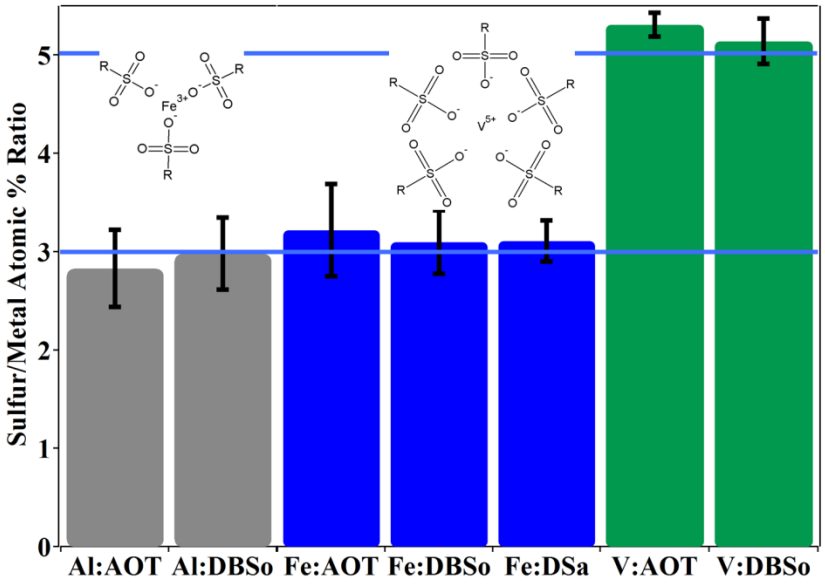

Figure 5.4: Sulfur/metal atomic percent ratio obtained from the XPS results of seven different complexes. Insert: Cartoon representation of a charge-balanced iron-sulfonate and vanadium complex.

X-ray photoelectron spectroscopy (XPS) analysis of the resulting organometallic complexes confirms the absence of sodium (from anionic surfactants) and chlorine (from metal salts), which indicates that they remain dissolved in water and are fully washed out from the product. The atomic percent ratio of sulfur/metal is also obtained from XPS. This ratio is used to infer the purity of the sample and also to corroborate the oxidation state of the metallic ion. A ratio of 3:1 sulfur to metal is expected for most samples because 3 surfactant chains are needed to balance out the +3 charge of the metal ion (insert in figure 5.4). Aluminum and iron complexes show the expected 3:1 atomic ratio (figure 5.4). However, vanadium samples deviate from this ratio and instead show an atomic ratio of 5:1 (insert in figure5.4). This suggests an excess of surfactant from the expected value of a +3 valence. The ratio of 5:1 (Sulfur:Vanadium) suggests that vanadium ions may be further oxidized and have a valence of +5. This observation is corroborated by UV-vis spectroscopy of the precursor (VCl_3) that is used to synthesize the complex (figure 5.5). The UV-vis spectra is typical of an oxidation state of +5 for vanadium[40] which is also in agreement with XPS. For the rest of the manuscript the notations "Fe:surfactant" and "Al:surfactant" will be used for the Fe^{3+} and Al^{3+} surfactant complexes, respectively, and "V:surfactant" will be use for the V^{5+} complexes.

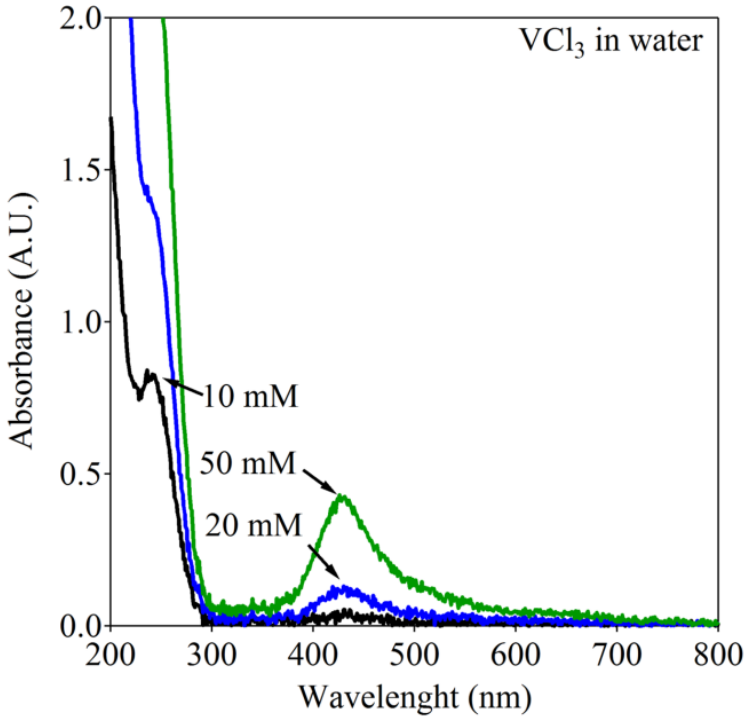

Figure 5.5: UV-vis of VCl_3 aqueous solution at different concentrations. The peak at ~400 nm is characteristic of V(V) oxidation steps, furthermore the lack of peaks at 600, 800 and 850 indicates the absence of the other oxidation states of vanadium.[40]

Organometallic complexes are dispersible in a wide range of organic solvents. In general, alcohols efficiently disperse all of the metallic complexes. DBSo, AOT and DSa organometallic complexes can be readily dispersed in methanol, ethanol, isopropyl alcohol, hexanol, and octanol. Concentrations as high as 700 mM of the AOT metal complex is readily achieved in octanol. At this concentration, the samples are viscous due to the strong interactions of the complexes. Dispersions of up to 2 M are also achieved in small chain alcohols (e.g. methanol, ethanol). The DBSo and AOT complexes also show very good solubility in halogenated solvents such as chloroform and dichlorobenzene. Concentrations of up to 500 mM can be produced in toluene and benzene for DBSo and

AOT organometallic complexes. DBSo and AOT organometallic complexes can also be dispersed in short alkane solvents (e.g. hexane), but not in long chain alkanes (e.g. dodecane).

Neutron and X-ray Small-Angle Scattering of Organometallic Complexes and Simultaneous Analysis.

Small angle scattering is used to probe the structures formed by the organometallic complexes dispersed in organic solvents. Due to the amphiphilic nature of the complexes, they form inverse micelles when dispersed in solvents with low dielectric constants. In order to obtain a clear analysis of the conformation of the samples, small angle neutron (SANS) and X-ray (SAXS) scattering is performed on all samples. For SAXS, scattering contrast depends on the local electron density. For this reason, SAXS primarily probes the size and shape of the metal core and the surfactant head groups. Deuterated solvents are used in all samples in order to increase neutron scattering contrast between the solvents and the aliphatic tail groups. Deuterium isotopes in the solvent create a high scattering contrast with the hydrogen atoms in the surfactant tails so that SANS is ideally suited to characterize the shape and size of the surfactant tails.

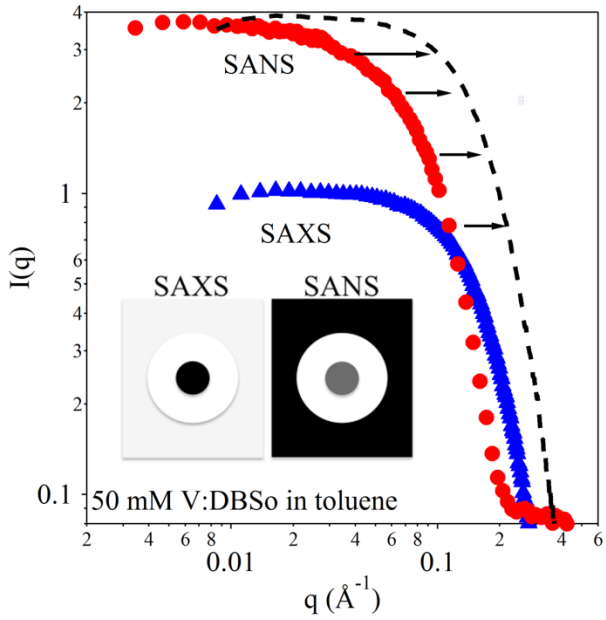

Figure 5.6: SANS and SAXS profiles of a 50 mM V:DBSo organometallic complex dispersed in toluene. The dashed curve is the SAXS profile shifted vertically to highlight the differences with the SANS profile. Insert: Pictorial representation of the difference in the scattering length density of the system using neutrons vs. x-rays.

Figure 5.6 shows the SANS (circles) and SAXS (triangles) profiles of a 50mM V:DBSo organometallic complex, dispersed in toluene. Both profiles show a Guinier region in the q range of ~0.2 > q > 0.06 Å^{-1}. The Guinier region in the SAXS profile is shifted to higher-q relative to the SANS profile. The metal surfactant complexes can be described as corresponding to an electron dense core and a hydrocarbon shell. The core is primarily composed of metal ions and head groups of the surfactants as well as any trace quantities of water that may be present in the solvent. The shell region of the structure is formed by aliphatic tails of the surfactants that are exposed towards the solvent to shield the polar core. An accurate description of the structure of these complexes can be obtained by simultaneously analyzing the SANS and SAXS scattering data. Both profiles

are fit with a core and shell form factor while constraining the size, shape and volume fraction to be equal. A rigorous and reliable description of the system is achieved by simultaneously analyzing two independent experimental profiles that are sensitive to different regions of the same structure. This ensures results that are significantly more reliable than the traditional independent interpretation of SANS and SAXS experiments.

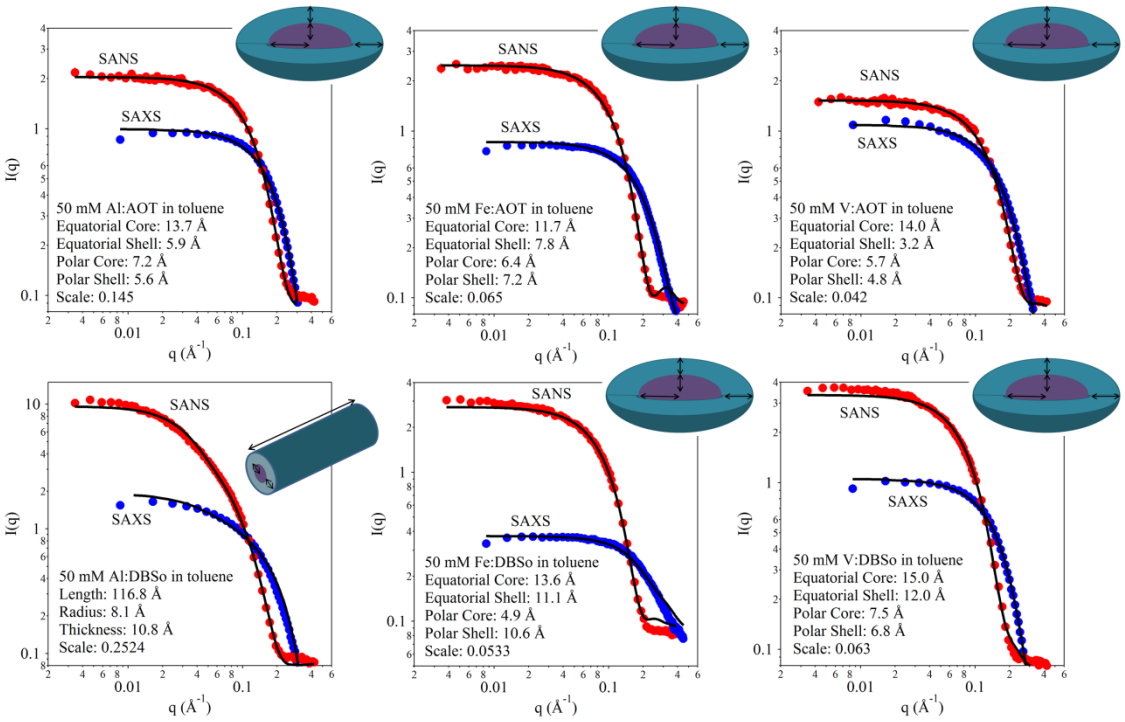

Figure 5.7: SANS and SAXS scattering profiles of the different organometallic salts used in this study, dispersed in toluene. The black lines are the simultaneous fits obtained using the previously described form factors. The parameters from these fits can be found in Table 5.2 in the manuscript. The insert image is a pictographically representation of the model use in the fits.

After evaluating several different core and shell form factors (i.e. sphere, ellipsoid, cylinders), the best fit for most samples in toluene is obtained from a core and shell ellipsoid model (all fits are shown in figure 5.7).[41-43] The only complex that is not adequately fit with this model is Al:DBSo. The scattering profile for this complex is qualitatively different from the profiles of all other dispersions. For example, the scattering intensity is about three times higher than for other samples and the Guinier region appears at a lower-q. These two changes suggest the existence of larger domains. This is also consistent with the higher viscosity that is visibly observed when compared to the other dispersions at the same concentration. The model that best describes the structure of the Al:DBSo complex is a core and shell cylinder model.[41-43] Table 5.2 lists all parameters obtained from simultaneous SAXS/SANS fits of complexes in toluene. The core size does not vary much from metal to metal. The equatorial radius of the ellipsoid is always 12-15 Å, while the polar radius remains around 5-8 Å. The size of the shell varies more significantly based on the surfactant that is used in the organometallic complex. Metal:DBSo complexes have a shell thickness of 11-12 Å that almost matches the fully extended size of a DBSo chain (13.3 Å).[44] Metal:AOT complexes have a shell thickness considerably smaller (6-8 Å) that is consistent with the short, branched chain (11.4 Å at its maximum extension).[45]

Table 5.2: Parameters obtained from the simultaneous fitting of the SANS and SAXS data of the different organometallic complexes dispersed in toluene using the core and shell ellipsoid and core and shell cylinder model.

		Organometallic Complex					
		Al:AOT	**Al:DBSo**	**Fe:AOT**	**Fe:DBSo**	**V:AOT**	**V:DBSo**
Parameter	**Core and Shell Model**	Ellipsoid	Cylinder	Ellipsoid	Ellipsoid	Ellipsoid	Ellipsoid
	$Radius_{Eq}$ Core (Å)	13.7	--	11.7	13.6	14.0	15.0
	$Thickness_{Eq}$ (Å)	5.9	--	7.8	11.1	3.2	12.0
	$Radius_{Pol}$ Core (Å)	7.2	--	6.4	4.9	5.7	7.5
	$Thickness_{Pol}$ (Å)	5.6	--	7.2	10.6	4.8	6.8
	Length (Å)	--	116.8	--	--	--	--
	Radius (Å)	--	8.2	--	--	--	--
	Thickness (Å)	--	10.9	--	--	--	--

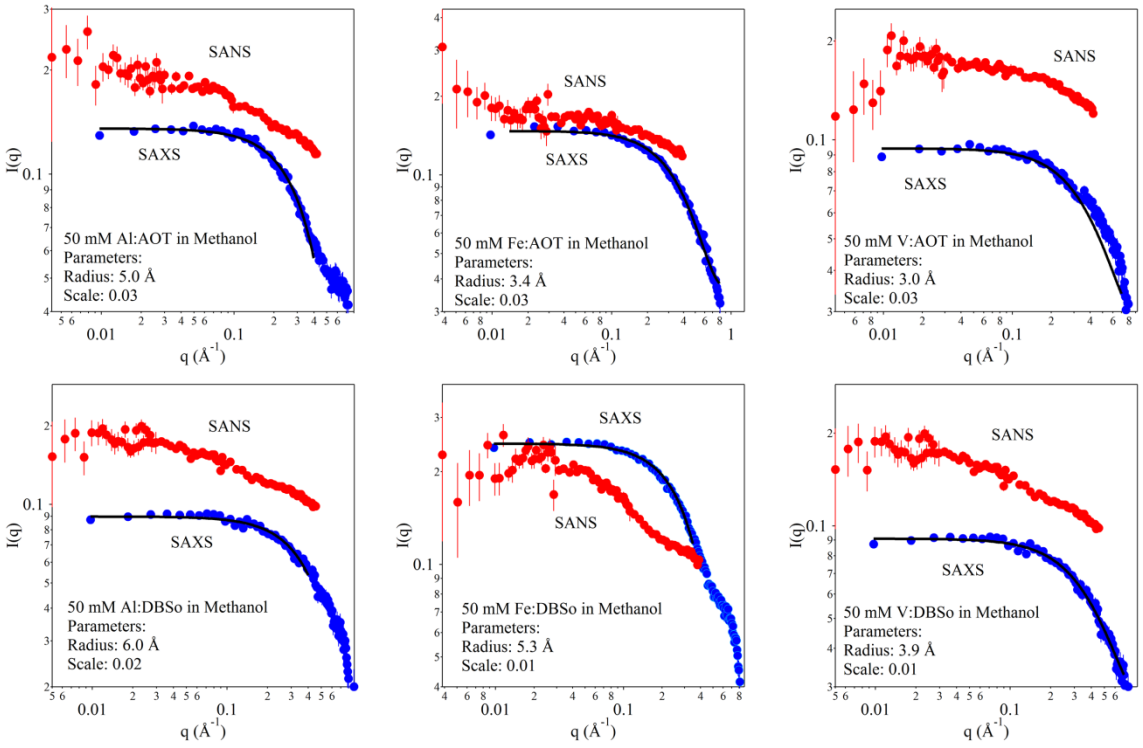

Figure 5.8: SANS and SAXS scattering profiles of the different organometallic salts used in this study, dispersed in methanol. The black lines are the simultaneous fits obtained using the previously described form factors. The parameters from these fits can be found in Table 5.3.

For organometallic complexes dispersed in methanol the Guinier regions are shifted to higher-q, indicating the presence of smaller features when compared to toluene. The Guinier region is very close to the maximum-q that is measurable with this neutron scattering instrument. This means that small features are barely visible in some of the SANS profiles but they are still very apparent in the SAXS profiles due to the lower incident wavelength and a larger maximum detector angle. Due to the limited resolution of the SANS profiles, simultaneous fits are not attempted on samples in methanol. Instead a simple sphere form factor is fit to the SAXS data to model the dimensions of the polar core (figure 5.8). Table 5.3 lists the radius obtained from the fits performed to the SAXS scattering profiles of all the complexes dispersed in methanol. The results point towards a more dispersed conformation of the organometallic complexes in methanol when compared to the toluene samples. These results indicate that methanol drastically disrupts the complex structure and keeps the metal ions apart. The radius of the core stays fairly constant regardless of the metal center that is used (3-6 Å); however, DBSo complexes consistently show larger radii than their AOT counterparts. Evidence of a different conformation for DBSo samples is also qualitatively observed in SANS profiles. In order to obtain a scattering resolution that is sufficiently above background, the SANS profiles of concentrated samples (300 mM) in methanol are obtained. The scattering in figure 5.9 shows a peak at around 3 $Å^{-1}$ that suggests some of these samples are likely above the overlap concentration. Although this prevents accurate fitting to analytical form factors, qualitatively, the scattering profiles of the DBSo and the AOT complexes are very different. The scattering intensity for the DBSo samples is higher than for the AOT samples, which indicates bigger scattering elements. Additionally the

slope of the scattering in the range of 0.007 to 0.02 $Å^{-1}$ is steeper in the DBSo than in the AOT samples. This indicates a change in the form factor of the arrangement of the surfactants tails, DBSo probably having larger domains and dimensionality than AOT.

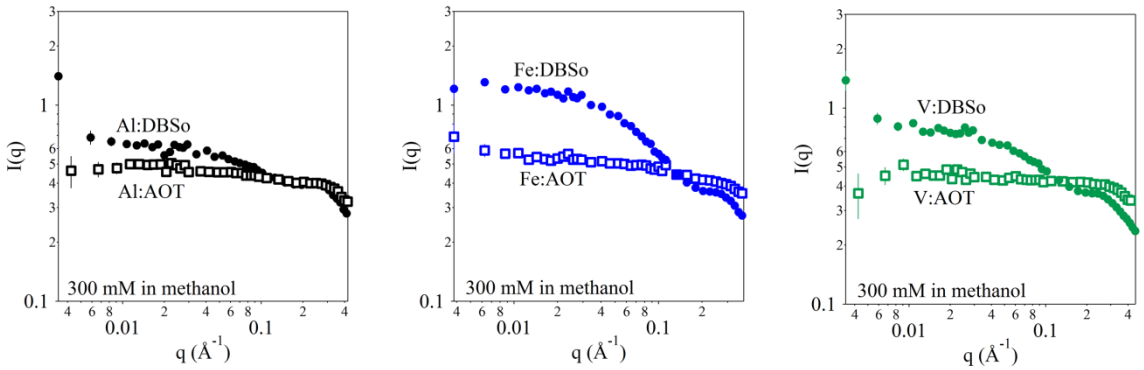

Figure 5.9: SANS profile of concentrated dispersion of metallic complexes in methanol.

Table 5.3: Parameters obtained from fitting of the SAXS data of the different organometallic complexes dispersed in methanol using the sphere model.

Sphere	Al:AOT	Al:DBSo	Fe:AOT	Fe:DBSo	V:AOT	V:DBSo
Radius (Å)	5.0	6.0	3.4	5.3	2.9	3.9

Molecular Dynamic Simulations of Organometallic Complex Dispersions.

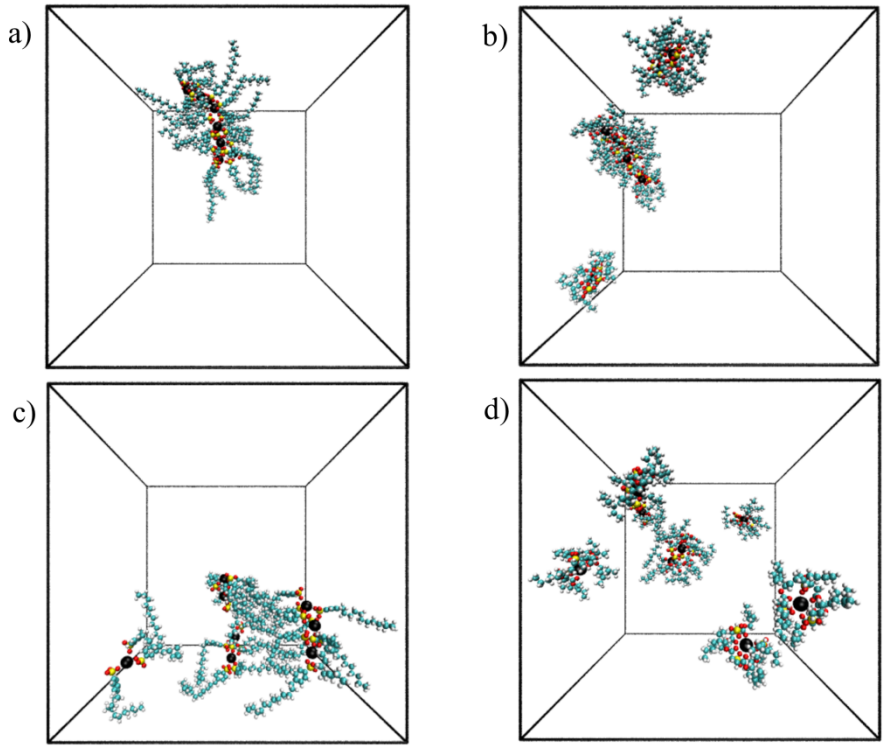

Figure 5.10: Molecular dynamic simulation of different iron complexes. a) Fe:DBSo in toluene, b)Fe:ATO in toluene, c)Fe:DBSo in methanol, d) Fe:AOT in methanol. Iron III ions are shown with a larger sphere size (black) in order to facilitate their identification.

Molecular dynamic simulations of the systems are performed in order to further corroborate the existence of the structures that are projected from small angle scattering experiments. Figure 5.10 shows the conformation of Fe:DBSo (figure 5.10a) and Fe:AOT (figure 5.10b) dispersed in toluene. All metal complexes are somewhat elongated but their small aspect ratio more accurately defines them as ellipsoids rather than cylinders. This result agrees very well with the small angle scattering models. Fe:AOT samples in toluene also aggregate into smaller domains when compared to Fe:DBSo. Yet, all structures in toluene contain multiple metal cores. For Fe:AOT, only about five iron cores

are found to complex together out of the eight that were included in the simulation box. The dimensions of the complex aggregate can be found in table 3. The dimensions of the Fe:AOT aggregates are 11.3 ± 1.2 Å in the equatorial radius and 8.8 ± 2.6 Å for the polar radius of the core, the AOT shell thickness is 8.4 ± 1.2 Å. These sizes are consistent with the ones obtained from the SAS data fitting (Table 5.2) which yielded 11.7 and 6.4 Å for the equatorial and polar radii respectively and a shell thickness of 7.2-7.8 Å. In contrast, all iron cores in the simulation box (eight) form part of the same DBSo micelle. The dimensions from the simulations (table 5.4) reveal an ellipsoid of 12.8 ± 1.5 Å equatorial radius and 4.9 ± 0.6 Å of polar radius and a shell thickness of 14.3 ± 1.6 Å. This again agrees well with the SAS data fitting which show dimension of 13.6 and 4.9 Å equatorial and polar radii with a shell thickness of 10.6-11.6 Å. The surfactant tails in the MD simulation are extended for both Fe:DBSo and Fe:AOT complexes in toluene. This shows that the differences in shell thickness obtained from SAS fits is directly related to the size of the surfactant tail.

A fully dispersed conformation is also observed in the simulation of Fe:AOT complexes in methanol (figure 5.10d). The metal cores are isolated from each other but still form stable complexes and the structures are similar to that suggested from the SAS models. In contrast, Fe:DBSo (figure 5.10c) complexes show aggregates of 2 to 3 ion cores in the MD simulation but appear to be dispersed according to SAS experiments of dilute samples (50 mM). DBSo tails also tend to interact with each other forming a sheet-like structure with intercalated DBSo tails in the simulation. This could corroborate the difference in the scattering profiles observed in concentrated samples (300 mM) in methanol between the AOT and the DBSo data (Figure 5.9). The dimension of the MD

aggregates once again matches the SAXS results. Fe AOT reveal single complex with a core radius if 3.3 ± 0.1 Å while the radius of the features found on the SAXS are 3.4 Å. The consistently larger radii of DBSo aggregates, when compared to AOT, observed in the scattering of the metallic complexes dispersed in methanol (Table 5.3) suggest that small multi-ion complexes may form for all metal:DBSo complexes.

Table 5.4: Dimension of the different structures formed by the metallic complexes obtained from the molecular dynamic simulations. The parameters are named the same way as in the small angel scattering models in order to obtain a direct comparison.

	Micellar Dimensions Obtained on Dynamic Simulations			
	Fe:DBSo		**Fe:AOT**	
Solvent	Toluene	Methanol	Toluene	Methanol
Core and Shell Model	Ellipsoid	Sphere	Ellipsoid	Sphere
$Radius_{Eq}$ Core (Å)	12.8 ± 1.5	---	11.3 ± 1.2	---
$Radius_{Pol}$ Core (Å)	4.9 ± 0.6	---	8.8 ± 2.6	---
$Thickness_{EII}$ (Å)	14.3 ± 1.6	---	8.4 ± 1.2	---
Radius (Å)	---	3.2 ± 0.6	---	3.3 ± 0.1
Radius (Two-Iron Complex) (Å)	---	5.6 ± 1.2	---	---
Thickness (Å)	---	15.6 ± 0.6	---	8.2 ± 1.1

The dispersed conformation of the metallic complexes is not only unique to methanol. Similar dispersed conformations are achieved with multiple alcohols (figure 5.11) indicating that the hydroxyl (OH) group interacts with the metal core and is responsible for their isolation. MD simulations show an average of 5.13 ± 0.41 and 3.20 ± 0.28 OH groups within 3 Å of the metallic ion for Fe DBSo and Fe AOT, respectively. This hints to a strong interaction between metal cores and alcohol functional groups that

facilitate the dispersion of the metal complexes. The strong metal-hydroxyl interaction could also explain the dispersion of DSa complexes in alcohols but not in any other organic solvent. Despite the general isolation of the metal ions from each other, MD simulations in methanol do not show signs of dissociation between the surfactants and the metal ions.

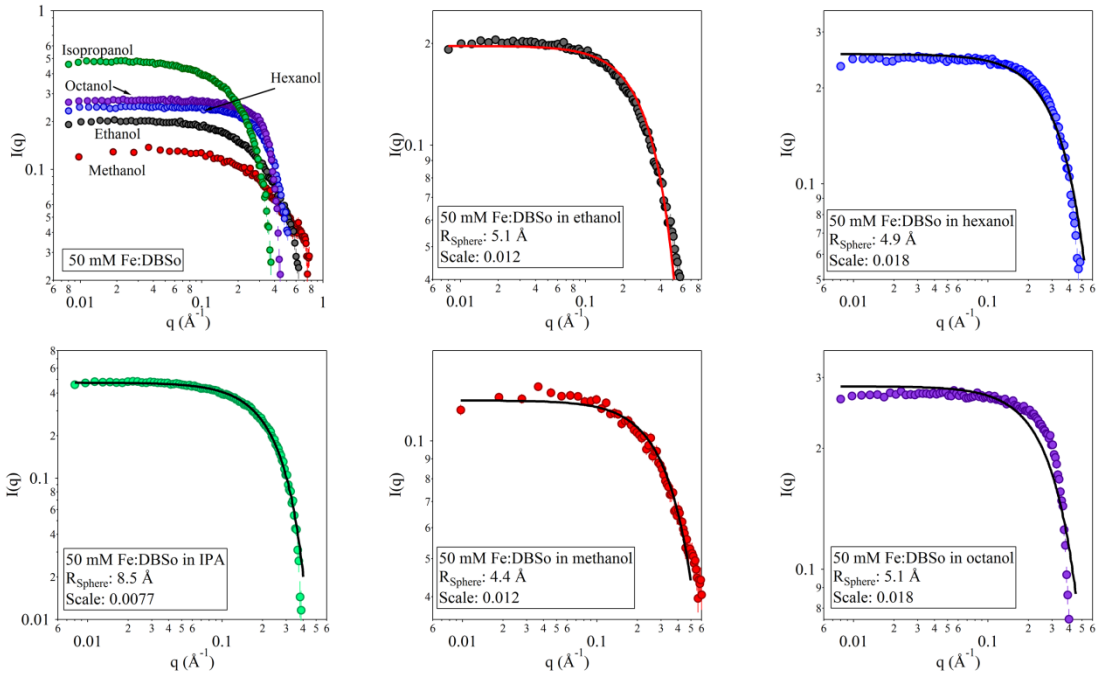

Figure 5.11: SAXS profile of Fe:DBSo dispersed in different alcohols. The figure also shows the fitting performed to the profiles using the sphere model.

Different alcohols are probed to characterize the behavior of the salt complex. The alcohol moiety seems to control the salt dissolution, and the length of the alcohol alkyl chains seems to have little to no effect. The position of the knee in the SAXS profile does not change in a wide range of alcohols. Only the isopropanol sample shows clear changes in scattering form factor for reason still not know. Figure 5.11 also shows the fits to the SAXS data in the different alcohols. For most of the solvents the fit reveals similar

dimensions (5-4 Å in radius) and similar scale factor. The difference in the intensity of the scattering profiles is caused by the contrast from the scattering length densities of the different alcohols. The fit for IPA hint for the formation of micelles in that solvent.

Aging of the Organometallic Complex Dispersions.

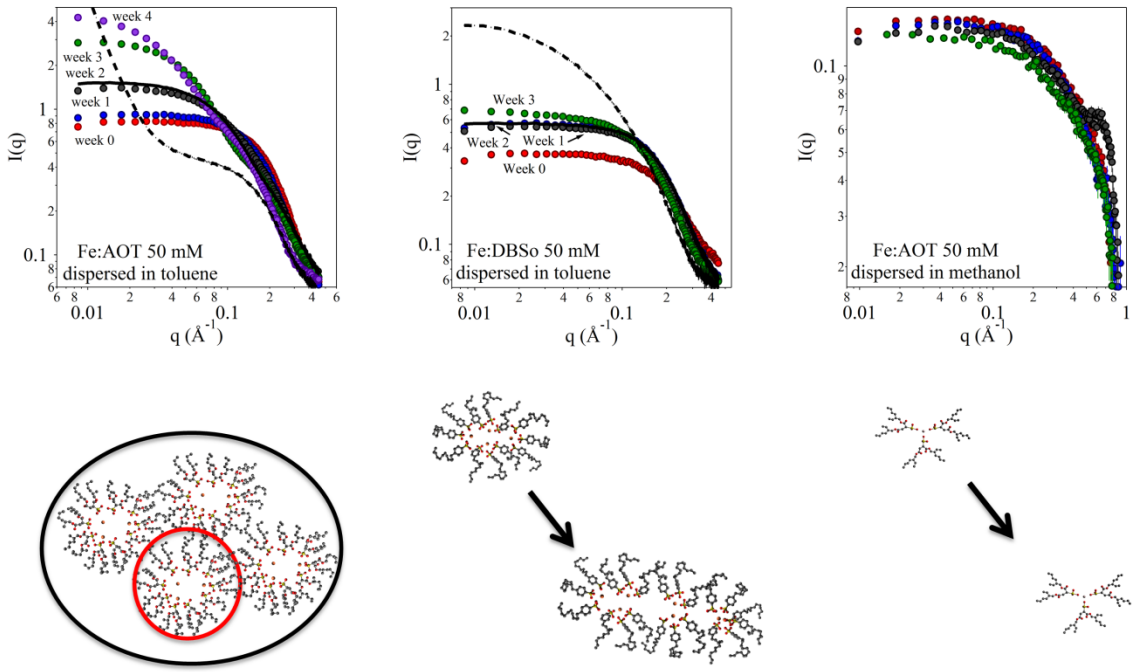

Figure 5.12: Evolution of the scattering of Fe:AOT dispersed in toluene (left), Fe:DBSo dispersed in toluene (center) and Fe:AOT dispersed in methanol (right). The samples are stored for up to 4 weeks at ambient conditions. The solid lines (left and center) represent the scattering profiles of the organometallic complex dispersions kept in a glove box for 5 weeks. Dashed lines (left and center) are the scattering profiles of organometallic complex dispersions stored in humid conditions for 5 weeks. Bottom: Cartoon representation of the behavior of the organometallic complexes when dispersed in toluene and methanol. The cartoons are based on the scattering profiles obtained at different aging stages.

The effect of aging on the complex aggregates dispersed in toluene and methanol is also tracked with SAXS. Fe:AOT, dispersed in toluene, shows a big change in the structural

conformation of the sample as a function of time. In the X-ray scattering profile, the Guinier region shifts to lower-q while the intensity of the scattering increases (figure 5.12, left graph). These are signs of growth of iron complexes. The scattering profile of Fe:AOT after 4 weeks starts to show a second feature: a Guinier region at around 0.03 $Å^{-1}$ and a shoulder at higher-q (0.15 $Å^{-1}$). The presence of this double feature indicates that the metallic complex domains are themselves aggregating into larger structures. The cartoon under the graph shows a possible conformation that can give rise to this type of scattering profile.[46] The Guinier region at low-q is probing the structure of the large cluster (encircled by the black line) while the shoulder at high-q results from the shape of the individual complexes (red circle). Fe:DBSo samples do not show a drastic change in form factor over the period of time that it is tracked (figure 5.12 middle). At the three-week mark the power-law exponent at low-q (i.e. slope in log-log plot) increases from 0 to 0.01, which could indicate a small increase in the size of the probed domains. Fits to the initial and week-3 profiles (figure 5.13) shows that the form factor of the aggregates changes from an ellipsoid with radii of 8 Å and 9.9 Å (polar and equatorial, respectively) to a more elongated ellipsoid with radii of 6.6 Å and 14.8 Å. The middle cartoon in Figure 5.12 depicts the increase in the size of the inverse micelle. Note that there is no indication of micellar aggregation in the case of Fe:DBSo. The Fe:AOT (figure 5.12 right) and Fe:DBSo (data not shown) salts dispersed in methanol did not show any change over the time period that they were tracked. This is to be expected since the metallic complex is fully dispersed in alcohol.

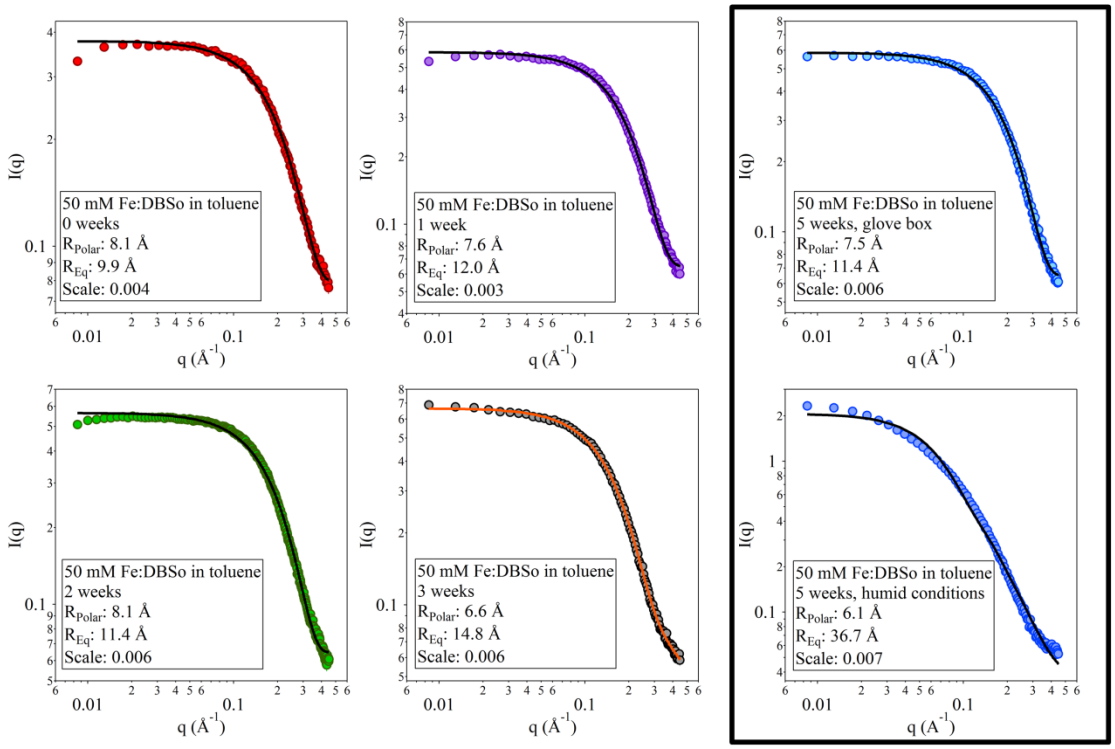

Figure 5.13: Fits performed to the aging DBSo in toluene SAXS profiles. A solid ellipsoid model is used. The scattering describe the core of the metal complex, and indicates swelling and growth of the micellar domains in the sample. The profiles inside the rectangle are obtained after 5 weeks under inert (top) and humid (bottom) conditions.

A mechanism that explains these changes is the slow hydration of the core of the microemulsion. Water has a finite solubility in toluene (~0.033 wt% at 25ºC), and the water can accumulate in the core hydrophilic core of the complex as time passes. As the concentration of water dissolved in the solvent decreases, more water from the atmosphere can dissolve into the solvent and further grow the structures by accumulating in their core. In order to evaluate this hypothesis, a dispersion of Fe:AOT and Fe:DBSo complexes is stored under humid conditions while a second vial of the same dispersion is stored in an environment with less than 2 ppm oxygen and humidity (glove box). The SAXS profiles are measured after 5 weeks of aging. The samples stored in the glove box

are the solid lines in figure 5.12. The low humidity and oxygen conditions significantly delays the growth of the microemulsions but does not fully stop changes in the structure. The small changes are probably caused by trace amounts of water that is dissolved in toluene and slowly migrates towards the polar core of the complexes. Since the metal surfactant complexes are also synthesized in water, it was found to be nearly impossible to effectively remove all trace amounts of water from these systems.

In contrast, intentional humid conditions (dashed lines in figure 5.12) enhanced the evolution of the micelles, accelerating and making more evident the structural changes in the metal complexes. This phenomena has been observed and reported in the literature for similar systems.[47-49] For Fe:AOT samples, a sharp increase in the scattering intensity at low-q indicates that the low-q plateau shifted to even lower-q and is no longer within the resolution of the SAXS instrument. Additionally, the shoulder from week 4 evolves into a very evident Guinier region that is located at a very similar q value to that of the fresh sample. As the micelle cluster keeps growing it is evident that the original micellar form factor is still present in the sample (the high-q Guinier region). For the Fe:DBSo sample that is kept in humid conditions, the elongation of the micelles increases to an almost cylinder-like structure with radii of 6.1 Å and 36.7 Å (polar and equatorial, respectively)(Figure 5.13).

Water Content.

The affinity of the organometallic salts to water is observed during the handling of these materials. The metal chlorides are hydrophiles and they are commonly found in a hydrate state[50]. It is also extremely hard to get rid of all the water trapped by the AOT

molecules[51, 52]. For these reasons, it was very important to see the effect that water has on the conformation and properties of the organometallic salts. Starting from the synthesis approach, it was obvious that AOT and DBSo salt retain more water than the DSa salts. DSa salts dried under vacuum overnight, while DBSo requires 2-3 days to fully dry and AOT salts will remain in a gel-like state even after several weeks under vacuum.

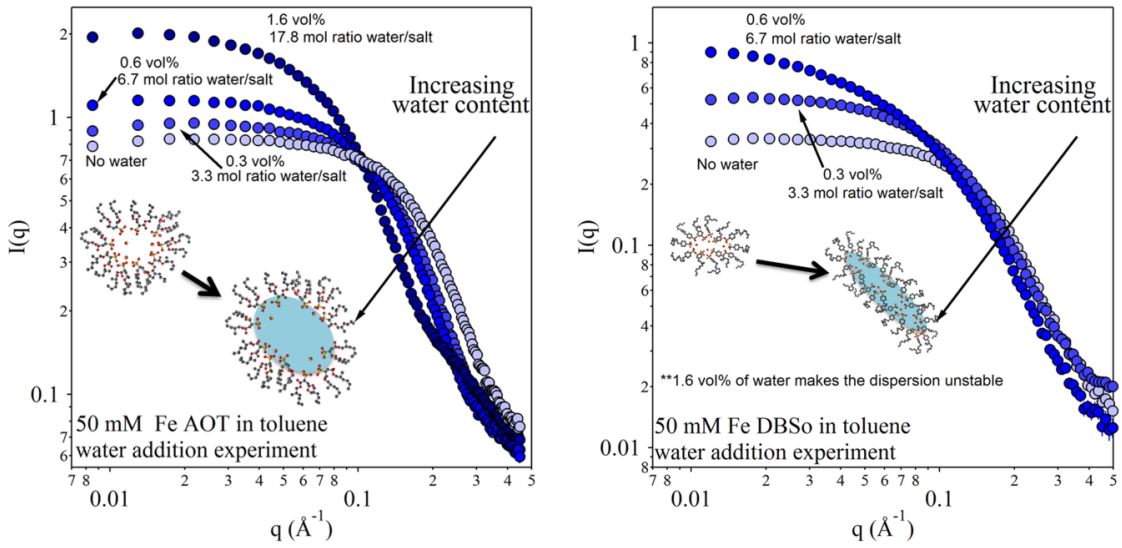

Figure 5.14: SAXS scattering profile of Fe:AOT (left) and Fe:DBSo (right) as water is added into the system. The insert figure depicts the possible growth mechanism analyzed by X-Ray scattering.

The effect of water in the structural conformation of the organometallic complexes dispersed in toluene is probed by adding water to the system. Water is added to the organometallic complex prior to the addition of the solvent in order to ensure the water-complex interaction is not hindered by the hydrophobicity of the solvent. The water concentrations used are 0.3, 0.6 and 1.6 volume percent. The Fe:AOT microemulsion swell with the addition of water, this phenomenon has been discussed previously.[9, 15, 26] It is important to point out that the evolution of the Fe:AOT with added water seems to differ from the aging Fe:AOT dispersion (figure 5.12). In figure 5.12 the

scattering evolution seems to indicate an aggregation of the micellar domains, whereas the changes in the conformation depicted in figure 5.14 show an increase in the size of the micelle but not indication of aggregation is present. The scattering of Fe:DBSo changes into a similar profile to the one observed under humid conditions (figure 5.12 and 5.13), which seems to indicate that the addition of water and aging in the sample causes the micelle to evolve in similar way.

Transport, Electrochemical, Optical and Electrostatic Properties of the Organometallic Complexes.

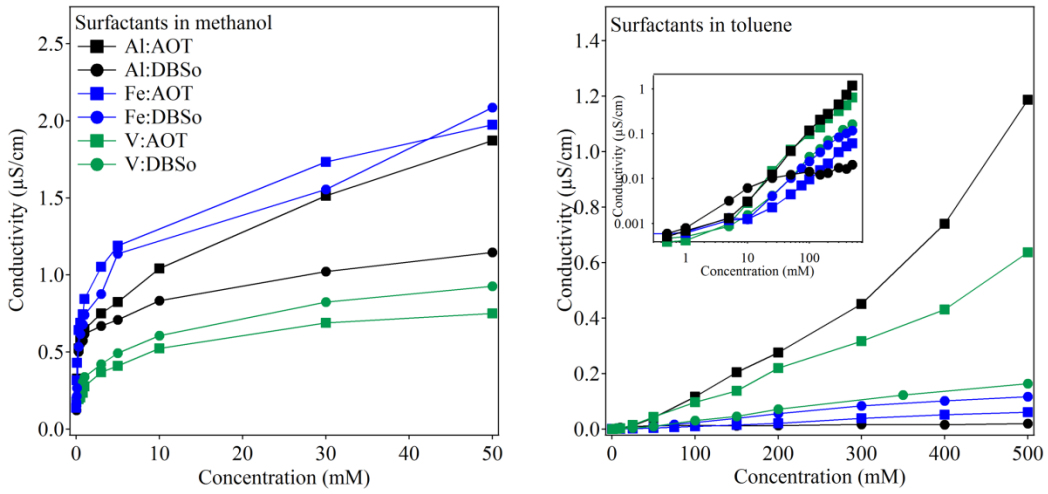

Figure 5.15: Conductivity, at different concentrations, of the metallic complexes dispersed in methanol (left) and toluene (right). Insert: Log-log plot of the conductivities in methanol.

Figure 5.15 shows the conductivity of different metallic complexes dispersed in methanol (left) and toluene (right) as a function of concentration. Al and Fe complexes show similar conductivities in methanol along the entire concentration series, whereas V samples show consistently lower conductivities. The similar conductivities among the salts corroborate the scattering results because SAS profiles show the complete

dissolution of the metal complex molecules in methanol. For similar complexes, this should lead to similar ion motilities and similar conductivities. The lower conductivity of the vanadium salt can be explained due to the larger drag and lower ionic mobility that arises from the fact that it has a larger number of associated organic molecules to each ion (5:1 instead of 3:1). A distinctive change in slope is observed around 1 mM for all the complexes.

The complexes dispersed in toluene increase the conductivity of the solvent by several orders of magnitude, and the relationship between conductivity and complex concentration is linear. AOT complexes are generally more conductive than DBSo, which is probably due to DBSo complexes being significantly larger than AOT complexes. The conductivity of Al:DBSo is drastically hindered at concentrations above 10 mM (insert in figure 5.15). The reason for this hindering is the formation of elongated complexes that cause the viscosity of the sample to increase drastically and also the decrease in the mobility of charge carriers.

The conductivities of the metal complex in toluene have a linear relationship with the concentration of the additive. This behavior is characteristic of ionic surfactants dispersed in apolar media.[53-55] Previous studies of Na:AOT showed very similar conductivities to the ones observed in this study and a similar linear dependence.[2, 53] The conductivity of the metal complexes in methanol deviates from the linear relationship with concentration. This is characteristic of a strong interaction between the ion pairs.[56] This corroborates the SAS analysis and the MD simulations, which indicate that there is no ion dissociation when the complex is dispersed in alcohols.

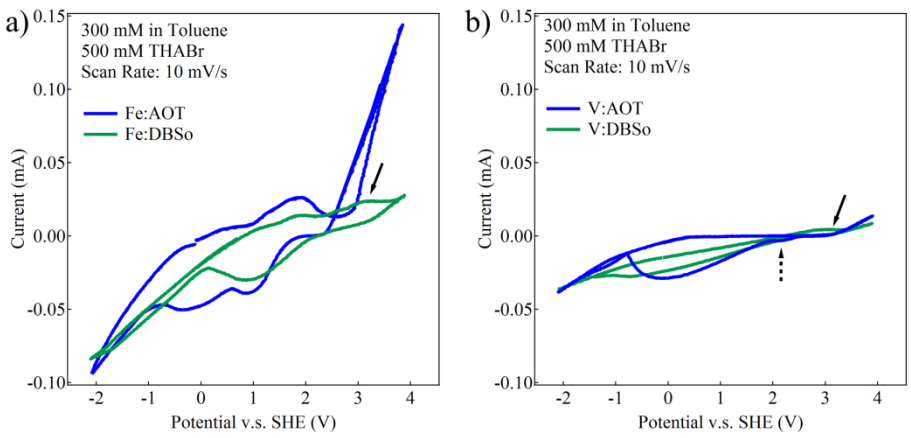

Figure 5.16: Cyclic voltammetry of Fe (a) and V (b) complexes dispersed in toluene. The solid arrows mark a common peak between the DBSo complexes. The dashed arrow highlights a small second reduction peak in the V:AOT curve.

Figure 5.16 shows the electrochemical behavior of the metallic complexes in toluene. The potentials in the figure are all referenced to the standard hydrogen electrode (SHE). Iron complexes are shown to be more redox active than their vanadium counterparts. Fe:DBSo (blue curve figure 5.16 a) and Fe:AOT (red curve in figure 5.16 a) curves show a reduction peak at around 1 V and an oxidation peak at around 1.7 V. This redox pair is possibly related to the $Fe^{3+} + e^{-} \leftrightarrow Fe^{2+}$. The Fe:AOT curve also shows a reduction peak at around -0.2 V, this potential could correspond to either $Fe^{3+} + 3e^{-} \leftrightarrow Fe(s)$ or $Fe^{2+} + 2e^{-} \leftrightarrow Fe(s)$ reactions. There is no apparent oxidation peak related to this reduction step. Peaks in the vanadium complexes are not as evident as in the iron system. There are a couple of peaks that can be observed in the V:AOT samples (red curve figure 5.16 b). The most evident reduction peak is very broad, centered at 0 V. A second, smaller reduction peak can be observed at 2.2 V (dashed arrow in figure 5.16 b), there are no evident oxidation peaks complementing these reduction peaks suggesting an irreversible transition. Fe:DBSo and V:DBSo show an oxidation peak at 3 V (arrows in

figure 5.16), which is not present in the AOT samples. Al salts did not show clean CV results since the redox potential for the reaction Al3+ + 3e- ↔ Al(s) is outside the stable potential window of toluene.

The cyclic voltammetry of the metallic salts show that the metallic ions associated with the surfactants can still be electrochemically active when dispersed in an apolar solvent. The metallic ions appear to be accessible to the electrodes despite being surrounded by insulating surfactant tails. These result shows that some metal complexes can be used for applications where an electrolyte for a redox system in apolar media is necessary. Additionally, figure 5.16 shows that iron salts are more electrochemically active than vanadium salts at these concentrations, and that metal ions paired with AOT performed better than the DBSo counterparts. The poor performance of vanadium can be related to the more efficient shielding of the metal ion by the larger number of surfactant molecules that are associated. Why complexes with AOT outperform those with DBSo is more difficult to explain. Possible mechanisms may be the higher water content in the AOT complexes or a more exposed ion center.

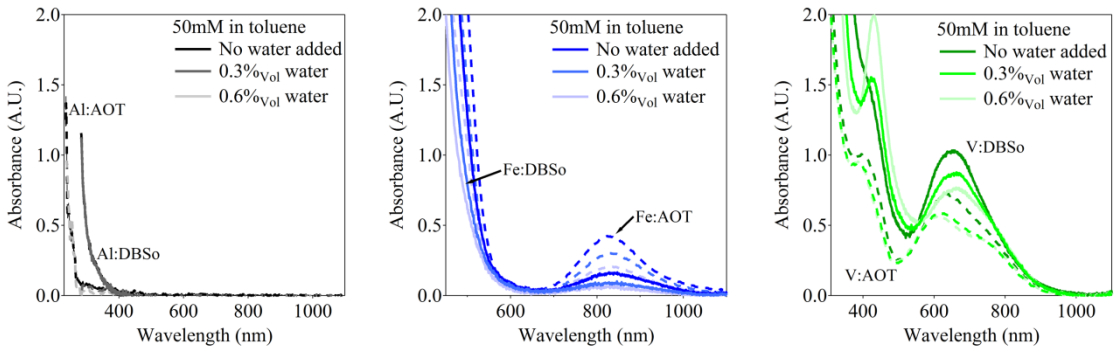

Figure 5.17: UV-vis absorbance of the metallic complex disperse in toluene with different levels of hydration.

Figure 5.17 shows the UV-visible absorbance of the metallic-surfactant complexes dispersed in toluene. AOT complex are depicted by dashed lines, while DBSo are solid lines. Aluminum complex show no absorbance in the wavelength range probed. Iron show a single peak at around 820 nm which intensity decreases as the water content is increased. Vanadium complexes spectra show two absorbance peaks at 400, 600 nm and a shoulder at ~700 nm. All these peaks decrease in intensity as the water is added. The peak at 400 is related to a V(V) oxidation state, while a peak at 600 is for V(III),and the shoulder at ~700 could be the presence of the peak characteristic of V(IV).[40] Ultimately this shows that after the formation of the vanadium complexes there are different redox states present in the sample.

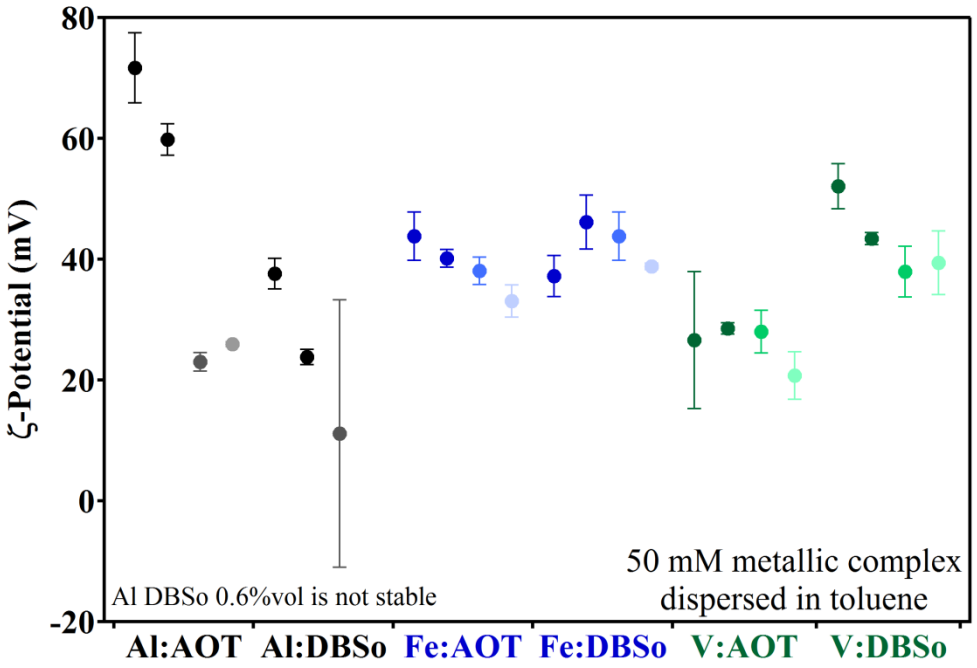

Figure 5.18: ζ potential of the metallic complex disperse in toluene with different levels of hydration.

The ζ potential of the metallic complex dispersed in toluene are measured and the results are displayed in figure 18. Although the definition of the meaning of the ζ potential is complex in solvents with low dielectric constant such as toluene, this measurement can be related to the electrophoretic mobility of the system. The results shows that all dispersion are formed by positively-charged micelles. The positive charge of the micelles is almost not affected by the hydration of the system, since the ζ potential stays basically constant.

Conclusions

The present work describes the synthesis of a metal-surfactant complex. The sodium of the surfactants dodecylbenzene sulfonate, dioctyl sulfosuccinate and dodecyl sulfate is replaced by multivalent ions of iron and aluminum and vanadium. These multivalent metal-surfactant complexes have been previously reported for AOT systems.[16-26] This work shows that surfactants (e.g. DBSo) that normally do not disperse in low-dielectric solvents, can form self-assembled complexes when the monovalent counter ion is exchange for a multivalent one. AOT and DBSo metallic complexes readily dispersed in a wide variety of organic complexes, while DSa complexes are only soluble in alcohols. AOT and DBSo complexes form large macromolecular aggregates in organic solvents. The shape and size of these structures in toluene is carefully evaluated using simultaneous analysis of small angle neutron and x-ray scattering. Additionally, MD simulations of the complexes are performed to corroborate the structures inferred from SAS. The behavior of the complexes in methanol is also probed using small angle scattering and MD simulations. The results indicate that the hydroxyl group of the solvent strongly interacts with the metal ion resulting in a more dispersed system. The results of

SAS and MD simulations generally show good agreement between shape and size of the self-assembled structures.

The conductivity and electrochemical behavior of the complexes is also analyzed. The conductivity corroborates the presence of macromolecular structures in toluene and significantly smaller structures in alcohols that are also consistent with the structural analyses. Some complexes also showed to be electrochemically active even when dispersed in solvent with a very low dielectric constant. This could present several advantages for designing new electrochemical systems that rely on organic solvents. One possible application is in the design of organic-solvent flow batteries with half-cells that produce larger voltage differences than are possible in water-based electrolytes.[57, 58]

References

1. Elschner, A.; Kirchmeyer, S.; Lovenich, W.; Merker, U.; Reuter, K., *PEDOT: Principles and Application of an Intrinsically Conductive Polymer*. CRC Press: Boca Raton, Fl, 2011.
2. Dukhin, A.; Parlia, S., Ions, ion pairs and inverse micelles in non-polar media. *Current Opinion in Colloid & Interface Science* 2012, 18, (2), 93-115.
3. Beunis, F.; Strubbe, F.; Karvar, M.; Drobchak, O.; Brans, T.; Neyts, K., Inverse micelles as charge carriers in nonpolar liquids: Characterization with current measurements. *Current Opinion in Colloid & Interface Science* 2013, 18, (2), 129-136.
4. Mathews, M. B.; Hirschhorn, E., Solubilization and Micelle Formation in a Hydrocarbon Medium. *Journal of Colloid Science* 1953, 8, (1), 86-96.
5. Berg, J. C., *An Introduction to Interfaces and Colloids: The Bridge to Nanoscience*. World Scientific Publishing Co. Pte. Ltd.: Singapore, 2010.
6. Piper, J. D.; Fleiger, A. G.; Smith, C. C.; Kerstein, N. A., Electrical insulating materials - Liquid dielectrics - Chemical, physical, electrical properties of systems containing lead or copper soaps in liquid paraffin. *Industrial and Engineering Chemistry* 1939, 31, 307-317.
7. Lyklema, J., Principles of interactions in non-aqueous electrolyte solutions. *Current Opinion in Colloid & Interface Science* 2013, 18, (2), 116-128.
8. Dukhin, A.; Parlia, S., Ions, ion pairs and inverse micelles in non-polar media. *Current Opinion in Colloid & Interface Science* 2015, 18, (2), 93-115.
9. Morrison, I. D., Electrical Charges in Nonaqueous Media. *Colloids and Surfaces a-Physicochemical and Engineering Aspects* 1993, 71, (1), 1-37.

10. Capek, I., The inverse mini-emulsion polymerization of acrylamide. *Designed Monomers and Polymers* 2003, 6, (4), 399-409.
11. Gacek, M.; Bergsman, D.; Michor, E.; Berg, J. C., Effects of Trace Water on Charging of Silica Particles Dispersed in a Nonpolar Medium. *Langmuir* 2012, 28, (31), 11633-11638.
12. Kriwet, B.; Walter, E.; Kissel, T., Synthesis of bioadhesive poly(acrylic acid) nano- and microparticles using an inverse emulsion polymerization method for the entrapment of hydrophilic drug candidates. *Journal of Controlled Release* 1998, 56, (1-3), 149-158.
13. Opawale, F. O.; Burgess, D. J., Influence of interfacial properties of lipophilic surfactants on water-in-oil emulsion stability. *Journal of Colloid and Interface Science* 1998, 197, (1), 142-150.
14. Eicke, H. F.; Christen, H., On the Stability of Micelles in Apolar Media. *Journal of Colloid and Interface Science* 1973, 46, (3), 417-427.
15. Eastoe, J.; Fragneto, G.; Robinson, B. H.; Towey, T. F.; Heenan, R. K.; Leng, F. J., Variation of Surfactant Counterion and its Effect on the Structure and Properties of Aerosol-OT-Based Water-in-Oil Microemulsions. *Journal of the Chemical Society-Faraday Transactions* 1992, 88, (3), 461-471.
16. Brown, P.; Butts, C. P.; Eastoe, J.; Glatzel, S.; Grillo, I.; Hall, S. H.; Rogers, S.; Trickett, K., Microemulsions as tunable nanomagnets. *Soft Matter* 2012, 8, (46), 11609-11612.
17. Burrows, H. D.; Tapia, M. J., Lanthanide ion binding in AOT/water/isooctane microemulsions. *Langmuir* 2002, 18, (17), 6706-6708.
18. Caboi, F.; Capuzzi, G.; Baglioni, P.; Monduzzi, M., Microstructure of Ca-AOT/water/decane w/o microemulsions. *Journal of Physical Chemistry B* 1997, 101, (49), 10205-10212.
19. Dunn, C. M.; Robinson, B. H.; Leng, F. J., Photon-Correlation Spectroscopy Applied to the Size Characterization of Water-in-Oil Microemulsion Systems Stabilized by Aerosol-OT Effect of Change in Counterion. *Spectrochimica Acta Part a-Molecular and Biomolecular Spectroscopy* 1990, 46, (6), 1017-1025.
20. Eastoe, J.; Fragneto, G.; Steytler, D. C.; Robinson, B. H.; Heenan, R. K., Small-Angle Neutron Scattering From Novel Bis-2-Ethylenesulphosuccinate Microemulsion - Evidence for Nonspherical Structures. *Physica B* 1992, 180, 555-557.
21. Eastoe, J.; Steytler, D. C.; Robinson, B. H.; Heenan, R. K.; Norht, A. N.; Dore, J. C., Structure of Cobalt Aerosl-OT Reversed Micelles Studied by Small-Angle Scattering Methods. *Journal of the Chemical Society-Faraday Transactions* 1994, 90, (17), 2497-2504.
22. Haynes, J. S.; Sams, J. R.; Thompson, R. C., Sythesis and Structural Studies of Iron(II) and Iron(III) Sulfonates. *Canadian Journal of Chemistry-Revue Canadienne De Chimie* 1981, 59, (4), 669-678.
23. Longo, A.; Ruggirello, A.; Liveri, V. T., Physicochemical investigation of nanostructures in liquid phases: Ytterbium nitrate ionic clusters confined in ytterbium bis(2-ethylhexyl) sulfosuccinate reversed micelles and liquid crystals. *Chemistry of Materials* 2007, 19, (5), 1127-1133.

24. Marques, M. F. F.; Burrows, H. D.; Miguel, M. D.; deLima, A. P.; Gil, C. L.; Duplatre, G., Analysis and modelling of positron lifetime spectroscopy data for the characterisation of water-in-oil microemulsion systems stabilised by Aerosol OT - Effect of changing the counter-ion. *Journal of the Chemical Society-Faraday Transactions* 1997, 93, (21), 3827-3831.
25. Towey, T. F.; Baglioni, P.; Martini, G.; Ristori, S., ESR Spectroscopy of Metal Bis(2-Ethylhexyl) Sulfoccinate Aggregates in Cyclohexane *Journal of Physical Chemistry* 1995, 99, (12), 3939-3942.
26. Eastoe, J.; Towey, T. F.; Robinson, B. H.; Williams, J.; Heenan, R. K., Structures of Metal Bis(2-Ethylhexyl) Sulfosuccinate Aggregates in Cyclohexane. *Journal of Physical Chemistry* 1993, 97, (7), 1459-1463.
27. de Oliveira, R. J.; Brown, P.; Correia, G. B.; Rogers, S. E.; Heenan, R.; Grillo, I.; Galembeck, A.; Eastoe, J., Photoreactive Surfactants: A Facile and Clean Route to Oxide and Metal Nanoparticles in Reverse Micelles. *Langmuir* 2011, 27, (15), 9277-9284.
28. Eastoe, J.; Stebbing, S.; Dalton, J.; Heenan, R. K., Preparation of colloidal cobalt using reversed micelles. *Colloids and Surfaces a-Physicochemical and Engineering Aspects* 1996, 119, (2-3), 123-131.
29. Rees, G. D.; Evans-Gowing, R.; Hammond, S. J.; Robinson, B. H., Formation and morphology of calcium sulfate nanoparticles and nanowires in water-in-oil microemulsions. *Langmuir* 1999, 15, (6), 1993-2002.
30. Rao, C. R. K.; Muthukannan, R.; Jebin, J. A.; Raj, T. A.; Vijayan, M., Synthesis and properties of polypyrrole obtained from a new Fe(III) complex as oxidizing agent. *Indian Journal of Chemistry Section a-Inorganic Bio-Inorganic Physical Theoretical & Analytical Chemistry* 2013, 52, (6), 744-748.
31. Brown, P.; Butts, C. P.; Cheng, J.; Eastoe, J.; Russell, C. A.; Smith, G. N., Magnetic emulsions with responsive surfactants. *Soft Matter* 2012, 8, (29), 7545-7546.
32. Brown, P.; Khan, A. M.; Armstrong, J. P. K.; Perriman, A. W.; Butts, C. P.; Eastoe, J., Magnetizing DNA and Proteins Using Responsive Surfactants. *Advanced Materials* 2012, 24, (46), 6244-6247.
33. Capuzzi, G.; Baglioni, P.; Gambi, C. M. C.; Sheu, E. Y., Percolation phenomenon of calcium bis(2-ethylhexyl) sulfosuccinate water-in-oil microemulsions by conductivity and dielectric spectroscopy measurements. *Physical Review E* 1999, 60, (1), 792-798.
34. Connelly, N. G.; Geiger, W. E., Chemical redox agents for organometallic chemistry. *Chemical Reviews* 1996, 96, (2), 877-910.
35. Glinka, C. J.; Barker, J. G.; Hammouda, B.; Krueger, S.; Moyer, J. J.; Orts, W. J., The 30 m small-angle neutron scattering instruments at the National Institute of Standards and Technology. *Journal of Applied Crystallography* 1998, 31, 430-445.
36. Kline, S. R., Reduction and analysis of SANS and USANS data using IGOR Pro. *Journal of Applied Crystallography* 2006, 39, 895-900.
37. Martinez, L.; Andrade, R.; Birgin, E. G.; Martinez, J. M., PACKMOL: A Package for Building Initial Configurations for Molecular Dynamics Simulations. *Journal of Computational Chemistry* 2009, 30, (13), 2157-2164.

38. Wang J; Wolf RM; Caldwell JW; Kollman PA; DA., C., Development and Testing of a General Amber Forced Field. *Journal of Computational Chemistry* 2005, 25, (9), 1157-1174.
39. Guardia E; JA, P., Molecular Dyanmics Simulation of Ferrous and Ferric Ions in Water. *Chemical Physics* 1990, 144, (3), 353-362.
40. Choi, N. H.; Kwon, S.-K.; Kim, H., Analysis of the Oxidation of the V(II) by Dissolved Oxygen Using UV-Visible Spectrophotometry in a Vanadium Redox Flow Battery. *Journal of the Electrochemical Society* 2013, 160, (6), A973-A979.
41. Berr, S. S., Solvent Isotope Effects on Alkyltrimethylammonium Bromide Micelles as a Function of Alkyl Chain-Lenght. *Journal of Physical Chemistry* 1987, 91, (18), 4760-4765.
42. Livsey, I., Neutron Scattering from Concentry Ciylinders - Interparticle Interference Function and Radius of Gyration *Journal of the Chemical Society-Faraday Transactions Ii* 1987, 83, 1445-1452.
43. Kotlarchyk, M.; Chen, S. H., Analysis of Small-Angle Neutron Scattering Spectra from Polydisperse Interacting Colloids. *Journal of Chemical Physics* 1983, 79, (5), 2461-2469.
44. Kumar, S.; Sharma, D.; Kabir ud, D., Small-angle neutron scattering studies on sodium dodecylbenzenesulfonate-tetra-n-butylammonium bromide systems. *Journal of Surfactants and Detergents* 2006, 9, (1), 77-82.
45. Kotlarchyk, M.; Huang, J. S.; Chen, S. H., Structure of AOT-Reversed Micelles Determined by Small-Angle Neutron Scattering. *Journal of Physical Chemistry* 1985, 89, (20), 4382-4386.
46. Larson-Smith, K.; Pozzo, D. C., Scalable synthesis of self-assembling nanoparticle clusters based on controlled steric interactions. *Soft Matter* 2011, 7, (11), 5339-5347.
47. Bergenholtz, J.; Romagnoli, A. A.; Wagner, N. J., viscosity, microstructure, and interparticle potential of aot/h2o/n-decane inverse microemulsions. *Langmuir* 1995, 11, (5), 1559-1570.
48. Shrestha, L. K.; Glatter, O.; Aramaki, K., Structure of Nonionic Surfactant (Glycerol alpha-Monomyristate) Micelles in Organic Solvents: A SAXS Study. *Journal of Physical Chemistry B* 2009, 113, (18), 6290-6298.
49. Tabor, R. F.; Eastoe, J.; Dowding, P. J.; Grillo, I.; Rogers, S. E., Bidisperse colloids: Nanoparticles and microemulsions in coexistence. *Journal of Colloid and Interface Science* 2010, 344, (2), 447-450.
50. Remsungnen, T.; Rode, B. M., QM/MM molecular dynamics simulation of the structure of hydrated Fe(II) and Fe(III) ions. *Journal of Physical Chemistry A* 2003, 107, (13), 2324-2328.
51. Hauser, H.; Haering, G.; Pande, A.; Luisi, P. L., interaction of water with sodium bis(2-ethyl-1-hexyl) sulfosuccinate in reversed micelles. *Journal of Physical Chemistry* 1989, 93, (23), 7869-7876.
52. Eicke, H. F.; Christen, H., is water critical to formation of micelles in apolar media. *Helvetica Chimica Acta* 1978, 61, (6), 2258-2263.

53. Denat, A.; Gosse, B.; Gosse, J. P., Electrical Conductivity of Solutions of an Ionic Sufactant in Hydrocarbons. *Revue De Physique Appliquee* 1981, 16, (12), 673-678.
54. Kim, J.; Anderson, J. L.; Garoff, S.; Schlangen, L. J. M., Ionic conduction and electrode polarization in a doped nonpolar liquid. *Langmuir* 2005, 21, (19), 8620-8629.
55. Poovarodom, S.; Berg, J. C., Effect of particle and surfactant acid-base properties on charging of colloids in apolar media. *Journal of Colloid and Interface Science* 346, (2), 370-377.
56. Dukhin, A., Critical concentration of ion-pairs formation in nonpolar media. *Electrophoresis* 2014, 35, (12-13), 1773-1781.
57. Shinkle, A. A.; Pomaville, T. J.; Sleightholme, A. E. S.; Thompson, L. T.; Monroe, C. W., Solvents and supporting electrolytes for vanadium acetylacetonate flow batteries. *Journal of Power Sources* 2014, 248, 1299-1305.
58. Zhang, D.; Lan, H.; Li, Y., The application of a non-aqueous bis(acetylacetone)ethylenediamine cobalt electrolyte in redox flow battery. *Journal of Power Sources* 2012, 217, 199-203.

Chapter VI

Synthesis and Characterization of Organic Solvent Dispersible Poly(3,4-Ethylenedioxythiophene)-Surfactant Complex

Poly(3,4-ethylenedioxythiophene) (PEDOT) has been arguably the most commercially successful intrinsically conductive polymer (ICP) to date because of its relatively high transparency and high conductivity[1]. The conductivity of doped PEDOT is in the range of 500-1200 S/cm making it one of the highest among ICPs[2]. PEDOT also has a low optical absorbance in the visible spectrum and is a robust material in terms of environmental degradation[1].

Unfortunately the same feature that gives the polymer its high conductivity also makes it very difficult to process from solution. Due to the rigidity of the PEDOT backbone, it is virtually impossible to disperse in pure form in any solvent[1]. In order to make the polymer processable, PEDOT is currently paired with compounds that simultaneously neutralize the positive charges of the polymer and also help to stabilize it in aqueous dispersions[3]. The charge balancing molecule bound to the PEDOT chains is often referred to as a 'dopant', even when this counter-ion does not necessarily oxidize the polymer chain[2].

By far, the most common form of the PEDOT polymer is when it is paired with polystyrene sulfonate (PSS)[1, 4]. PSS interacts with PEDOT through its exposed negatively charged sulfonate groups. The excess charge of the PSS also helps to stabilize the polymer due to repulsive electrostatic interactions between PEDOT:PSS chains in polar solvents like water. PEDOT:PSS is used commercially to generate thin films for organic photovoltaics and in organic light emitting diodes as the hole injection layer[5, 6]. It is also used in the fabrication of high-voltage capacitors and in anti-static applications (e.g. photographic films)[7, 8]. Yet, processing of PEDOT:PSS is limited to aqueous dispersions and small deviations from this, by the addition of miscible solvents (e.g. alcohols), will make the dispersion unstable and unusable[1]. This work explores a novel way to synthesize PEDOT complexes directly in organic solvents of low or no polarity. This synthesis route also results in simultaneous polymer doping with a surfactant during EDOT polymerization. The surfactant's organic tail renders the polymer dispersible in organic solvents by increasing configurational entropy in the dispersion state and by increasing stability due to steric repulsion.

A similar route for the polymerization of polypyrrole in the presence of surfactants has been previously reported[9-11]. These studies succeeded in creating stable and highly conductive polypyrrole dispersions in organic solvents by using sodium dodecyl sulfate (SDS) and dodecylbenzene sulfonic acid (DBSA). Here, we apply this synthesis route to other polymers (i.e. PEDOT) and perform a comprehensive study of the effect of the solvent, surfactant type and polymerization conditions on the structure of the polymer dispersion and its properties.

A few other accounts of PEDOT dispersions in organic solvents can also be found in the literature. In general, ICPs are rendered processable by covalently attaching an alkyl chain to the monomers. This method has also been demonstrated by attaching functional units to the ethylenedioxy bridge in the EDOT monomer prior to polymerization[12-14]. The presence of these functional units can end up hindering the polymerization due to strong electronic and steric interactions. Another approach is through in-situ chemical polymerization[15]. In this method, a mixture of EDOT monomer and an oxidizer are mixed in an organic solvent. The mixture is then cast into films and the reaction proceeds until the solvent evaporates. The oxidizer is washed out of the film and only PEDOT remains. A drawback of this technique is that the quality of the resulting polymer is very dependent on the conditions under which the film is cast, the time between mixing and casting the film, and the solvent evaporation time [1]. Another approach, used by Heraeus Precious Metals, is the pairing of PEDOT with at polysulfonic acid copolymer[16]. This process is analogous to the use of PSS for aqueous dispersions. The drawback for this approach is the high content of non-conductive high molecular weight polymer that, when compared to small surfactant molecules, leads to lower conductivities.[16]

This work describes a method to synthesize PEDOT dispersible in organic solvent. The method is low-cost, and allows the use of PEDOT in techniques and processes where the need for organic dispersions previously prevented it.

Materials and Methods.

Synthesis of Organic-dispersible PEDOT Complexes.

Specially synthesized organic iron III salts are used to synthesize poly(ethylene dioxythiophene) (PEDOT). Iron salts are synthesized by dispersing the surfactant in water, then adding an excess of iron(III) chloride. When the iron(III) and the surfactant interact with each other, the complex becomes insoluble in water and crashes out. The iron-surfactant salt is filtered and dried under vacuum for at least three days. The organic dried iron III salts are dissolved in a solvent that can be toluene, methanol, isopropyl alcohol or chloroform (Sigma-Aldrich, St Louis, MO). Ethylene dioxythiophene monomer (EDOT) (Sigma-Aldrich, St Louis, MO) is added to the iron salt dispersion at a molar ratio of 1:1 relative to iron. In order to identify the parameters that affect the conformation of the PEDOT, different synthesis conditions are tested. The temperature of reaction, the solvent in which the synthesis takes placed and the starting monomer concentration are the three parameters varied. Table 6.1 shows the synthesis conditions of each of the different synthesis batches used. Notice that the quantity of iron salt added to the sample varies in order to keep the 1:1 molar ration relative to initial monomer concentration. The samples are thoroughly mixed and are let to react undisturbed for two weeks before the excess iron salt is purified out by using ultrafiltration (Millipore, Billerica, MA), using solvent-resistant, 1μm pore size filters (Pall Port Washington, NY). This removes excess surfactant and iron ions from the dispersion since they are in excess over the PEDOT. The filtrate is tracked using a UV-Vis spectrophotometer until the characteristic absorbance peak for iron ions at a wavelength of ~300 nm disappears. It

typically takes 10-12 solvent exchanges for the concentration of iron to be insignificant enough to not be observed in the UV-Vis spectra. The polymer is then scraped out of the ultrafiltration chamber and dried overnight.

Table 6.1: Synthesis conditions for the different PEDOT samples. Table also shows the quantity of PEDOT obtained at each condition.

	Monomer Concentration			Solvent			Temperature		
Iron Complex	AOT	AOT	AOT	DBSo	DBSo	DBSo	DBSo	DBSo	DBSo
Solvent	Chloroform	Chloroform	Chloroform	Toluene	Chloroform	IPA	Toluene	Toluene	Toluene
EDOT Conc. (mg/ml)	5	15	50	30	30	30	30	30	30
EDOT Quantity (mg)	35	104	350	210	210	210	210	210	210
Iron Salt Quantity (g)	0.333	0.976	3.89	1.54	1.55	1.55	1.52	1.55	1.54
Temperature (ºC)	60	60	60	60	60	60	Room T.	40	60
Solvent Volume (ml)	7	7	7	7	7	7	7	7	7
Product (mg)	43	460	276	532	356	49	480	516	532
Product wt/EDOT wt	1.2	4.42	0.79	2.53	1.70	0.23	2.29	2.46	2.53

Electron Microscopy.

A FEI (Hillsboro, OR) Tecnai G2 F20 transmission electron microscope (TEM) is used for scanning transmission electron microscopy (sTEM) operating at 200kV. A 5 mg/ml dispersion of the polymer in chloroform is created by ultrasonication of the polymer in the solvent for 3 minutes with a 20% amplitude using a Branson Ultrasonics horn (Danbury, CT). A drop of the stable dispersion is then deposited on an ultrathin, TEM copper grid with Formvar support (Ted Pella, Redding, CA), and allowed to dry.

SEM is performed in an FEI Sirion SEM with an accelerating voltage of 5kV. Samples are prepared by drop casting 3 ml of a 5 mg/ml polymer dispersion on top of a glass slide. In order to render to sample conductive, 7 nm of gold is sputter coated over the sample.

Dielectric Spectroscopy.

AC dielectric spectroscopy measurements are performed using an Agilent e4980a LCR Meter. A perturbation voltage of 20 mV, within the linear impedance response range, and a frequency range of 20 Hz – 2 MHz are used for all samples. The dielectric spectroscopy and DC conductivity of dried PEDOT is measured by compressing a pellet of the polymer powder. The solid dimensions are 3.81 mm in diameter and 0.3 mm thick.

Small Angle Neutron Scattering.

Small angle neutron scattering (SANS) and ultra small angle neutron scattering (USANS) experiments are performed at the Center for Neutron Research at the National Institute of Standards and Technology (NIST) in Gaithersburg, Maryland. The neutron scattering experiments are performed using both the NGB-30 (SANS) and BT5 (USANS) instruments. SANS is performed using a standard configuration to cover a wide range of wave-vector values ($0.002 < q < 0.3$ Å^{-1})[17], using wavelengths of 6, and 8.4 Å. USANS experiments are performed using the perfect crystal diffractometer BT5 at the NIST-NCNR[18]. This increases the total q range to $3x10^{-5}$ Å^{-1} making possible to characterize the micrometer size features of the polymer particles. For each measurement, the samples are taken directly from the SANS instrument and placed into BT5 so that identical and fully equilibrated structures are probed.

The samples are formed by dispersing the polymer in d-chloroform (Sigma-Aldrich) and ultrasonicating with a probe for at least three minutes using amplitudes between 20 and 30%. The polymer is added to the solvent at different concentrations in order to corroborate that there are no interparticle correlations (i.e. structure factors) that

emerge at high concentrations. Ultimately a concentration of 15 mg/ml is used for all samples unless otherwise specified. Additionally, dispersions of PEDOT are prepared with variable ratios of hydrogenated and deuterated toluene in order to measure the scattering length density (SLD) of the synthesized polymer.

All samples are exposed to the neutron beam using demountable Ti cells with quartz windows and a 1 mm path length. The data is reduced and corrected by accounting for background radiation and scattering from the empty cell. The data is also normalized to an absolute scale by measuring the incident neutron flux[19]. Data reduction is performed using the standard NIST Igor-based macros[19]. Analysis and model fitting is also performed using the NIST Igor-based analysis software and the DANSE SansView software[19]. The models, when fit to the data, are corrected to account for the different collimation systems (i.e. smearing) with the tools available in these software packages. Corrections for incoherent scattering are also performed by assuming that, at the largest measurable scattering vectors ($q > 2$ Å^{-1}), the scattering intensity is dominated by a flat incoherent background signal.

Small Angle X-ray Scattering.

A small angle X-ray Scattering (SAXS) instrument (Anton-Paar, Graz, Austria) with a line-collimation system using a Cu Kα source with a wavelength of 1.54 Å is used. Fujifilm (Greenwood, SC) image plates and a Perkin-Elmer (Covina, CA) image plate reader are employed to acquire the data. The SAXSQuant software is used to reduce the two dimensional data to a one-dimensional, intensity (I) versus scattering vector (q) plot. PEDOT in powder form is placed in between two pieces of thin glass (75 μm) by using

an aluminum spacer 0.016" thick. The powder is exposed to the x-ray beam at 20ºC for 2 hrs.

UV-Visible Spectroscopy and Dynamic Light Scattering.

UV-visible spectroscopy is performed in 2.5 mg/ml PEDOT dispersions in chloroform. The samples are prepared using the same protocol as the SANS dispersions. A Thermo Scientific Evolution 300 (Fremont, CA) spectrophotometer is used, covering wavelengths from 200 to 1100 nm. The samples are placed in a 1 mm path length quartz cuvette. The absorbance of chloroform is subtracted from the sample signal and treated as background.

Dynamic light scattering is performed in a Malvern Zetasizer Nano ZS instrument (Worcestershire, United Kingodm), the measurement is made using a laser wavelength of 633 nm. The same samples used for the UV-vis experiments are used in this case. The measurements are run in a 1 cm path length glass cuvette.

Stabilization of PEDOT Dispersion.

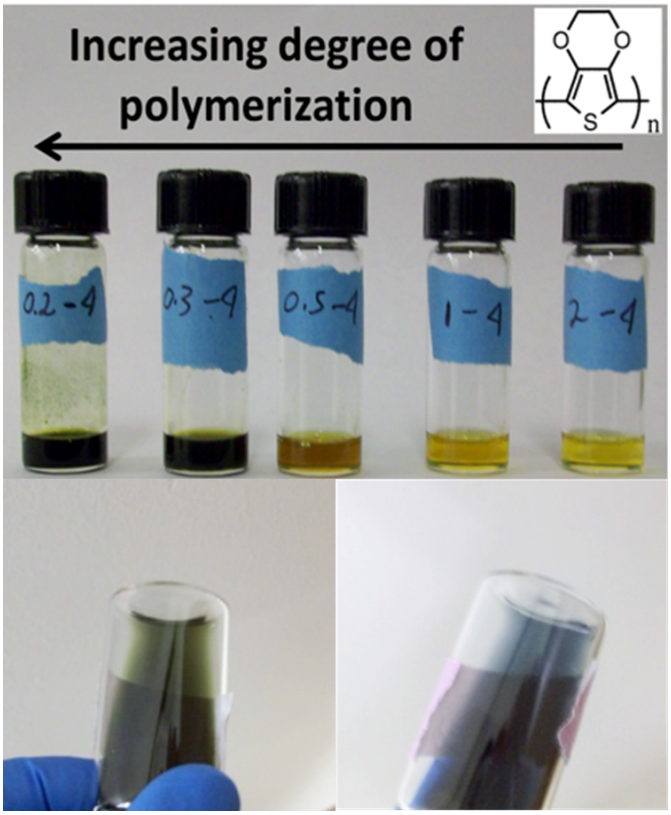

Figure 6.1: Top: Pictures of the evolution on the appearance of the dispersion as the reaction takes place. Bottom: left, Detail of the green color caused by the presence of PEDOT in the salt dispersion. Right, blue hue of the PEDOT complex after purification.

Figure 6.1 shows pictures of PEDOT dispersions at different stages of the polymerization. From right to left on figure 6.1 (top), the sample initially has transparent yellow hue, which is the color of the iron salt dispersed in the solvent. As the polymerization of the EDOT monomer (insert figure 6.1) proceeds, the solution turns dark. Eventually the solution will turn completely opaque and/or small pieces of aggregates will start to be visible. Upon close examination it is clear that the opaque solution has a green hue (figure 6.1 bottom left). This green coloration arises from the

combination of the yellow color of the iron salt, mixed with the characteristic blue color of PEDOT. The presence of aggregates is usually caused by an incompatible pairing of the dopant and the solvent or by a high concentration of the resulting polymer in the sample. The iron salt in the sample is filtered out as previously described until all of the excess monomer and salt is removed. The remaining powder can be dispersed in several non-polar organic solvents including chloroform and toluene. The purified dispersion has the characteristic blue color of PEDOT dispersions (figure 6.1 bottom right).

The reaction time varies widely depending on the solvent in which the EDOT and the iron salt are initially dissolved for polymerization. Synthesis in toluene will regularly form a gel 1-2 days after the reaction is started. Synthesis in chloroform proceeds well but will not form gels even after two weeks. It is worth noting that the formation of gels under some synthesis conditions is not a detrimental feature. On the contrary, gelation facilitates the purification of the sample. After the sample is purified and dried, the polymer will disperse in many solvents using the previously described steps. Alcohols (e.g. methanol, ethanol and IPA) slow the reaction kinetics significantly and after two weeks at room temperature no PEDOT can be recovered by purification even though a change in color is observed. This could be due to a low solubility of EDOT in the alcohol due to the high polarity of the solvent[20]. In chloroform and toluene EDOT disperses readily, resulting in faster reaction kinetics in those solvents. In order to obtain significant amounts of PEDOT synthesized in alcohols it is necessary to slightly increase the synthesis temperature to 60 °C. At elevated temperatures the kinetics of the synthesis accelerates. Even at just 40 ºC the samples will turn opaque within a day.

Calculating the yields percentage of the reaction is not trivial. The dopant adds a significant amount of mass to the polymer, but the dope level is not evident therefore an actual percent yield cannot be easily calculated. In order to quantify the efficiency of the synthesis conditions, the weight ratio (R) of the product, after purification and drying, to the weight of the EDOT monomer added is quantified (table 6.1). When compared the yield obtained from the synthesis with different solvents toluene produces the biggest yield with and R of 2.53, versus chloroform with 1.7. Isopropyl alcohol is by far the most inefficient solvent with and R of only 0.23. When compared the synthesis at different temperature there is a jump in the yield from room temperature (~25 ºC) to 40 ºC when R goes from 2.30 to 2. 46, at 60 ºC the R=2.53. This shows that solvent choice has a much bigger effect than temperature in the yield. The samples with varying monomer concentration do not show any clear trends in the yield; this high variability could be caused by the surfactant choice (monomer concentration series is done using AOT instead of DBSo as in the other series), due to the higher solubility of AOT in the solvent used for sample purification, which makes AOT vulnerable to be washed away.

As previously discussed, the rigidity of pure PEDOT causes an uncontrollable aggregation of polymer, rendering the polymer hard to disperse in any solvent. If a surfactant is attached to the polymer head-on due to doping, improved wetting and steric interactions of the tails can stabilize PEDOT dispersions. Still, the choice of organic chain is important in order to achieve stable dispersions. If the dopant chain is too short or incompatible with the solvent, the PEDOT will not be stable and will readily aggregate. If the dopant is adequate, PEDOT particles will remain dispersed in the

organic solvent rendering the polymer processable and capable of forming homogenous films.

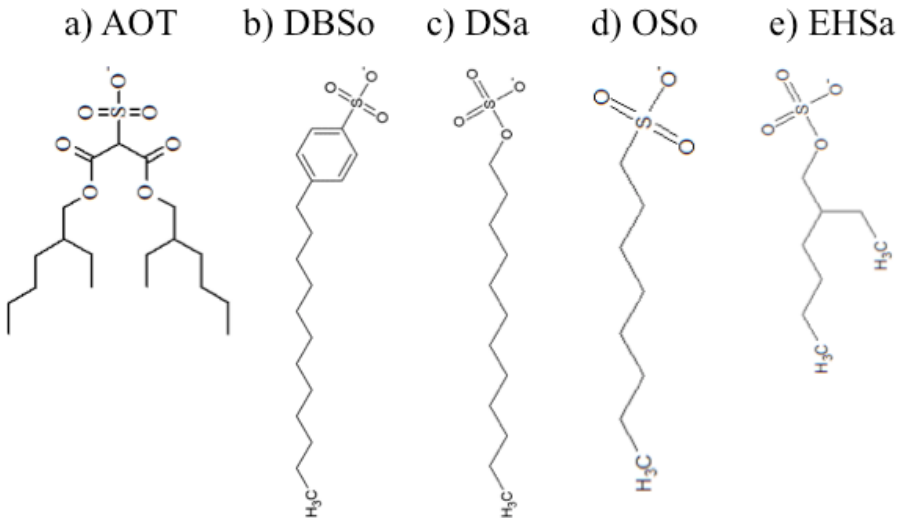

Figure 6.2 shows the chemical structure of some of the surfactants used as dopants and stabilizers. a) dioctyl sulfosuccinate (AOT), b) dodecyl benzene sulfonate (DBSo), c) dodecyl sulfate (DSa), d) octyl sulfonate (Oso), e) ethyl hexyl sulfate (EHSa).

Table 6.2: State of the polymerization of PEDOT doped with the surfactants listed in figure 6.2. The monomer concentration is changed, as indicated, but the iron to monomer ratio is kept constant at 1:1. Sample volume is kept constant to 2 mL for all the samples, and the synthesis is carried out at room temperature.

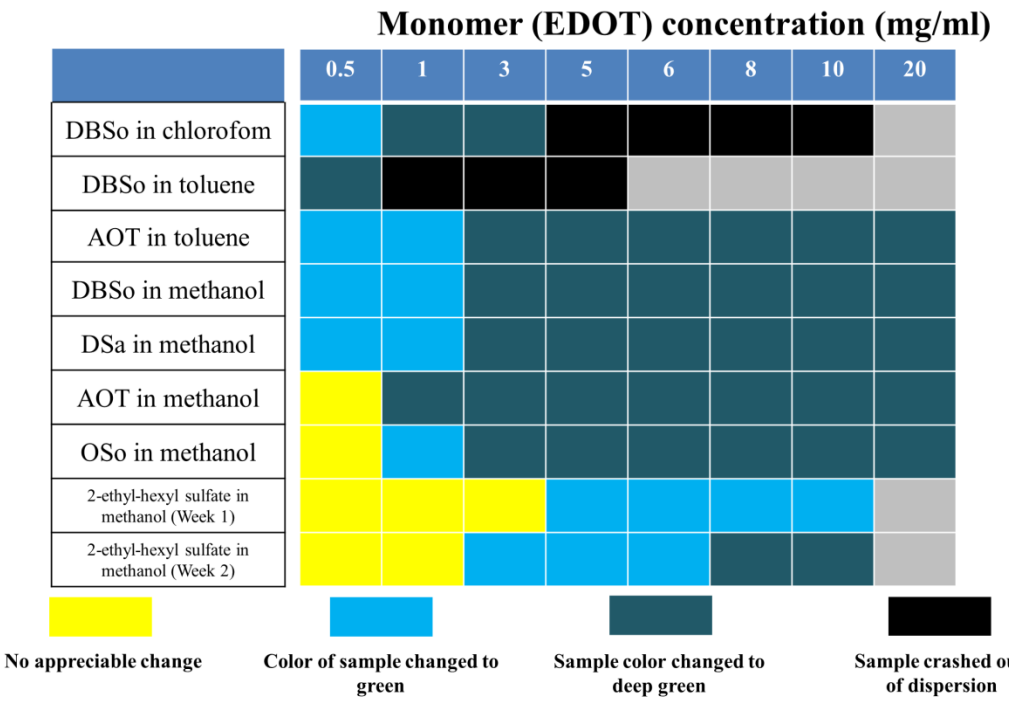

Iron complexes with dopants such as dioctyl sulfosuccinate (AOT 6.2a) and dodecylbenzene sulfonate (DBSo 6.2b) are dispersible in a wide variety of solvents including toluene, chloroform, and isopropyl alcohol. These organic iron salts readily polymerize EDOT and efficiently keep the PEDOT dispersions stable. Other complexes like dodecyl sulfate (DSa 6.2c), octyl sulfonate (OSo 6.2d), and 2-ethyl-hexyl sulfate (EHSa 6.2e) are only dispersible in alcohols and therefore can only polymerize EDOT in these solvents and therefore can only polymerize EDOT in these solvents. The surfactant iron salts are designed to deliver iron III ions for polymerization while also containing the functional groups sulfate or sulfonate in order to bind to the polymer like in other systems (i.e. PEDOT:PSS) [1]. Additionally, the alkyl chains of the surfactants need to be long enough to prevent PEDOT domains from interacting with each other and uncontrollably aggregating. Several surfactant-iron complexes of different chain lengths and head groups are investigated (figure 6.2). Surfactants with branched tails, which are found to

efficiently stabilize poly-3-alkylthiophenes and other conjugated polymers, are also studied (figure 6.2 a, e). Table 6.2 shows the state of the PEDOT synthesis using the different surfactant as dopants. The synthesis is carried out at room temperature, using different monomer concentrations, and a 1:1 iron to monomer ratio. The estate of the samples is reported a well after the synthesis started. The DSa, OSo and EHSa PEDOT complexes are only synthesized in methanol due to the limited compatibility of the iron salts with organic solvents.

Pairing PEDOT:OSo and PEDOT:EHSa complexes (PEDOT:Surfactant nomenclature is used to differentiate the complexes) will crash out of dispersion during synthesis. It is impossible to form a stable PEDOT dispersion with these samples even after the salt has been fully removed and the polymer is dried. PEDOT:DSa forms a stable dispersion prior to the purification steps but, after drying, it is impossible to re-suspend the product in any of the solvents that are evaluated in this work. In contrast, PEDOT:AOT and PEDOT:DBSo are stable and readily re-disperse in solvents after drying. OSo and EHSa chains are probably too short to efficiently prevent the aggregation of PEDOT chains. DSa is also too short to properly stabilize PEDOT that is dispersed in solvent after purification, but the excess of iron:DSa is probably interacting and stabilizing the polymer before purification. PEDOT:DBSo regularly forms a gel while being synthesized. However, the gel is easily broken and the purified polymer is very easy to re-disperse. PEDOT:AOT will never fall out of dispersion during synthesis but, after purification, it is harder to make a PEDOT:AOT dispersion compared to PEDOT:DBSo (i.e. requires longer sonication time). Dopants that stabilize PEDOT in organic solvents are generally those with relatively long alkyl chains. Shorter chains fail

to yield purified stable dispersions. The rest of this work focuses on the results obtained from the synthesis of PEDOT:AOT and PEDOT:DBSo but we note that several other surfactants are also likely to be good candidates for this application.

Characterization of the Polymer Mesostructure.

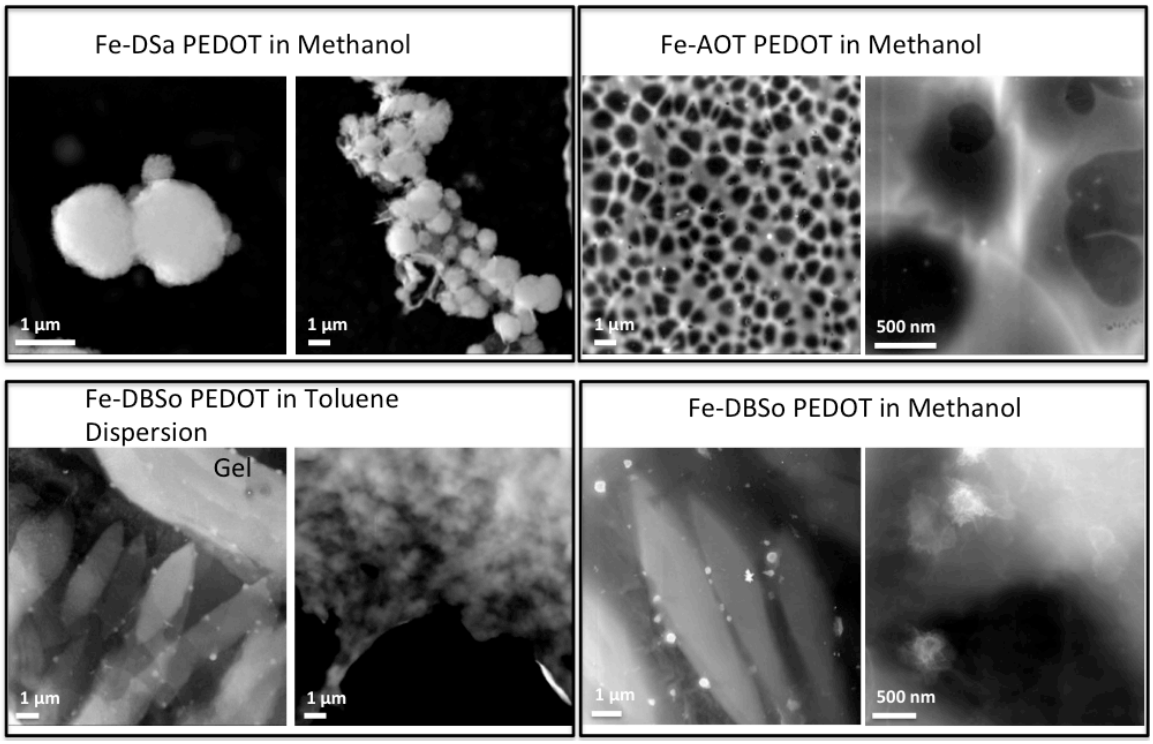

Figure 6.3: sTEM micrographs of PEDOT:DSa in methanol, PEDOT:AOT in methanol and PEDOT DBSo in toluene and methanol. All samples are 5 mg/ml EDOT without purification.

The conformation of the colloidal particles also changes depending on the surfactant that is used during polymerization. It is well know that dopants in PEDOT systems, such as PSS in PEDOT:PSS, will not fully prevent the aggregation of the polymer. PEDOT usually forms kinetically stable dispersions, rather than true polymer solutions, because at long times or higher concentrations aggregation still takes place. In

the case of PEDOT:PSS, it has been shown that polymer strands form rod-like domains when dispersed in water[1, 2]. Scanning transmission and scanning electron microscopy (sTEM and SEM) are performed in PEDOT:AOT and PEDOT:DBSo and PEDOT:DSa samples in order to explore their aggregate conformation. The conformation of the colloidal particles that the polymer forms changes depending on the dopant selection. Figure 6.3 shows sTEM micrographs of PEDOT doped with DSa, AOT, and DBSo before the purification step. The structure of the polymer domain changes from independent spheres in the case of DSa, to an interconnected network when AOT is used, and to what seems like ellipsoidal plates for DBSo. Similar structures are achieved when using the same dopant molecule in different solvents. The bottom part of figure 6.3 shows PEDOT:DBSo dispersions in toluene and methanol, and the presence of similar plate structures can be observed in both samples. These structures can be seen when the sample contains a fairly low PEDOT loading (2-5 mg/ml) and the excess iron salt is kept in the dispersion. The excess salt and the low concentrations stabilize the solvent into these defined structures. Once the concentration is increased, or the stabilizing salt removed, the polymer domains will start to further aggregate into mesoscopic structures.

It is necessary to purify the PEDOT:dopant complex because the iron salt remaining in the sample accounts for up to 30%wt of the total sample (up to 80%wt of the solids). This high concentration of the iron salt disrupts the properties of the polymer and gives the sample a green color (instead of the blue of the PEDOT). Figure 6.4 shows sTEM and SEM micrographs of PEDOT:AOT (6.4a, 6.4b), and PEDOT:DBSo (6.4d, 6.4e). These images represent the resulting polymer structure after the purification step takes place. The sTEM images do not show a marked difference between the

PEDOT:AOT and PEDOT:DBSo samples. Both polymer domains look like amorphous blobs. The solvent-polymer interface of PEDOT:DBSo looks smoother than the PEDOT:AOT which looks more cloudy and ill-defined. PEDOT:AOT also presents what appears to be two different characteristic sizes. The larger particles are similar to those of PEDOT:DBSo, at around 2-4 µm in diameter. The smaller particles (200-500 nm) do not appear in the PEDOT:DBSo samples (6.4c).

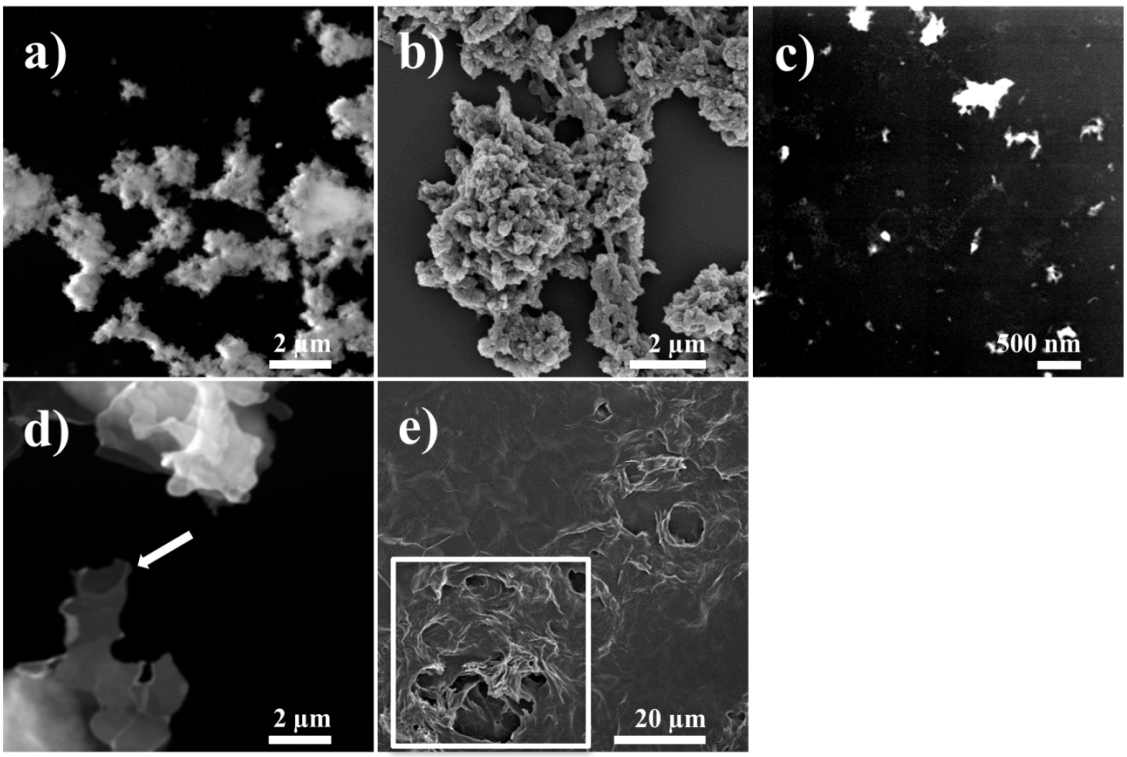

Figure 6.4: TEM (a, c, d) and SEM (b, e) micrographs of PEDOT:AOT (a, b, c) and PEDOT DBSo (d, e). a) and b) shows the bigger PEDO:AOT particles and their surface detail. c) Shows the detail of the smaller PEDOT:AOT domains present in the samples. d) e) Shows the PEDOT:DBSo domains, the arrow in d) points to sheet-like particles present in the samples, the square in e) marks the position of a scratch in the film.

SEM pictures reveal more details about the surface of the aggregate. PEDOT:AOT particles seem to be formed by well defined, sphere-like polymer building blocks. These sphere-like objects are approximately 200-250 nm in diameter based on sTEM. The existence of these spherical building blocks makes it possible to fragment the larger domains into the smaller pieces observed in the sTEM samples. However, it is counter intuitive that this sample is actually harder to re-disperse than other PEDOT complexes. Pictures of PEDOT:DBSo show a very smooth polymer surface. When focused on the scratched surface regions (square in figure 6.4e) it looks like the PEDOT:DBSo building blocks are polymer sheets. These sheet-like structures also appear in the sTEM images (arrow in figure 6.4d). Since the sTEM images are obtained from dried dispersions, the sheet-like particles are not very evident because they all crumble up into amorphous blobs. From the electron microscope images it is evident that the surface area of PEDOT:AOT particles is much higher than that of the smooth PEDOT:DBSo domains. Unfortunately, the processing required to image samples using electron microcopy can affect the structure of the sample so that it is difficult to characterize these more accurately based only on sTEM.

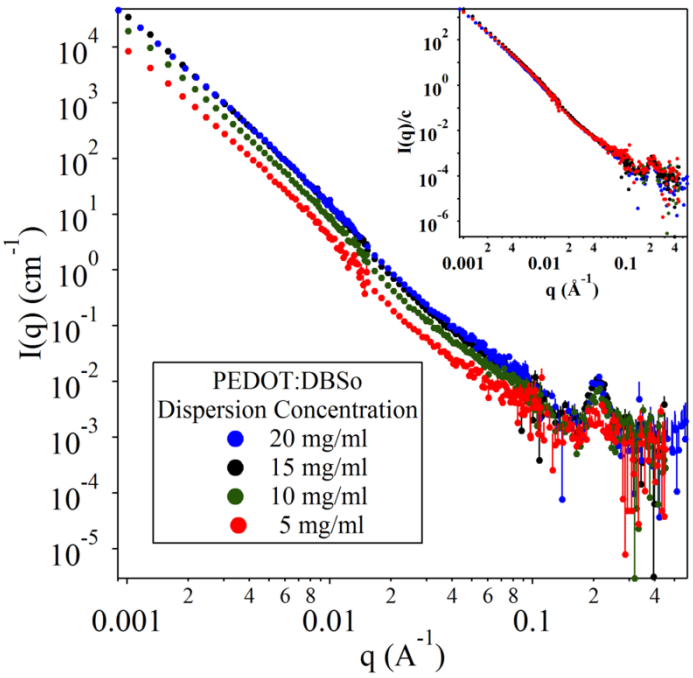

Figure 6.5: Small angle neutron scattering (SANS) profiles of PEDOT:DBSo at different concentrations in absolute scale. Insert: Same scattering curves normalized to concentration.

Small angle neutron scattering (SANS) is performed on PEDOT complexes dispersions in order to probe the structure of the PEDOT domains without the artifacts induced by the preparation required for electron microscopy. Figure 6.5 shows the scattering profile of PEDOT:DBSo in d-chloroform at different concentrations. The scattering shows that between 5 and 20 mg/ml there is no substantial change in the shape of the scattering profile. This indicates that, in this concentration range, the sample is still below the critical overlap concentration and there are negligible contributions from structure factors so that the scattering profiles are dominated by the average shape of isolated particles. The insert in figure 6.5 shows the normalized profiles, showing that the scattering shape is independent of PEDOT concentration. A concentration of 15 mg/ml is used for the rest of the experiments in order to provide a good signal to noise level.

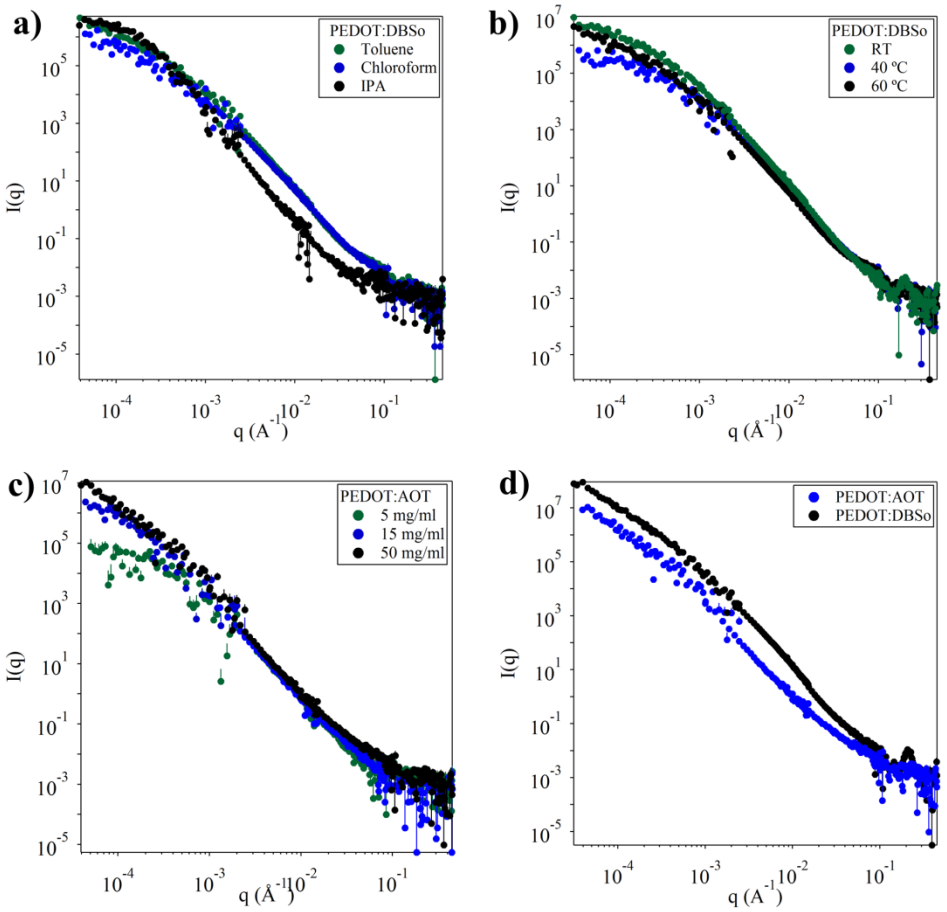

Figure 6.6: Scattering profiles of polymer synthesized at different conditions. a) PEDOT:DBSo synthesized in different solvents. b) PEDOT:DBSo synthesized at different temperature. c) PEDOT:AOT synthesized using different monomer concentrations. d) Comparison of PEDOT:AOT and PEDOT:DBSo synthesized under identical conditions.

Figure 6.6 shows combined SANS and desmeared USANS profiles of typical samples. The high-q ($q > 10^{-3}$ Å^{-1}) shows similar scattering profiles for PEDOT:DBSo synthesized in toluene and chloroform (fig 6.6a), and at different temperatures (fig 6.6b). PEDOT:AOT also show similar behavior at high q when synthesized using different monomer concentrations. Yet the, low-q region is clearly different (fig 6.6c). Large

differences are observed in the scattering profiles between PEDOT:AOT and PEDOT:DBSo (fig 6.6d). The mid-q power-law slope ($1 \cdot 10^{-3} < q < 2 \cdot 10^{-2} Å^{-1}$) consist of values that are close to 3 for PEDOT:AOT and values between 2.5-2.8 for PEDOT:DBSo (except when synthesized in IPA). These slopes describe the interface of the polymer complex and the solvent. Values near -2 are expected for the interface of rigid sheet-like objects (2D). They increase from -2 when sheets are curved (e.g. flexible) and when multiple 2D structures form part of larger complexes. In contrast, slopes between -4 and -3 are typical of three-dimensional solid objects with values closer to -4 indicating a perfectly smooth and sharp solid-solvent interface[21]. The results from these power law fits (table 1) are generally consistent with 2D interfaces for PEDOT:DBSo and rough 3D structures for PEDOT:AOT. The scattering profile of PEDOT:DBSo synthesized in IPA deviates from the rest of the DBSo samples. The mid-q power-law slope for this sample (3.68) is much larger than for PEDOT:DBSo polymerized in the other solvents. Fitting results of the SANS/USANS data are summarized in table 6.3.

Table 6.3: Results from the analysis of the SANS data performed on PEDOT complexes synthesized under different conditions. P.L. is the power law exponent at mid-q, S_v is the specific surface area of the samples.

PEDOT:AOT				PEDOT:DBSo				PEDOT:DBSo		
Con.	P.L.	S_v (m^2/g)		Solv.	P.L.	S_v (m^2/g)		Temp.	P.L.	S_v (m^2/g)
5	3.05	2.77		Tol	2.81	13.5		R.T.	2.67	26.4
15	3.16	1.27		Chl	2.56	N.A.		40 °C	2.83	27.8
50	3.26	0.75		IPA	3.68	0.61		60 °C	2.81	13.5

At low-q ($q < 10^{-3} Å^{-1}$) the difference among the different synthesis conditions is more evident indicating changes in particle size. PEDOT:DBSo synthesized in chloroform and toluene (figure 6.6a) still exhibit very similar behavior to each other. The

sample synthesized in IPA is once again different as it has a more defined Guinier region (i.e. plateau). The plateau starts at lower-q indicating the presence of large particles or structures when compared to syntheses in the other two solvents. Figure 6.4b shows that the temperature of the synthesis does not drastically influence the form factor of the scattering though there are likely small differences in particle size. Also there is not an evident trend of the change in scattering intensity with temperature. Monomer concentration during synthesis seems to be the most important parameter controlling the large-scale structure of PEDOT domains (figure 6.6c). The scattering behavior at low-q drastically changes with the monomer concentration and suggest that lower concentrations leads to smaller particle sizes.

The specific surface area of the polymer complexes is also extracted from the SANS scattering profiles by performing a Porod analysis on the samples[22]. The analysis is performed by plotting $I(q)\cdot q^4$ vs q for each sample. From this plot the Porod constant (P_c) is obtained from the flat regions. P_c is the value of $I(q)\cdot q^4$ at which the I(q) has a dependence of q^{-4} (i.e. $I(q)\cdot q^4$ has a slope of 0). The dependence of q^{-4} indicates the neutron beam is probing the interface between the PEDOT particles surface and the solvent at small length scales. From P_c the surface area per volume (Σ) can be calculated by using the equation:

$$\sum = \frac{P_c}{2\pi(\Delta SLD)^2} \text{(Eq. 6.1)}$$

Here, ΔSLD is the difference of the scattering length density of the solvent and the polymer complex. After obtaining Σ, the specific surface area (S_v) can be calculated using the equation:

$$S_v = \frac{\Sigma}{\rho_m \phi} \text{ (Eq. 6.2)}$$

Again, ρ_m is the mass density of the polymer and ϕ is the volume fraction of the polymer complex in the sample. Deviations from Porod behavior at high q are due to the internal structure of the polymers within the particles.

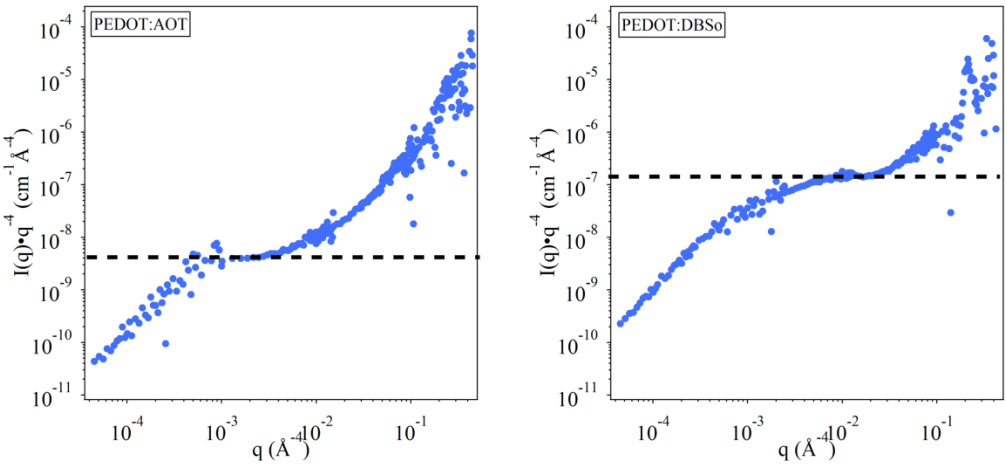

Figure 6.7: Representative Porod plots of PEDOT:AOT (left) and PEDOT:DBSo (right). The dashed lines indicate the portion in the data from which the Porod constant is taken.

Porod plots of PEDOT:DBSo and PEDOT:AOT are shown in figure 6.7, and table 6.1 contains the S_v values obtained from the Porod analysis. P_c for the PEDOT complexes is observed at relatively low-q (i.e. q ~0.002 $Å^{-1}$ for PEDOT:AOT and q ~0.01 $Å^{-1}$ for PEDOT:DBSo). This indicates that the polymer particles are relatively large and therefore the surface area turns out to be small. PEDOT:DBSo shows S_v values an order

of magnitude higher than the ones obtained for PEDOT:AOT. S_v also shows an inverse dependency with the concentration of the monomer during synthesis, indicating that in order to obtain a higher S_v more dilute batches should be synthesized. The temperature during synthesis does not appear to play a major role in S_v of the polymers when the temperature is maintained under a certain threshold. The sample synthesized at 60°C shows a drop in S_v and this hint for a change in the morphology of the PEDOT aggregate as the temperature of the synthesis rises. The solvent in which the polymer gets synthesized heavily affect the S_v parameter. PEDOT:DBSo synthesized in toluene shows a two order of magnitude higher S_v than the same polymer synthesized in IPA. PEDOT:DBSo synthesized in chloroform did not have a clear q^{-4} dependence, and therefore the value of P_c could not be obtained. It is worth mentioning that the samples in different solvents are all synthesized at 60 °C due to the low PEDOT yield in alcohols. This is probably a contributing factor for the lower values of S_v compared with other PEDOT:DBSo samples.

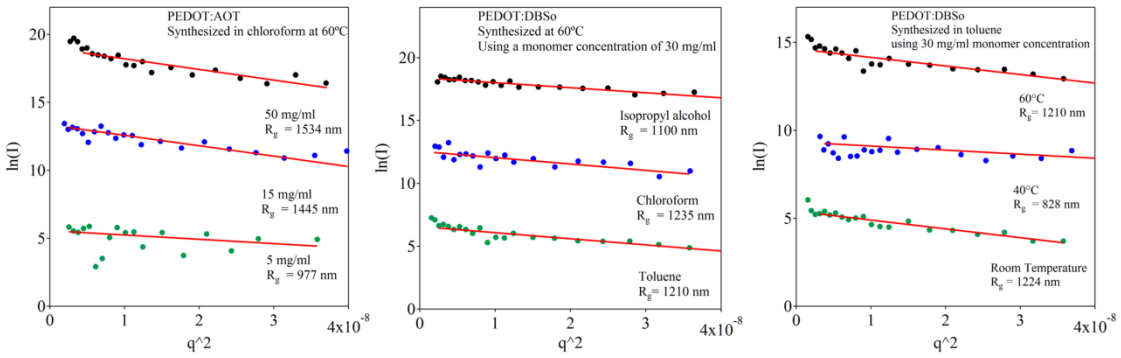

Figure 6.8: Fits performed to the ultra-small neutron scattering profile of PEDOT samples, synthesized at different conditions, using the Guinier model. The values of the radius of gyration, obtained from the fits, are listed in the legend of each graph, the values of $q \cdot R_g$ are also included to show that the fits meet the $q \cdot R_g < \sqrt{3}$. The data is shifted in the y-axis for clarity.

Further analysis is performed to the small-q region of the SANS profile ($4 \cdot 10^{-5} < q < 2 \cdot 10^{-3}$ Å^{-1}). The data is fit using the Guinier standard plot in order to obtain the radius of gyration (R_g) of the polymer particles in the dispersion[21, 22]. The Guinier standard plot consists on plotting the data in the form of the natural logarithm of the intensity versus q^2. The slope of the resulting line is equal to R_g^2 divided by 3. The radii of gyration obtained from the fits are listed in figure 6.8 and table 6.2. The fits reveal that the temperature during synthesis does not have a very large impact on the size of the polymer particles (figure 6.8 right). The values of R_g oscillate roughly between 800-1200 nm over the temperature range probed without a clear trend. The concentration of the monomer seems to cause a systematic change on the size of PEDOT particles (figure 6.8: left). At the highest monomer concentrations, R_g reaches a maximum value of ~1,500 nm. In contrast, when the synthesis concentration is low, R_g drops to ~1,000 nm. The solvent in which the synthesis takes place does not seem to to play a large role on the final particle size (figure 6.8 middle). The data indicates that the size of the PEDOT complex particles is around ~1,200 nm in all the solvents for otherwise identical synthesis conditions.

Table 6.4: R_H and R_g of PEDOT complexes. R_g is obtained by fits to the low-q range of the neutron scattering profiles. The values of R_H are obtained by dynamic light scattering.

PEDOT:AOT				PEDOT:DBSo				PEDOT:DBSo		
Con.	R_g (nm)	R_H (nm)		Solv.	R_g (nm)	R_H (nm)		Temp.	R_g (nm)	R_H (nm)
5	977	420, 99		Tol	1210	639, 138		R.T.	1225	735, 102
15	1445	1345, 240, 103		Chl	1235	704, 111		40 °C	828	501, 110
50	1534	1129, 256		IPA	1100	2741, 621, 93		60 °C	1210	639, 138

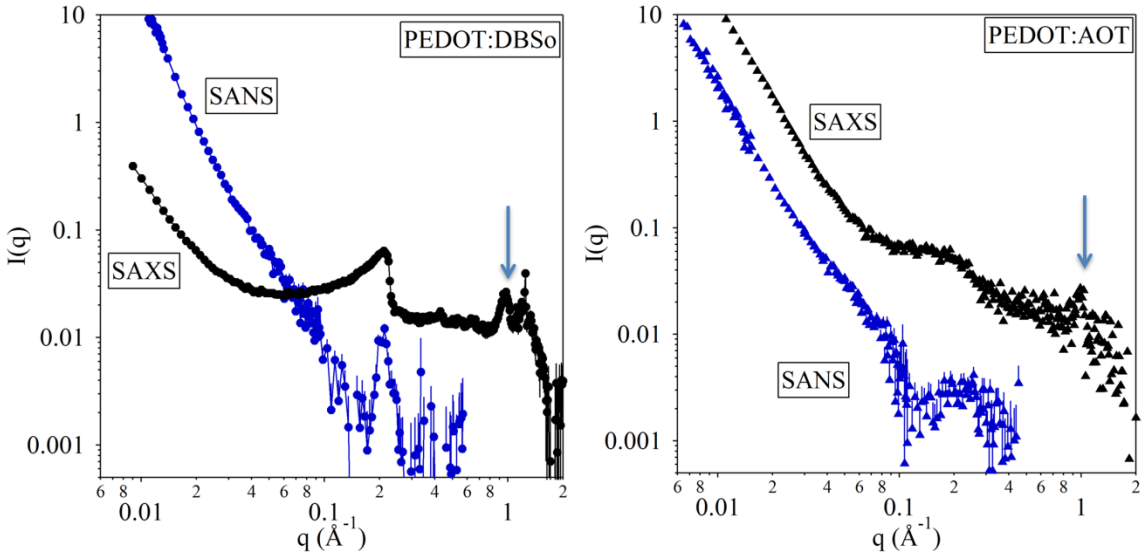

Figure 6.9: SAXS profiles of dried PEDOT:DBSo (left) and PEDOT:AOT (right) powder. The blue data is the SANS profiles of the PEDOT dispersion for comparison. The arrows mark a peak that appears in both PEDOT:DBSo and PEDOT:AOT samples.

Another marked difference between PEDOT:AOT and PEDOT:DBSo appears at very high q. Some of the PEDOT:DBSo profiles exhibit a well-defined peak at q ~0.21 Å^{-1}. The peak indicates the presence of a repetitive length of approximate 28 Å. The peak at this q position is not visible in any of the PEDOT:AOT profiles. In figure 6.6d a small increase in q can be observed for the PEDOT:AOT but this does not appear to be a crystalline feature as is indicated by the sharp peak of PEDOT:DBSo. In order to better

visualize this crystalline peak in the samples, small and wide angle x-ray scattering (SWAXS) was performed on dried polymer powders to reduce the background signal of the solvent and to increase the accessible q range. Figure 6.9 shows the x-ray scattering profiles for PEDOT:DBSo (left) and PEDOT:AOT (right). The x-ray scattering profile (black symbols) of PEDOT:DBSo shows several well-defined peaks at the same q position as the one observed in the SANS profile (blue symbols). The first and second harmonic of the peak can also be observed at q ~ 0.42 and 0.63 $Å^{-1}$, this suggests that a lamellar structure is being formed in these materials. The SAXS profile of PEDOT:AOT shows a very broad peak in a similar q position as the PEDOT:DBSo sample. The peaks, in this q-region, are probably caused by the polymer stacking. The characteristic size of the PEDOT:DBSo lamellar peak correspond to approximately 2 lengths of the DBSo chain (~17 Å)[23]. Meanwhile the peak in PEDOT:AOT is broad due to the disruption on the crystal lattice caused by the branching of the AOT chains, this disruption does not exist in the single-chain DBSo surfactant, and the resulting peak is very sharp.

At higher-q (~ 0.98 $Å^{-1}$) both PEDOT:DBSo and PEDOT:AOT present another peak (arrows in image 6.9). The presence of this peak in both samples leads us to conclude that the peak corresponds to a feature that is conserved. The position of this peak corresponds to characteristic features of approximately 6.4 Å in size. This is close to the reported size of PEDOT chain stacking, which is 6.8 Å, and is attributed to the π-π stacking caused by thiophene rings[2].

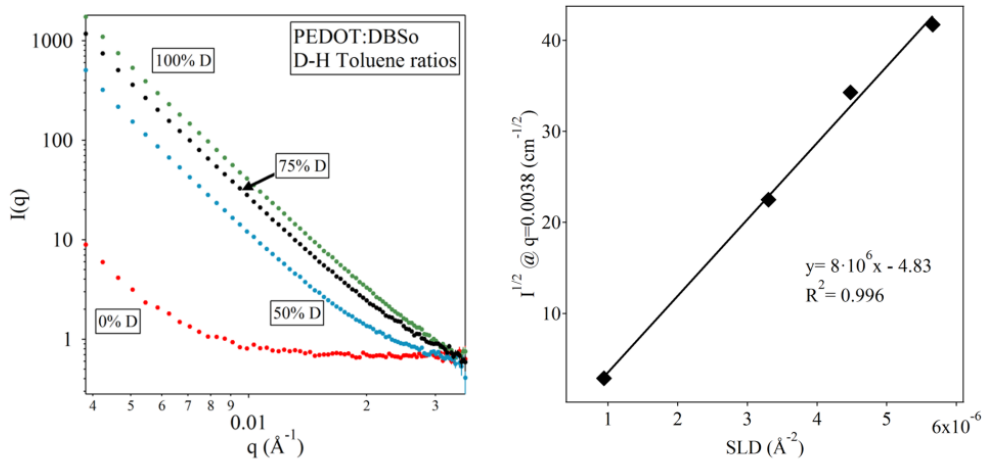

Figure 6.10: Left: Scattering profiles of PEDOT:DBSo at different deuterated and hydrogenated toluene ratios. Right: Square root of the scattering intensity at q=0.0038 Å^{-1} vs the solvents SLD. The points are fitted to a straight line; the equation of the line is showed in the graph.

The scattering length density (SLD) of the polymers is also evaluated using the method of contrast variation. The chosen solvent for this study is toluene due to the broad SLDs covered by the mixture of deuterated toluene (SLD= $5.40 \cdot 10^{-6}$ Å^{-2}) and hydrogenated toluene (SLD= $0.93 \cdot 10^{-6}$ Å^{-2}). PEDOT:DBSo is dispersed on different H-D toluene solvent ratios (100%$_{vol}$D, 75%$_{vol}$D, 50%$_{vol}$D, 0%$_{vol}$D). The scattering profile of the four samples is shown in figure 6.10 left. The square root of the intensity of each sample at q=0.0038 Å^{-1} is plotted vs the SLD of the solvent (figure 6.10 right). The data points are fit to a straight line so that the x-intercept of the line is equal to the SLD of the polymer (i.e. the point at which ΔSLD is 0). Using this method, we find that the SLD of PEDOT:DBSo is $0.60 \cdot 10^{-6}$ Å^{-2}. Unfortunately, the SLD for PEDOT:AOT could not be calculated due to the poor dispersability of the polymer in toluene. The magnitude of the SLD reveals that the amount of surfactant in the PEDOT:DBSo complex is high. Pure PEDOT only contains 4 hydrogen atoms and its SLD should be around $2.36 \cdot 10^{-6}$ Å^{-2}[24 24].

In order for the resulting SLD to be so low, it requires a large loading of hydrogen, which can be found in the aliphatic chain of the surfactant. The amount of hydrogen required to lower the SLD to $0.60 \cdot 10^{-6}$ $Å^{-2}$ also exceeds a 1:1 monomer:surfant ratio. This indicates that the PEDOT is decorated by large amounts of surfactant to the extent that more than one surfactant molecule is associating with any given PEDOT monomer.

Properties of PEDOT Complexes.

Dielectric spectroscopy measurements of PEDOT dispersions are performed in order to explore differences in electrical properties. Table 6.5 shows solid-state conductivities of dry polymers. These results highlight the variability in the properties of the synthesized conjugated polymers. PEDOT:AOT shows a range of an order of magnitude on its DC conductivity, while PEDOT:DBSo shows a conductivity fairly constant for all different batches tested. This high variability could be due to different degrees of doping in the AOT sample. Due to the solubility of the AOT chains in the solvent used to purify the polymer after synthesis, the number of washes and quantity of solvent used could have a big impact on the degree of doping and ultimately change the sample conductivity. The degree of doping and the variability it causes on the properties of the polymer is not further explored in this work, but it is worth exploring as a future research project.

Table 6.5: Conductivities of solid films of PEDOT:surfactant complexes.

Polymer	Conductivity (S/m)
PEDOT:AOT	$8.38 \cdot 10^{-2}$
PEDOT:DBSo	$3.60 \cdot 10^{-3}$

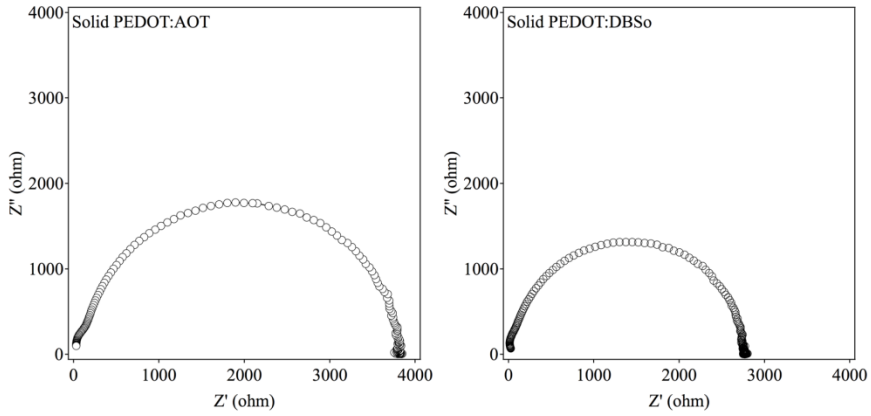

Figure 6.11: Cole – Cole plots of the polymers in solid state.

Figure 6.11 shows the Nyquist plots of the polymer in solid state. The Nyquist plot shows one semicircle for both PEDOT complexes.

Figure 6.12 shows the results for the UV-visible absorbance spectroscopy. The concentration of most samples is 2.5 mg/ml. For PEDOT:DBSo synthesized in IPA, the concentration had to be reduced by half (1.25 mg/ml) because the absorption was too large for the instrument. The uv-vis data for all the samples show three distinct behaviors. The polymers absorb light in the ultra-violet wavelength range (200-400 nm), followed by a valley (low absorbance) at visible light wavelengths (~450 nm). Finally there is an increase in the absorbance in the near infra-red (NIR) portion of the spectrum (< 600 nm). The absorption in the ultra violet range is due the polymer's band gap. It is expected for

PEDOT to have a relatively low degree of polymerization, and therefore the absorption wavelength of the polymer should fall within this range[25]. The different arrangement of the polymer chains and possible different doping efficiency can cause a change in the polymer's band gap and therefore yield a subtle change in the light absorbance profile. The dip in absorbance over the visible region of the spectra indicates that PEDOT complexes retain the characteristic transparency of other PEDOT presentations[1]. An increase in absorption in the NIR wavelength is observed in most of the samples. These have been observed for doped P3AT's and it is attributed to an increase of free charge carriers in the polymer[26].

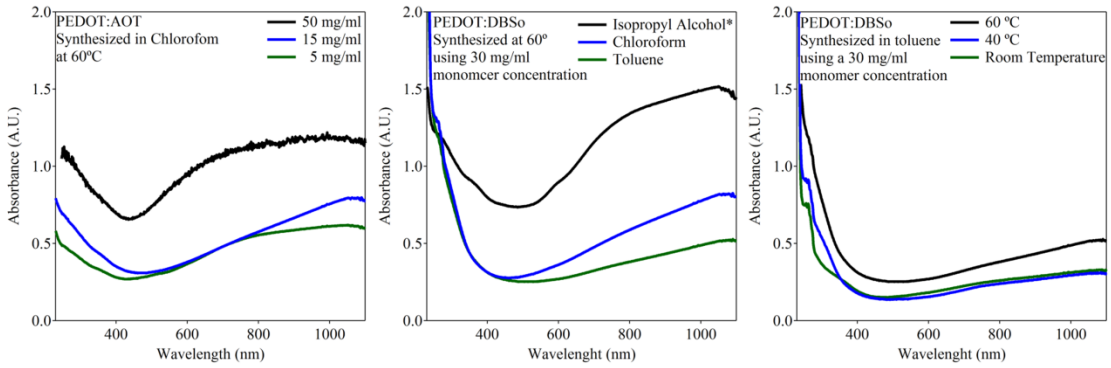

Figure 6.12: Uv-visible absorption of PEDOT complexes synthesized under different conditions. The sample of PEDOT:DBSo in IPA was diluted by a factor of two because the absorption was too high to be measured at the concentration of the other samples (2.5 mg/mL).

The hydrodynamic radii (R_H) of PEDOT, synthesized under different condition, obtained by DLS are listed in the Table 6.4. The DLS data showed at least two populations of aggregate sizes for most of the samples. Samples such as PEDOT:DBSo synthesized in IPA and PEDOT:AOT with monomer concentration of 15 mg/ml, show a size. The prevalent aggregate size for PEDOT:DBSo samples has an R_H of 500-700 nm,

meanwhile PEDOT:AOT particles are generally above 1 µm in hydrodynamic radius. Table 6.4 contains the R_g from the SANS fit and compares it with the R_H obtained from DLS. The presence of the larger particles that appear in the DLS data (700-1200 nm) explains the deviation from the Guinier behavior for some of the SANS samples at low-q. The R_g seems to match well with the values of the large fraction of aggregates in terms of R_H. R_g and R_H do not only match in magnitude, but also in the relative size among samples. Monomer concentration shows the same trend where 15 and 50 mg/ml show similar R_H (~1200) and 5 mg/ml produce smaller PEDOT particles of ~420 nm. The same occurs with solvent changes where R_H is very constant among all the solvent, around 600-700 nm. However, IPA samples do show larger particles of ~3 µm in R_H. These particles do not appear in the neutrons scattering data probably due to the resolution limits of the instrument. The sizes shown in the temperature series once again show that the polymer synthesized at 40ºC has smaller aggregates than those synthesized at 60 ºC and room temperature. In general the R_H is slightly smaller than R_g (except for the large particles of IPA), but a difference between these two parameters is expected since R_H and R_g are two different representations of the system. The DLS size distribution profile can be found in in figure 6.13

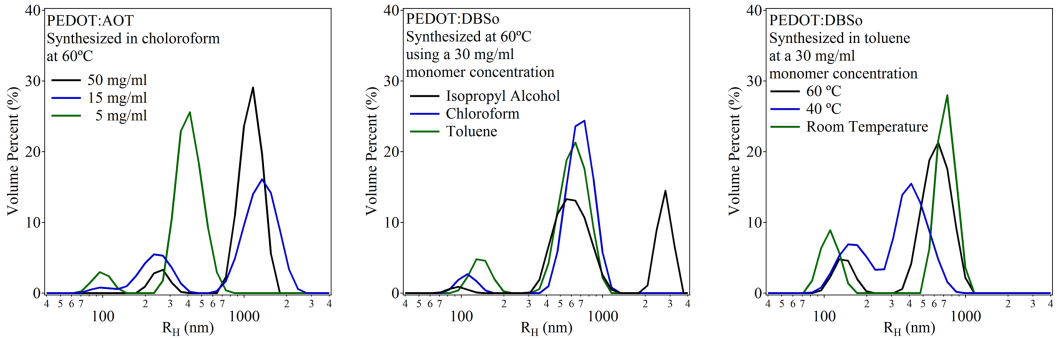

Figure 6.13: R_H distribution of the PEDOT complexes sizes, from different synthesis conditions, obtained by dynamic light scattering.

Conclusions.

This work describes a simple synthesis route for organic solvent-dispersible PEDOT. The PEDOT-organic solvent compatibility is obtained by the pairing of PEDOT chains with stabilizing surfactant dopants during synthesis. Several sulfates and sulfonates are evaluated but DBSo and AOT yield the most stable dispersions in toluene, chloroform and IPA. The morphology of different PEDOT complexes is evaluated by neutron, x-ray and light scattering techniques. PEDOT:DBSo shows smaller particles, with higher surface area and crystallinity than PEDOT:AOT. However, PEDOT:AOT particles proved to be significantly more conductive in dispersion and in the solid state.

The effect of temperature, solvent and monomer concentration on the morphology of the PEDOT complex is also evaluated. Polymerization temperature seems to play a small role in the aggregate size, even when it greatly affects the kinetics of reaction and the surface area of the polymer domains. Meanwhile solvent and monomer concentration have a larger impact in the structure of the polymer particles.

Development of Conductive Paints for Static Charge Dissipation.

The market size for electrostatic dissipation coatings is approximately 4.3 billion dollars and is expected to grow with the continued increase of the electronics market and the incorporation of plastic composites for transportation applications[27]. The purpose of these coatings is electromagnetic effect management. The specific function of these

conductive, electrostatic dissipating coatings is the prevention of risks associated to lighting strikes and dissipation of static charge build-up. Particularly important is the engineering of low cost materials in order to protect large areas with electrostatic dissipation coatings.

In order to efficiently dissipate the electrostatic charge, the coating must have a sheet resistance within the range of 10^9-10^6 ohm/□[28]. Resistance within this range ensures efficient charge mitigation while simultaneously preventing the creation of high electrical currents. Currently, the antistatic coatings are made out of either conductive oxides (such as indium tin oxide) or by putting additives into paints (such as surfactants or metal nanoparticles)[29-32]. Oxides, albeit very efficient, are too expensive due to the rare earth elements used in their production. They also typically require vacuum-based deposition processes, making them very unpractical and expensive for large area antistatic applications.[33, 34] Metal nanoparticles and nanowires are the most common additives used in the industry. These systems can lead to low sheet resistances.[35-37] They, however, present many problems. First of all, metals have a high density, thereby adding a lot of weight per volume of additive (e.g. 19.3 g/ml for gold and 10.49 g/ml for silver). They are also composed of metal nanospheres, whose geometry requires a very high loading (~20-40%wt) in order to percolate the film and adequately dissipate charge, or nanowires which modify the rheological properties of the pain.[38, 39] These high loadings compromise the paint adhesion, optical properties (i.e. changes the color of the paint, and it is not possible to make transparent films), and the flexibility of the film. Carbon-based additives, such as carbon nanotubes and graphene, has been used to create conductive films, however they are hard to dispersed in order to create good quality coatings.[40, 41]

Intrinsically conductive polymers (ICP's) are promising candidates as paint additives to achieve electrostatic charge dissipating coatings. Their delocalized π orbital along the chain allow for charge transport, and the use of chemical dopants can enhance the mobility of charge carriers in the polymer. ICP also present relatively small densities (around 1g/ml) when compared to metals additives currently used. Also, the cost of synthesizing ICPs is much lower than conductive oxides due to the abundance of the elements which comprise them. The loading of the ICP can potentially be much lower than the metal nanoparticles due to the formation of polymer aggregates which lower the additive concentration require to achieve percolation. Finally, the ICP chemistry can be manipulated in order to obtain desirable properties in the material such as reducing light absorption in the visible spectra in order to render the material optically transparent. Poly(3,4-ethylenedioxythiophene) (PEDOT) is a particularly good candidate. PEDOT has a very high conductivity (500-1200 S/cm) and is a very robust material to environmental degradation[1]. PEDOT also has very low absorbance in the visible spectrum, which is a necessary property in order to keep the optical properties of the paint[1].

The PEDOT:Surfactant dispersions discussed in this chapter can be readily incorporated into commercially available paints in order to render the paint conductive. The objectives of the additives are to make a film with conductivities within the range for electrostatic dissipation while maintaining the optical properties of the paint. For the current study, paints that produce optically clear (i.e. transparent) films are tested in order to readily observed deviations from this property caused by the additive integration into the paint (i.e. films of paint and PEDOT additive should be transparent). This PEDOT

additive has been tested with paints of several characteristics and compositions, showing different degrees of additive-matrix compatibility and film conductivity.

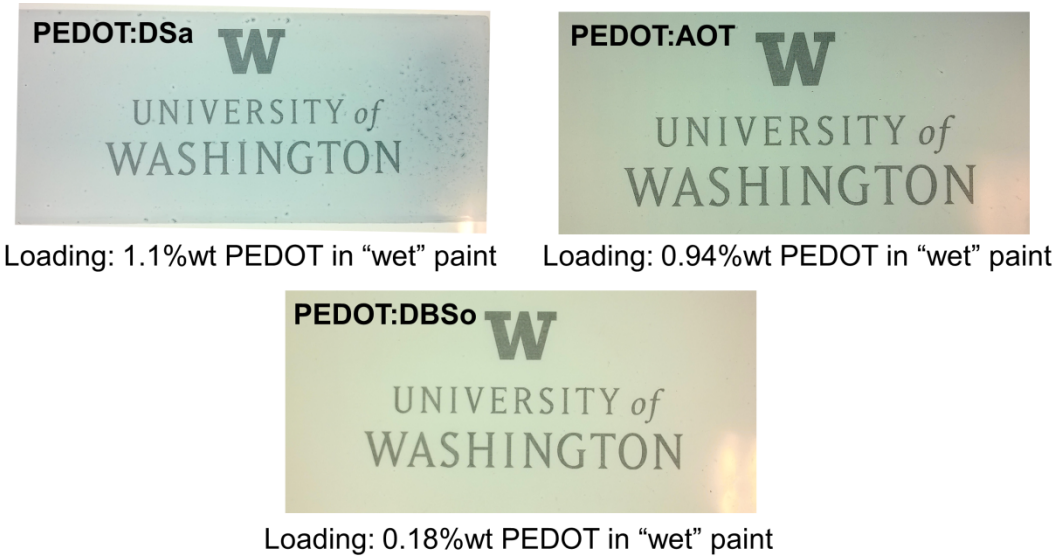

Figure 6.14: Films coated using Perma New 6000 paint with PEDOT complexes dispersed in methanol. Each film contains the type of PEDOT complex added to the paint and the polymer loading on the mixture before the solvents are evaporated.

Figures 6.14 and 6.15 show films casted with Perma-New 6000 by California Coatings with the addition of PEDOT additives dispersed in methanol (6.14) and toluene (6.15). Perman-New is a scratch resistant, clear coating for lenses and visors. Perman-New is composed of silica-filled methylpolysiloxane polymers dispersed in alcohols (alcohol based paint. These results show that the compatibility of the paint and the solvent, in which PEDOT is dispersed, is a key factor for the stability and effectiveness of the additive. Figure 6.14 shows that the methanol additives stay dispersed after being mixed with the alcohol-based paint. No macroscopic polymer aggregates are observed in the film, and the coating keeps its optical properties (i.e. stays transparent). On the other hand, when the PEDOT in toluene dispersions are mixed with Perman-New the polymer

rapidly aggregates, which translates into the grainy, optically opaque films observed in figure 6.15

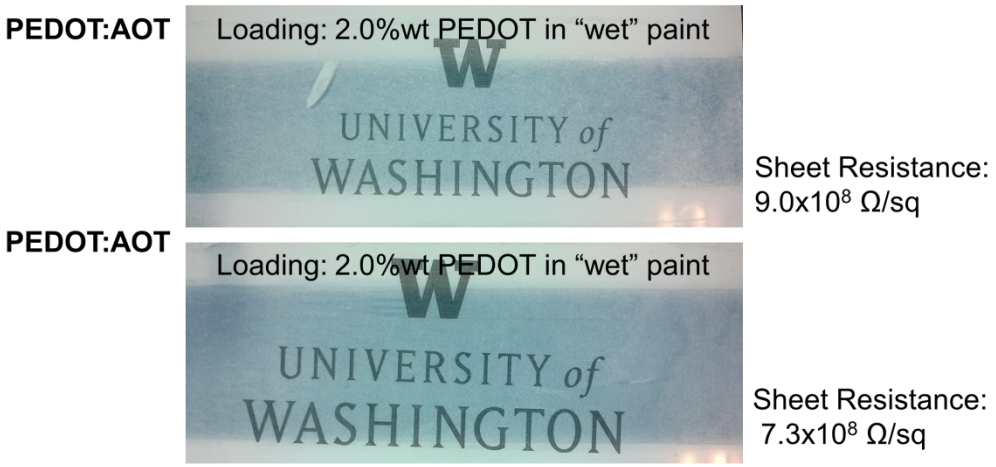

Figure 6.15: Films coated using Perma New 6000 paint with PEDOT complexes dispersed in toluene. Each film contains the type of PEDOT complex added to the paint, the measured sheet resistance of the sample and the polymer loading on the mixture before the solvents are evaporated

Films casted with Perma-New also highlight the importance of additive concentrations. The paint-additive samples made with toluene dispersion have at least double the PEDOT concentration than their methanol counterparts. This translated into the methanol-based additives not showing any charge transport, while the toluene based additives show sheet resistances well within the range necessary to prevent static charge build-up.

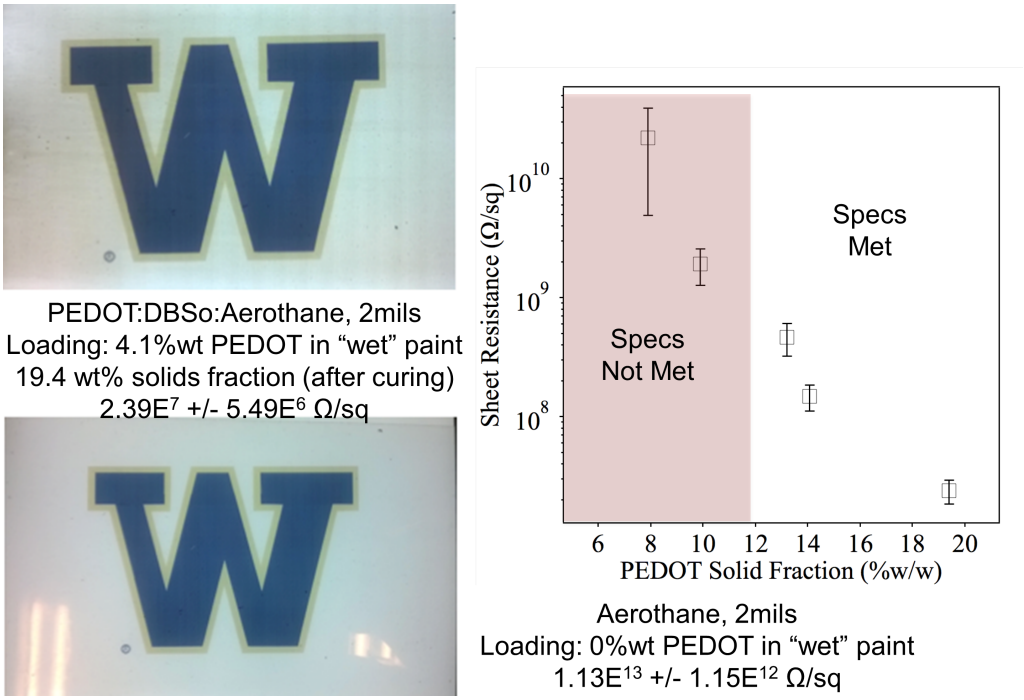

Figure 6.16: Left: Films coated using Aerothane by Polyfiber with PEDOT complexes dispersed in toluene. Each film contains the type of PEDOT complex added to the paint, the measured sheet resistance of the sample and the polymer loading on the mixture before the solvents are evaporated. Right: Sheet resistance as a function of the additive solid fraction.

Aerothane by Polyfiber is use to test the additive in a non-alcohol based paint. Aerothane is compatible with toluene and chloroform dispersions. Figure 6.16 shows films casted using Aerothane with PEDOT additive (top) and without PEDOT additive (bottom). The additive introduces some coloration to the paint. It also lowers the sheet resistance of the paint by 6 orders of magnitude. Figure 6.16 also shows a plot relating the PEDOT additive solid fraction to the sheet resistance of the casted films. In order to obtain a sheet resistance within the adequate range for electrostatic charge dissipation, the additive percentage in Aerothane should be at least 12wt%. At these loading, the optical properties of the paint change. The films starts showing coloration (figure 6.17) and turns

optically opaque (figure 6.17 left). In order to obtain a transparent film, the additive concentration needs to be reduced down to concentrations where the minimum conductivity required, for static charge dissipation, is not met.

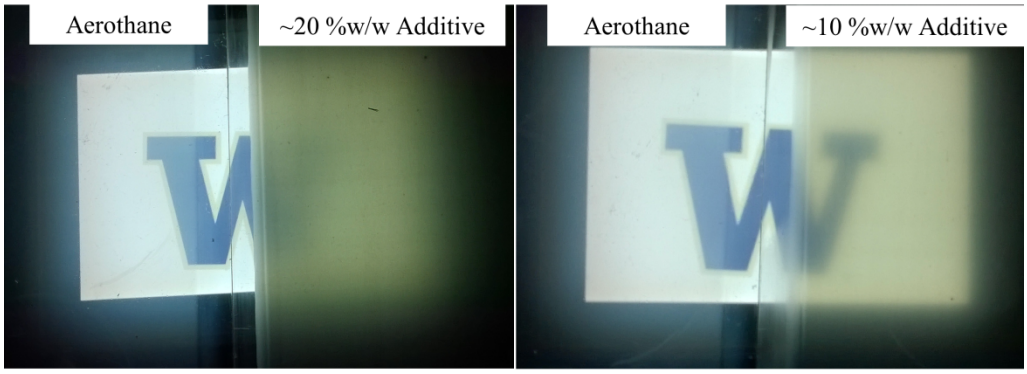

Figure 6.17: Comparison of the transparency of Aerothane before and after polymer addition. The film on the left shoes the lowest sheet resistance. The film on the right does not meet the minimum conductivity requirements for charge dissipation.

PEDOT complexes can be used as conductivity enhancers in paints for antistatic coating applications. The films showed in this dissertation already present conductivities within the appropriate range for static charge dissipation, but the required optical properties of the film have not been achieved. Several parameters can be changed in order to keep the additive from disrupting the optical properties of the paint. 1) A more conductive PEDOT complex can be used to lower the quantity of polymer additive that is needed. 2) Synthesis conditions (i.e. solvent choice, concentration of the monomers) can be selected to decrease the size of the polymer particles to reduce light scattering in the film.

References:

1. Elschner, A.; Kirchmeyer, S.; Lovenich, W.; Merker, U.; Reuter, K., *PEDOT: Principles and Application of an Intrinsically Conductive Polymer*. CRC Press: Boca Raton, Fl, 2011.
2. Kirchmeyer, S.; Reuter, K., Scientific importance, properties and growing applications of poly(3,4-ethylenedioxythiophene). *Journal of Materials Chemistry* 2005, 15, (21), 2077-2088.
3. Bubnova, O.; Khan, Z. U.; Malti, A.; Braun, S.; Fahlman, M.; Berggren, M.; Crispin, X., Optimization of the thermoelectric figure of merit in the conducting polymer poly(3,4-ethylenedioxythiophene). *Nature Materials* 2011, 10, (6), 429-433.
4. Jonsson, S. K. M.; Birgerson, J.; Crispin, X.; Greczynski, G.; Osikowicz, W.; van der Gon, A. W. D.; Salaneck, W. R.; Fahlman, M., The effects of solvents on the morphology and sheet resistance in poly (3,4-ethylenedioxythiophene)-polystyrenesulfonic acid (PEDOT-PSS) films. *Synthetic Metals* 2003, 139, (1), 1-10.
5. Carter, S. A.; Angelopoulos, M.; Karg, S.; Brock, P. J.; Scott, J. C., Polymeric anodes for improved polymer light-emitting diode performance. *Applied Physics Letters* 1997, 70, (16), 2067-2069.
6. Krebs, F. C., Air stable polymer photovoltaics based on a process free from vacuum steps and fullerenes. *Solar Energy Materials and Solar Cells* 2008, 92, (7), 715-726.
7. Jonas, F.; Morrison, J. T., 3,4-polyethylenedioxythiophene (PEDT): Conductive coatings technical applications and properties. *Synthetic Metals* 1997, 85, (1-3), 1397-1398.
8. Chen, L.; Yuan, C.; Dou, H.; Gao, B.; Chen, S.; Zhang, X., Synthesis and electrochemical capacitance of core-shell poly (3,4-ethylenedioxythiophene)/poly (sodium 4-styrenesulfonate)-modified multiwalled carbon nanotube nanocomposites. *Electrochimica Acta* 2009, 54, (8), 2335-2341.
9. Rao, C. R. K.; Muthukannan, R.; Jebin, J. A.; Raj, T. A.; Vijayan, M., Synthesis and properties of polypyrrole obtained from a new Fe(III) complex as oxidizing agent. *Indian Journal of Chemistry Section a-Inorganic Bio-Inorganic Physical Theoretical & Analytical Chemistry* 2013, 52, (6), 744-748.
10. Omastova, M.; Pionteck, J.; Trchova, M., Properties and morphology of polypyrrole containing a surfactant. *Synthetic Metals* 2003, 135, (1-3), 437-438.
11. Omastova, M.; Trchova, M.; Kovarova, J.; Stejskal, J., Synthesis and structural study of polypyrroles prepared in the presence of surfactants. *Synthetic Metals* 2003, 138, (3), 447-455.
12. Roncali, J.; Blanchard, P.; Frere, P., 3,4-Ethylenedioxythiophene (EDOT) as a versatile building block for advanced functional p-conjugated systems. *Journal of Materials Chemistry* 2005, 15, (16), 1589-1610.
13. Welzel, H. P.; Kossmehl, G.; Schneider, J.; Plieth, W., Reactive Groups on Polymer-Covered Electrodes. 2. Functionalized Thiophene Polymers by

Electrochemical Polymerization and Their Application as Polymeric Reagents. *Macromolecules* 1995, 28, (16), 5575-5580.
14. Lyskawa, J.; Le Derf, F.; Levillain, E.; Mazari, M.; Salle, M.; Dubois, L.; Viel, P.; Bureau, C.; Palacin, S., Univocal demonstration of the electrochemically mediated binding of Pb2+ by a modified surface incorporating a TTF-based redox-switchable ligand. *Journal of the American Chemical Society* 2004, 126, (39), 12194-12195.
15. McFarlane, S. L.; Deore, B. A.; Svenda, N.; Freund, M. S., A One-Step, Organic-Solvent Processable Synthesis of PEDOT Thin Films via in Situ Metastable Chemical Polymerization. *Macromolecules* 2010, 43, (24), 10241-10245.
16. Loevenich, W., PEDOT-Properties and Applications. *Polymer Science Series C* 2014, 56, (1), 135-143.
17. Glinka, C. J.; Barker, J. G.; Hammouda, B.; Krueger, S.; Moyer, J. J.; Orts, W. J., The 30 m small-angle neutron scattering instruments at the National Institute of Standards and Technology. *Journal of Applied Crystallography* 1998, 31, 430-445.
18. Barker, J. G.; Glinka, C. J.; Moyer, J. J.; Kim, M. H.; Drews, A. R.; Agamalian, M., Design and performance of a thermal-neutron double-crystal diffractometer for USANS at NIST. *Journal of Applied Crystallography* 2005, 38, 1004-1011.
19. Kline, S. R., Reduction and analysis of SANS and USANS data using IGOR Pro. *Journal of Applied Crystallography* 2006, 39, 895-900.
20. Plesse, C.; Vidal, F.; Randriamahazaka, H.; Teyssie, D.; Chevrot, C., Synthesis and characterization of conducting interpenetrating polymer networks for new actuators. *Polymer* 2005, 46, (18), 7771-7778.
21. Hammouda, B. Probing Nampscale Structures –The SANS Toolbox. http://www.ncnr.nist.gov/staff/hammouda/the_SANS_toolbox.pdf
22. Lindner, P., *Neutrons, X-Rays and Light: Scattering Methods Applied to Soft Condesed Matter.* Elsevier Science: Amsterdam, 2002.
23. Rai, R.; Baker, G. A.; Behera, K.; Mohanty, P.; Kurur, N. D.; Pandey, S., Ionic Liquid-Induced Unprecedented Size Enhancement of Aggregates within Aqueous Sodium Dodecylbenzene Sulfonate. *Langmuir* 2010, 26, (23), 17821-17826.
24. Kienzle, P. Neutron activation and scattering calculator. http://www.ncnr.nist.gov/resources/activation/
25. Bu, H.-B.; Goetz, G.; Reinold, E.; Vogt, A.; Azumi, R.; Segura, J. L.; Baeuerle, P., "Click"-modification of a functionalized poly(3,4-ethylenedioxythiophene) (PEDOT) soluble in organic solvents. *Chemical Communications* 2012, 48, (21), 2677-2679.
26. Tourillon, G.; Garnier, F., Effect of Dopant on the Physicochemical and Electrical-Properties of Organic Condcuting Polymer. *Journal of Physical Chemistry* 1983, 87, (13), 2289-2292.
27. Conductive Coatings in Electronics and Energy Markets. In NanoMarkets LLC: Glen Allen, VA, 2012.

28. Narkis, M.; Lidor, G.; Vaxman, A.; Zuri, L., New injection moldable electrostatic dissipative (ESD) composites based on very low carbon black loadings. *Journal of Electrostatics* 1999, 47, (4), 201-214.
29. Gelves, G. A.; Lin, B.; Sundararaj, U.; Haber, J. A., Low electrical percolation threshold of silver and copper nanowires in polystyrene composites. *Advanced Functional Materials* 2006, 16, (18), 2423-2430.
30. Nam, S.; Cho, H. W.; Lim, S.; Kim, D.; Kim, H.; Sung, B. J., Enhancement of Electrical and Thermomechanical Properties of Silver Nanowire Composites by the Introduction of Nonconductive Nanoparticles: Experiment and Simulation. *Acs Nano* 7, (1), 851-856.
31. Sun, Y.; Zhang, J.-M.; Xu, K.-W., First-principles study on the relaxed structures and electronic properties of Cu [110] nanowires. *Journal of the Korean Physical Society* 61, (7), 1015-1020.
32. Gelves, G. A.; Al-Saleh, M. H.; Sundararaj, U., Highly electrically conductive and high performance EMI shielding nanowire/polymer nanocomposites by miscible mixing and precipitation. *Journal of Materials Chemistry* 21, (3), 829-836.
33. Tolcin, A. C. *Mineral commodity summaries 2015*; Reston, VA C6 -, 2015; pp 74-75.
34. Minami, T., Transparent conducting oxide semiconductors for transparent electrodes. *Semiconductor Science and Technology* 2005, 20, (4), S35-S44.
35. Conductive-Compounds Ag-800 Silver Conductive Ink [Technical Data Sheet]. http://www.conductivecompounds.com/pdf/ag800-silver-filled-ink.pdf
36. Liu, C.-H.; Yu, X., Silver nanowire-based transparent, flexible, and conductive thin film. *Nanoscale Research Letters* 6.
37. Madaria, A. R.; Kumar, A.; Zhou, C., Large scale, highly conductive and patterned transparent films of silver nanowires on arbitrary substrates and their application in touch screens. *Nanotechnology* 22, (24).
38. Zallen, R., *The Physics of Amorphous Solids*. Wiley: New York, 1983.
39. Berry, V.; Gole, A.; Kundu, S.; Murphy, C. J.; Saraf, R. F., Deposition of CTAB-terminated nanorods on bacteria to form highly conducting hybrid systems. *Journal of the American Chemical Society* 2005, 127, (50), 17600-17601.
40. Azim, S. S.; Satheesh, A.; Ramu, K. K.; Ramu, S.; Venkatachari, G., Studies on graphite based conductive paint coatings. *Progress in Organic Coatings* 2006, 55, (1), 1-4.
41. Zhang, D.; Ryu, K.; Liu, X.; Polikarpov, E.; Ly, J.; Tompson, M. E.; Zhou, C., Transparent, conductive, and flexible carbon nanotube films and their application in organic light-emitting diodes. *Nano Letters* 2006, 6, (9), 1880-1886.

Chapter VII

Conclusions and Outlook

Conjugated Polymers Organogel Structures.

On chapter III and IV the formation of gels from conjugated polymers is explored. The control over the kinetics of aggregation is achieved by changing the gelation conditions. The results showed that the supersaturation of the system controls the kinetics of aggregation. The kinetics of the system modifies the structure of the organogel. A more ordered system will form when the kinetics are slow, and a more disordered, and bifurcated system is formed with fast kinetics. In order to control the gelation, different conditions are varied, which included the temperature of gelation, the solvent choice and solvent quality in which the polymers are dispersed before inducing gelation. However, many other parameters could also be used to control the supersaturation of the system. Chapter IV also shows how the properties of the samples are altered by the changes in the organogel conformation. The conductivity of the system shows a maximum, which probably coincides with an organogel structure ordered enough to form large domains that create a percolated network, thus facilitating charge transport, but at the same time the supersaturation of the system is high enough to maximize the quantity of polymer that transitioned into its crystalline state.

The control over these conjugated polymer organogels can be exploited. The organogel can be incorporated into a matrix (epoxy based paint) to render the matrix conductive.[1] Controlling the structure of the organogel prior to incorporating it in the matrix could maximize the properties to fit the necessities of the application. Due to the variability of the gelation behavior, shown in chapter IV, it is necessary to optimize the control over the gelation kinetics for each batch of polymer and set of conditions used.

Another possible area of interest already hinted in chapter IV it is the processing of the fibers into films. By tuning the kinetics of aggregation it is possible to create thin films of the organogels. This needs to be optimized for each set of conditions such as substrate, polymer backbone, solvent restrictions, coating method, etc. The different set of conditions needs to be fully explored in order to create a set of heuristic rules to cast films. These films could be used in applications such as solar cells. Some work that needs to be done is the exploration of techniques to backfill the spaces between polymer domains with a complementary semiconductor in order to create a heterojunction.

Ultimately the control over the structure of the organogel allows for the fine-tuning of the properties for any given application. Changing the conditions in which the organogel is formed can alter the conductivity of the system, the degree of aggregation of the polymer, the conformation and size of the polymer domains.

Metal Surfactant Complexes.

The substitution of the monovalent metal ion in surfactants for a polyvalent ion has been previously documented in the literature.[2-6] The dispersion of these multi-surfactant metal complexes into low dielectric constant solvent has also been previously

studied but only with surfactants which monovalent version already disperses in those kinds of solvents. The present work shows that the ion exchange can induce dispersability of a surfactant, in low dielectric constant solvents, even when the monovalent version of the surfactant is not dispersible (such as sodium lauryl sulfate and dodecyl benzene sulfonate). Also the present works pairs scattering techniques (neutron and X-ray) with molecular dynamics simulation (MD) in order to fully characterize the structure formed by these amphiphilic particles when dispersed in organic solvents. To further improve on this approach, two complementary scattering contrasts are simultaneously analyzed. The first contrasts (X-ray scattering) magnifies the behavior of the metallic ion in dispersion, while the second contrasts (neutron scattering) is chosen to focus on the conformation of the surfactant tails. The simultaneous analysis of these two scattering profiles guaranties a self-consistent description of the domains formed by these metallic complexes. The scattering and MD simulations both reveal the formation of elongated structures where the metallic ions are shielded from the solvent by the tails of the surfactants (i.e. an inverse micelle conformation). When an alcohol is used as the solvent to disperse the complexes, the scattering and MD simulations reveal that the metallic ions separate from each other due to a solvation layer formed with the interactions of the metal ion with the hydroxyl group in the solvent. However, the surfactant tails stay associated with the metallic ion under all the conditions probed. There is evidence of surfactant tails interacting with each other when dodecyl benzene sulfonate complexes are dissolved in alcohols, forming a sheet-like structure.

The properties of the complex dispersions are studied and this area could be further explored in future work. The electrical and electrochemical behavior of the

dispersions is tested, showing electrochemical activity and charge transport in solvents where the behavior is not usually obtained. The relatively simple synthesis of these complexes facilitates the exploration in using them for applications such as electrolytes for solvents with low dielectric constant or for charge transport in organic solvent-based flow batteries.[7, 8] Optimization of the system is necessary, such as the identification of the adequate metal ion and surfactant chain pair for any giving applications. Additional divalent metal ions such as cobalt^{2+} and iron^{2+}, and trivalent ions such as chromion^{3+} and gold $^{3+}$ have been tested for the creation of these complexes with varying degrees of success (complex cannot be formed with gold ions). Different surfactant tails have been also tested and most of them form a complex with the multivalent ions but only some will form dispersions in organic solvents. Only sulfate and sulfonates surfactants have been tested so far, but there is nothing prohibiting the use of other surfactant head group to form complexes.

The electrophoretic mobility of the complexes dispersed in organic solvent is indirectly probed when the ζ potential of the dispersions in toluene is measured. The result indicates a strong positive mobility (figure 5.18), which hints for the possibility of controlling the metallic complex domains by applying an electric field to the dispersion. The encapsulation of water in the core of the complexes' domain is also observed in this study and previously reported.[4] These two properties of the system could be exploited in order to develop a controlled carrier of aqueous media dispersed within a low dielectric constant solvent. Similar systems are already being studied as "smart surfactants" that react to an applied magnetic field.[2]

Poly(3,4-Ethylenedioxythiophene) Complex Dispersed in Organic Solvents

Poly(3,4-Ethylenedioxythiophene) (PEDOT) has several desired traits such as low absorbance in the visible wavelengths, high conductivity, and resistance to environmental conditions.[9] However the solubility of the polymer in most solvents is very low which makes the polymer hard to process. The present work describes a process to render PEDOT dispersible in organic solvents by doping the polymer with a surfactant. Using a surfactant with enough steric interactions to disrupt the aggregation of the polymer proved to be a key factor for the stabilization of the PEDOT dispersions. Dodecylbenzene sulfonate (DBSa) and dioctyl sulfonsuccinate (AOT) are the two surfactant, from the ones tested, that more efficiently disperse PEDOT. The structure of the PEDOT:DBSo and PEDOT:AOT complexes, synthesized using different conditions (solvent, temperature, monomer concentration), is tested using scattering techniques. All the samples produce micron-size aggregates. PEDOT:AOT appears to yield spherical aggregates while PEDOT:DBSo form sheet-like aggregates. The monomer concentration has the biggest impact in the aggregate size, where low concentration translates into smaller aggregates.

Much optimization is still required for this system. The purification steps needs to be optimized. Enough washing steps need to be performed in order to have the excess reactants removed from the sample, but not too many to decrease the doping by washing away the surfactant associated with the polymer chains. A more detailed study of the effect that the synthesis conditions have on the conductive properties of the polymer is needed in order to find the optimum set of conditions where the polymer has the highest

conductivity while retaining its dispersability. Additionally the dopant choice should also be explored. Based on the results for this study the longer the chain the more disruptive is to the aggregation of the polymer, and the more stable the dispersion results. However, the solubility of the dopant in the solvent was not taken into account for the surfactant selection on this study, an ideal dopant is a surfactant which stabilizes the PEDOT dispersion but at the same time has a limited solubility in the solvent so it stays associated with the polymer. Furthermore, a very long and bulky surfactant would hinder the charge transport properties of the complex.

The processability of PEDOT in organic solvents opens the possibility for the use of the polymer in new applications. The inclusion of PEDOT complexes into organic solvent-based paints is explored in the present work. The purpose is to create a conductive and optically transparent film for static charge dissipation. The PEDOT complexes are successfully dispersed into the paints, although some optimization of the complex compatibility with the paint is necessary. The conductivities of the resulting films are within the adequate range for static charge dissipation. The adhesion properties of the paints also are not affected by the inclusion of the PEDOT additive, which resulted in films resistant to scratches. The transparency of the film is still not achieved. The necessary work to achieve this goal is tied with the optimization of the conditions that increases the conductivity of the polymer. An increment in the conductivity will allow for a decrease in the amount of additive necessary to achieve adequate conductivities. Lower additive concentrations produce less opaque films as seen in figure 6.17. Alternatively, a dopant surfactant that disperses more efficiently the polymer domains could be found.

The smaller PEDOT domains would translate in a decreased in the light scattering caused by the addition of the polymer domains, and increase the transparency of the film.

References.

1. Pozzo, D.; Newbloom, G., Composites incorporating a conductive polymer nanofiber network. In Google Patents: 2013.
2. Brown, P.; Butts, C. P.; Eastoe, J.; Glatzel, S.; Grillo, I.; Hall, S. H.; Rogers, S.; Trickett, K., Microemulsions as tunable nanomagnets. *Soft Matter* 2012, 8, (46), 11609-11612.
3. Dunn, C. M.; Robinson, B. H.; Leng, F. J., Photon-Correlation Spectroscopy Applied to the Size Characterization of Water-in-Oil Microemulsion Systems Stabilized by Aerosol-OT Effect of Change in Counterion. *Spectrochimica Acta Part a-Molecular and Biomolecular Spectroscopy* 1990, 46, (6), 1017-1025.
4. Eastoe, J.; Fragneto, G.; Robinson, B. H.; Towey, T. F.; Heenan, R. K.; Leng, F. J., Variation of Surfactant Counterion and its Effect on the Structure and Properties of Aerosol-OT-Based Water-in-Oil Microemulsions. *Journal of the Chemical Society-Faraday Transactions* 1992, 88, (3), 461-471.
5. Haynes, J. S.; Sams, J. R.; Thompson, R. C., Sythesis and Structural Studies of Iron(II) and Iron(III) Sulfonates. *Canadian Journal of Chemistry-Revue Canadienne De Chimie* 1981, 59, (4), 669-678.
6. Longo, A.; Ruggirello, A.; Liveri, V. T., Physicochemical investigation of nanostructures in liquid phases: Ytterbium nitrate ionic clusters confined in ytterbium bis(2-ethylhexyl) sulfosuccinate reversed micelles and liquid crystals. *Chemistry of Materials* 2007, 19, (5), 1127-1133.
7. Shinkle, A. A.; Pomaville, T. J.; Sleightholme, A. E. S.; Thompson, L. T.; Monroe, C. W., Solvents and supporting electrolytes for vanadium acetylacetonate flow batteries. *Journal of Power Sources* 2014, 248, 1299-1305.
8. Zhang, D.; Lan, H.; Li, Y., The application of a non-aqueous bis(acetylacetone)ethylenediamine cobalt electrolyte in redox flow battery. *Journal of Power Sources* 2012, 217, 199-203.
9. Kirchmeyer, S.; Reuter, K., Scientific importance, properties and growing applications of poly(3,4-ethylenedioxythiophene). *Journal of Materials Chemistry* 2005, 15, (21), 2077-2088.

Chapter VII

Bibliography

Alcazar, D., Wang, F., Swager, T. M., and Thomas, E. L. (2008). Gel Processing for Highly Oriented Conjugated Polymer Films. Macromolecules *41*, 9863-9868.

Assadi, A., Svensson, C., Willander, M., and Inganas, O. (1988). FIELD-EFFECT MOBILITY OF POLY(3-HEXYLTHIOPHENE). Applied Physics Letters *53*, 195-197.

Azim, S. S., Satheesh, A., Ramu, K. K., Ramu, S., and Venkatachari, G. (2006). Studies on graphite based conductive paint coatings. Progress in Organic Coatings *55*, 1-4.

Ballauff, M. (1986). Phase equilibria in rodlike systems with flexible side chains. Macromolecules *19*, 1366-1374.

Barker, J. G., Glinka, C. J., Moyer, J. J., Kim, M. H., Drews, A. R., and Agamalian, M. (2005). Design and performance of a thermal-neutron double-crystal diffractometer for USANS at NIST. Journal of Applied Crystallography *38*, 1004-1011.

Berg, J. C. (2010). An Introduction to Interfaces and Colloids: The Bridge to Nanoscience, (Singapore: World Scientific Publishing Co. Pte. Ltd.).

Bergenholtz, J., Romagnoli, A. A., and Wagner, N. J. (1995). VISCOSITY, MICROSTRUCTURE, AND INTERPARTICLE POTENTIAL OF AOT/H2O/N-DECANE INVERSE MICROEMULSIONS. Langmuir *11*, 1559-1570.

Bernius, M. T., Inbasekaran, M., O'Brien, J., and Wu, W. S. (2000). Progress with light-emitting polymers. Advanced Materials *12*, 1737-1750.

Berr, S. S. (1987). Solvent Isotope Effects on Alkyltrimethylammonium Bromide Micelles as a Function of Alkyl Chain-Lenght. Journal of Physical Chemistry *91*, 4760-4765.

Berry, V., Gole, A., Kundu, S., Murphy, C. J., and Saraf, R. F. (2005). Deposition of CTAB-terminated nanorods on bacteria to form highly conducting hybrid systems. Journal of the American Chemical Society *127*, 17600-17601.

Berson, S., De Bettignies, R., Bailly, S., and Guillerez, S. (2007). Poly (3-hexylthiophene) fibers for photovoltaic applications. Adv Funct Mater *17*, 1377-1384.

Beunis, F., Strubbe, F., Karvar, M., Drobchak, O., Brans, T., and Neyts, K. Inverse micelles as charge carriers in nonpolar liquids: Characterization with current measurements. Current Opinion in Colloid & Interface Science *18*, 129-136.

Beunis, F., Strubbe, F., Karvar, M., Drobchak, O., Brans, T., and Neyts, K. (2013). Inverse micelles as charge carriers in nonpolar liquids: Characterization with current measurements. Current Opinion in Colloid & Interface Science *18*, 129-136.

Bond, A. M., Fleischmann, M., and Robinson, J. (1984). Electrochemistry in Organic-Solvents Without Supporting Electrolyte Using Platinium Microelectrodes. Journal of Electroanalytical Chemistry *168*, 299-312.

Brown, P., Butts, C. P., Cheng, J., Eastoe, J., Russell, C. A., and Smith, G. N. (2012a). Magnetic emulsions with responsive surfactants. Soft Matter *8*, 7545-7546.

Brown, P., Butts, C. P., Eastoe, J., Glatzel, S., Grillo, I., Hall, S. H., Rogers, S., and Trickett, K. (2012b). Microemulsions as tunable nanomagnets. Soft Matter *8*, 11609-11612.

Brown, P., Khan, A. M., Armstrong, J. P. K., Perriman, A. W., Butts, C. P., and Eastoe, J. (2012c). Magnetizing DNA and Proteins Using Responsive Surfactants. Advanced Materials *24*, 6244-6247.

Bu, H.-B., Goetz, G., Reinold, E., Vogt, A., Azumi, R., Segura, J. L., and Baeuerle, P. (2012). "Click"-modification of a functionalized poly(3,4-ethylenedioxythiophene) (PEDOT) soluble in organic solvents. Chemical Communications *48*, 2677-2679.

Bubnova, O., Khan, Z. U., Malti, A., Braun, S., Fahlman, M., Berggren, M., and Crispin, X. (2011). Optimization of the thermoelectric figure of merit in the conducting polymer poly(3,4-ethylenedioxythiophene). Nature Materials *10*, 429-433.

Burrows, H. D., and Tapia, M. J. (2002). Lanthanide ion binding in AOT/water/isooctane microemulsions. Langmuir *18*, 6706-6708.

Butler, P., Alina, G., Hernandez, R. C., Doucer, M., Jackson, A., Kienzle, P., Kline, S. R., and Zhou, J. SASView for Small Angle Scattering Analysis. In.

Caboi, F., Capuzzi, G., Baglioni, P., and Monduzzi, M. (1997). Microstructure of Ca-AOT/water/decane w/o microemulsions. Journal of Physical Chemistry B *101*, 10205-10212.

Capek, I. (2003). The inverse mini-emulsion polymerization of acrylamide. Designed Monomers and Polymers *6*, 399-409.

Capuzzi, G., Baglioni, P., Gambi, C. M. C., and Sheu, E. Y. (1999). Percolation phenomenon of calcium bis(2-ethylhexyl) sulfosuccinate water-in-oil microemulsions by conductivity and dielectric spectroscopy measurements. Physical Review E *60*, 792-798.

Carter, S. A., Angelopoulos, M., Karg, S., Brock, P. J., and Scott, J. C. (1997). Polymeric anodes for improved polymer light-emitting diode performance. Applied Physics Letters *70*, 2067-2069.

Chang, J. F., Sun, B. Q., Breiby, D. W., Nielsen, M. M., Solling, T. I., Giles, M., McCulloch, I., and Sirringhaus, H. (2004). Enhanced mobility of poly(3-hexylthiophene) transistors by spin-coating from high-boiling-point solvents. Chemistry of Materials *16*, 4772-4776.

Chang, M.-Y., Huang, Y.-H., and Han, Y.-K. (2014). Aggregation, crystallization, and resistance properties of poly(3-hexylthiophene-2,5-diyl) solid films gel-cast from CHCl3/p-xylene mixed solvents. Organic Electronics *15*, 251-259.

Chen, C. Y., Chang, C. S., Huang, S. W., Chen, J. H., Chen, H. L., Su, C. L., and Chen, S. A. (2010). Phase-Separation-Induced Gelation of Poly(9,9-dioctylfluorene) Methylcyclohexane Solution. Macromolecules *43*, 4346-4354.

Chen, J.-H., Chang, C.-S., Chang, Y.-X., Chen, C.-Y., Chen, H.-L., and Chen, S.-A. (2009a). Gelation and Its Effect on the Photophysical Behavior of Poly(9,9-dioctylfluorene-2,7-diyl) in Toluene. Macromolecules *42*, 1306-1314.

Chen, J.-Y., Hsu, F.-C., Sung, Y.-M., and Chen, Y.-F. (2012). Enhanced charge transport in hybrid polymer/ZnO-nanorod solar cells assisted by conductive small molecules. Journal of Materials Chemistry *22*, 15726-15731.

Chen, L., Yuan, C., Dou, H., Gao, B., Chen, S., and Zhang, X. (2009b). Synthesis and electrochemical capacitance of core-shell poly (3,4-ethylenedioxythiophene)/poly (sodium 4-styrenesulfonate)-modified multiwalled carbon nanotube nanocomposites. Electrochimica Acta *54*, 2335-2341.

Chen, S. H., Chou, H. L., Su, A. C., and Chen, S. A. (2004). Molecular packing in crystalline poly(9,9-di-n-octyl-2,7-fluorlene). Macromolecules *37*, 6833-6838.

Choi, N. H., Kwon, S.-K., and Kim, H. (2013). Analysis of the Oxidation of the V(II) by Dissolved Oxygen Using UV-Visible Spectrophotometry in a Vanadium Redox Flow Battery. Journal of the Electrochemical Society *160*, A973-A979.

Conductive Coatings in Electronics and Energy Markets. In, (Glen Allen, VA: NanoMarkets LLC). (2012)

Conductive-Compounds (2014). Ag-800 Silver Conductive Ink [Technical Data Sheet]. In.

Connelly, N. G., and Geiger, W. E. (1996). Chemical redox agents for organometallic chemistry. Chemical Reviews *96*, 877-910.

de la Iglesia, P., and Pozzo, D. C. (2013). Effects of supersaturation on the structure and properties of poly(9,9-dioctylfluorene) organogels. Soft Matter *9*, 11214-11224.

de Oliveira, R. J., Brown, P., Correia, G. B., Rogers, S. E., Heenan, R., Grillo, I., Galembeck, A., and Eastoe, J. (2011). Photoreactive Surfactants: A Facile and Clean Route to Oxide and Metal Nanoparticles in Reverse Micelles. Langmuir *27*, 9277-9284.

deLeeuw, D. M., Simenon, M. M. J., Brown, A. R., and Einerhand, R. E. F. (1997). Stability of n-type doped conducting polymers and consequences for polymeric microelectronic devices. Synthetic Metals *87*, 53-59.

Denat, A., Gosse, B., and Gosse, J. P. (1981). Electrical Conductivity of Solutions of an Ionic Sufactant in Hydrocarbons. Revue De Physique Appliquee *16*, 673-678.

Dukhin, A. (2014). Critical concentration of ion-pairs formation in nonpolar media. Electrophoresis *35*, 1773-1781.

Dukhin, A., and Parlia, S. (2012). Ions, ion pairs and inverse micelles in non-polar media. Current Opinion in Colloid & Interface Science *18*, 93-115.

Dukhin, A., and Parlia, S. (2015). Ions, ion pairs and inverse micelles in non-polar media. Current Opinion in Colloid & Interface Science *18*, 93-115.

Dunn, C. M., Robinson, B. H., and Leng, F. J. (1990). Photon-Correlation Spectroscopy Applied to the Size Characterization of Water-in-Oil Microemulsion Systems Stabilized by Aerosol-OT Effect of Change in Counterion. Spectrochimica Acta Part a-Molecular and Biomolecular Spectroscopy *46*, 1017-1025.

Eastoe, J., Fragneto, G., Robinson, B. H., Towey, T. F., Heenan, R. K., and Leng, F. J. (1992a). Variation of Surfactant Counterion and its Effect on the Structure and Properties of Aerosol-OT-Based Water-in-Oil Microemulsions. Journal of the Chemical Society-Faraday Transactions *88*, 461-471.

Eastoe, J., Fragneto, G., Steytler, D. C., Robinson, B. H., and Heenan, R. K. (1992b). Small-Angle Neutron Scattering From Novel Bis-2-Ethylenesulphosuccinate Microemulsion - Evidence for Nonspherical Structures. Physica B *180*, 555-557.

Eastoe, J., Stebbing, S., Dalton, J., and Heenan, R. K. (1996). Preparation of colloidal cobalt using reversed micelles. Colloids and Surfaces a-Physicochemical and Engineering Aspects *119*, 123-131.

Eastoe, J., Steytler, D. C., Robinson, B. H., Heenan, R. K., Norht, A. N., and Dore, J. C. (1994). Structure of Cobalt Aerosl-OT Reversed Micelles Studied by Small-Angle

Scattering Methods. Journal of the Chemical Society-Faraday Transactions *90*, 2497-2504.

Eastoe, J., Towey, T. F., Robinson, B. H., Williams, J., and Heenan, R. K. (1993). Structures of Metal Bis(2-Ethylhexyl) Sulfosuccinate Aggregates in Cyclohexane. Journal of Physical Chemistry *97*, 1459-1463.

Egerton, R. F. (2005). Physical Principles of Electron Microscopy: Springer US).

Eicke, H. F., and Christen, H. (1973). On the Stability of Micelles in Apolar Media. Journal of Colloid and Interface Science *46*, 417-427.

Eicke, H. F., and Christen, H. (1978). IS WATER CRITICAL TO FORMATION OF MICELLES IN APOLAR MEDIA. Helvetica Chimica Acta *61*, 2258-2263.

Elschner, A., Kirchmeyer, S., Lovenich, W., Merker, U., and Reuter, K. (2011). PEDOT: Principles and Application of an Intrinsically Conductive Polymer, (Boca Raton, Fl: CRC Press).

Fuchigami, H., Tsumura, A., and Koezuka, H. (1993). POLYTHIENYLENEVINYLENE THIN-FILM-TRANSISTOR WITH HIGH CARRIER MOBILITY. Applied Physics Letters *63*, 1372-1374.

Gacek, M., Bergsman, D., Michor, E., and Berg, J. C. (2012). Effects of Trace Water on Charging of Silica Particles Dispersed in a Nonpolar Medium. Langmuir *28*, 11633-11638.

Garnier, F., Hajlaoui, R., Yassar, A., and Srivastava, P. (1994). ALL-POLYMER FIELD-EFFECT TRANSISTOR REALIZED BY PRINTING TECHNIQUES. Science *265*, 1684-1686.

Gelves, G. A., Al-Saleh, M. H., and Sundararaj, U. Highly electrically conductive and high performance EMI shielding nanowire/polymer nanocomposites by miscible mixing and precipitation. Journal of Materials Chemistry *21*, 829-836.

Gelves, G. A., Lin, B., Sundararaj, U., and Haber, J. A. (2006). Low electrical percolation threshold of silver and copper nanowires in polystyrene composites. Advanced Functional Materials *16*, 2423-2430.

Glatter, O., and Kratky, O. (1982). Glatter, O.; Kratky, O, (New York: Glatter, O.; Kratky, O).

Glinka, C. J., Barker, J. G., Hammouda, B., Krueger, S., Moyer, J. J., and Orts, W. J. (1998). The 30 m small-angle neutron scattering instruments at the National Institute of Standards and Technology. Journal of Applied Crystallography *31*, 430-445.

Goncalves, V. C., and Balogh, D. T. (2009). Optical VOCs detection using poly(3-alkylthiophenes) with different side-chain lengths. Sensors and Actuators B-Chemical *142*, 55-60.

Guardia E, and JA, P. (1990). Molecular Dyanmics Simulation of Ferrous and Ferric Ions in Water. Chemical Physics *144*, 353-362.

Guenes, S., Neugebauer, H., and Sariciftci, N. S. (2007). Conjugated polymer-based organic solar cells. Chemical Reviews *107*, 1324-1338.

Guinier, A., and Fournet, G. (1955). "Small-Angle Scattering of X-Rays", (New York: John Wiley and Sons).

Hall, D. A., and Elving, P. J. (1967). VOLTAMMETRY WITHOUT BACKGROUND ELECTROLYTE - REDOX PATTERN OF DPPH IN NON-AQUEOUS MEDIA. Electrochimica Acta *12*, 1363-&.

Hammouda, B. (1993). SANS from Heterogeneous Polymer Mixtures - A Unified Overview. Advances in Polymer Science, 87-133.

Hammouda, B. (2008). Probing Nampscale Structures –The SANS Toolbox. In, (Gaithersburg, MD).

Handbook of Chemistry and Physics: 83rd Edition, (Davers, MA: CRC Press LLC). (2002)

Hauser, H., Haering, G., Pande, A., and Luisi, P. L. (1989). INTERACTION OF WATER WITH SODIUM BIS(2-ETHYL-1-HEXYL) SULFOSUCCINATE IN REVERSED MICELLES. Journal of Physical Chemistry *93*, 7869-7876.

Haynes, J. S., Sams, J. R., and Thompson, R. C. (1981). Sythesis and Structural Studies of Iron(II) and Iron(III) Sulfonates. Canadian Journal of Chemistry-Revue Canadienne De Chimie *59*, 669-678.

Hecht, A. M., Duplessix, R., and Geissler, E. (1985). STRUCTURAL INHOMOGENEITIES IN THE RANGE 2.5-2500 A IN POLYACRYLAMIDE GELS. Macromolecules *18*, 2167-2173.

Horowitz, G. (1998). Organic field-effect transistors. Advanced Materials *10*, 365-377.

Huang, L., Huang, X., Sun, G., Gu, C., Lu, D., and Ma, Y. (2012). Study of beta phase and Chains Aggregation Degrees in Poly(9,9-dioctylfluorene) (PFO) Solution. Journal of Physical Chemistry C *116*, 7993-7999.

Huang, P.-T. C., Yao-Sheng Chou, Cheng-Wei (2011). Preparation of porous poly(3-hexylthiophene) by freeze-dry method and its application to organic photovoltaics. Journal of Applied Polymer Science.

Huang, W., Huang, P., Han, Y., Lee, C., Hsieh, T., and Chang, M. (2008). Aggregation and Gelation Effects on the Performance of Poly(3-hexylthiophene)/Fullerene Solar Cells. Macromolecules, 7485-7489.

Instruction Manual SAXSess Small-Angle X-Ray Scattering System, (Graz, Austria: Anton Paar GmbH). (2010)

Jonas, F., and Morrison, J. T. (1997). 3,4-polyethylenedioxythiophene (PEDT): Conductive coatings technical applications and properties. Synthetic Metals *85*, 1397-1398.

Jonsson, S. K. M., Birgerson, J., Crispin, X., Greczynski, G., Osikowicz, W., van der Gon, A. W. D., Salaneck, W. R., and Fahlman, M. (2003). The effects of solvents on the morphology and sheet resistance in poly (3,4-ethylenedioxythiophene)-polystyrenesulfonic acid (PEDOT-PSS) films. Synthetic Metals *139*, 1-10.

Justino, L. L. G., Luisa Ramos, M., Knaapila, M., Marques, A. T., Kudla, C. J., Scherf, U., Almasy, L., Schweins, R., Burrows, H. D., and Monkman, A. P. (2011). Gel Formation and Interpolymer Alkyl Chain Interactions with Poly(9,9-dioctylfluorene-2,7-diyl) (PFO) in Toluene Solution: Results from NMR, SANS, DFT, and Semiempirical Calculations and Their Implications for PFO beta-Phase Formation. Macromolecules *44*, 334-343.

Keum, J. K., Xiao, K., Ivanov, I. N., Hong, K., Browning, J. F., Smith, G. S., Shao, M., Littrell, K. C., Rondinone, A. J., Andrew Payzant, E*., et al.* (2013). Solvent quality-induced nucleation and growth of parallelepiped nanorods in dilute poly(3-hexylthiophene) (P3HT) solution and the impact on the crystalline morphology of solution-cast thin film. CrystEngComm *15*, 1114-1124.

Kienzle, P. (2014). Neutron activation and scattering calculator. In, (Gaithersbur, MD: NIST Center for Neutron Research).

Kim, B.-G., Jeong, E. J., Park, H. J., Bilby, D., Guo, L. J., and Kim, J. (2011). Effect of Polymer Aggregation on the Open Circuit Voltage in Organic Photovoltaic Cells: Aggregation-Induced Conjugated Polymer Gel and its Application for Preventing Open Circuit Voltage Drop. Acs Applied Materials & Interfaces *3*, 674-680.

Kim, F. S., and Jenekhe, S. A. (2012). Charge Transport in Poly(3-butylthiophene) Nanowires and Their Nanocomposites with an Insulating Polymer. Macromolecules *45*, 7514-7519.

Kim, J., Anderson, J. L., Garoff, S., and Schlangen, L. J. M. (2005). Ionic conduction and electrode polarization in a doped nonpolar liquid. Langmuir *21*, 8620-8629.

Kirchmeyer, S., and Reuter, K. (2005). Scientific importance, properties and growing applications of poly(3,4-ethylenedioxythiophene). Journal of Materials Chemistry *15*, 2077-2088.

Kline, S. R. (2006). Reduction and analysis of SANS and USANS data using IGOR Pro. Journal of Applied Crystallography *39*, 895-900.

Knaapila, M., Bright, D. W., Stepanyan, R., Torkkeli, M., Almasy, L., Schweins, R., Vainio, U., Preis, E., Galbrecht, F., Scherf, U., and Monkman, A. P. (2011). Network structure of polyfluorene sheets as a function of alkyl side chain length. Physical Review E *83*.

Knaapila, M., Garamus, V. M., Dias, F. B., Almasy, L., Galbrecht, F., Charas, A., Morgado, J., Burrows, H. D., Scherf, U., and Monkman, A. P. (2006). Influence of solvent quality on the self-organization of archetypical hairy rods - Branched and linear side chain polyfluorenes: Rodlike chains versus "beta-sheets" in solution. Macromolecules *39*, 6505-6512.

Knaapila, M., Stepanyan, R., Torkkeli, M., Garamus, V. M., Galbrecht, F., Nehls, B. S., Preis, E., Scherf, U., and Monkman, A. P. (2008). Control over phase behavior and solution structure of hairy-rod polyfluorene by means of side-chain length and branching. Physical Review E *77*.

Koezuka, H., Tsumura, A., Fuchigami, H., and Kuramoto, K. (1993). Polythiophene field-effect transistor with polypyrrole worked as source and drain electrodes. Applied Physics Letters *62*, 1794-1796.

Koppe, M., Brabec, C., Heiml, S., Schausberger, A., Duffy, W., Heeney, M., and McCulloch, I. (2009). Influence of Molecular Weight Distribution on the Gelation of P3HT and Its Impact on the Photovoltaic Performance. Macromolecules *42*, 4661-4666.

Kotlarchyk, M., and Chen, S. H. (1983). Analysis of Small-Angle Neutron Scattering Spectra from Polydisperse Interacting Colloids. Journal of Chemical Physics *79*, 2461-2469.

Kotlarchyk, M., Huang, J. S., and Chen, S. H. (1985). Structure of AOT-Reversed Micelles Determined by Small-Angle Neutron Scattering. Journal of Physical Chemistry *89*, 4382-4386.

Krebs, F. C. (2008). Air stable polymer photovoltaics based on a process free from vacuum steps and fullerenes. Solar Energy Materials and Solar Cells *92*, 715-726.

Kriwet, B., Walter, E., and Kissel, T. (1998). Synthesis of bioadhesive poly(acrylic acid) nano- and microparticles using an inverse emulsion polymerization method for the entrapment of hydrophilic drug candidates. Journal of Controlled Release *56*, 149-158.

Kumar, S., Sharma, D., and Kabir ud, D. (2006). Small-angle neutron scattering studies on sodium dodecylbenzenesulfonate-tetra-n-butylammonium bromide systems. Journal of Surfactants and Detergents *9*, 77-82.

Lan, Y.-K., and Huang, C.-I. (2008). A Theoretical Study of the Charge Transfer Behavior of the Highly Regioregular Poly-3-hexylthiophene in the Ordered State. The Journal of Physical Chemistry B *112*, 14857-14862.

Larson-Smith, K., and Pozzo, D. C. (2011). Scalable synthesis of self-assembling nanoparticle clusters based on controlled steric interactions. Soft Matter *7*, 5339-5347.

Li, J.-L., and Liu, X.-Y. (2010). Architecture of Supramolecular Soft Functional Materials: From Understanding to Micro-/Nanoscale Engineering. Advanced Functional Materials *20*, 3196-3216.

Li, J.-L., Yuan, B., Liu, X.-Y., and Xu, H.-Y. (2010a). Microengineering of Supramolecular Soft Materials by Design of the Crystalline Fiber Networks. Crystal Growth & Design *10*, 2699-2706.

Li, J., Yuan, B., Liu, X., and Xu, H. (2010b). Microengineering of Supramolecular Soft Materials by Design of the Crystalline Fiber Networks. Crystal Growth & Design, 2699-2706.

Li, J. L., Liu, X. Y., Wang, R. Y., and Xiong, J. Y. (2005). Architecture of a biocompatible supramolecular material by supersaturation-driven fabrication of its fiber network. Journal of Physical Chemistry B *109*, 24231-24235.

Lindner, P. (2002). Neutrons, X-Rays and Light: Scattering Methods Applied to Soft Condesed Matter., (Amsterdam: Elsevier Science).

Lindner, P., and Zemb, T. (2002). Neutrons, X-rays and Light: Scattering Methods Applied to Soft Condensend Matter, (Amsterdam: North Holland).

Liu, C.-H., and Yu, X. Silver nanowire-based transparent, flexible, and conductive thin film. Nanoscale Research Letters *6*.

Liu, J., Arif, M., Zou, J., Khondaker, S. I., and Zhai, L. (2009). Controlling Poly(3-hexylthiophene) Crystal Dimension: Nanowhiskers and Nanoribbons. Macromolecules *42*, 9390-9393.

Livsey, I. (1987). Neutron Scattering from Concentry Ciylinders - Interparticle Interference Function and Radius of Gyration Journal of the Chemical Society-Faraday Transactions Ii *83*, 1445-1452.

Loevenich, W. (2014). PEDOT-Properties and Applications. Polymer Science Series C *56*, 135-143.

Longo, A., Ruggirello, A., and Liveri, V. T. (2007). Physicochemical investigation of nanostructures in liquid phases: Ytterbium nitrate ionic clusters confined in ytterbium bis(2-ethylhexyl) sulfosuccinate reversed micelles and liquid crystals. Chemistry of Materials *19*, 1127-1133.

Lyklema, J. (2013). Principles of interactions in non-aqueous electrolyte solutions. Current Opinion in Colloid & Interface Science *18*, 116-128.

Lyskawa, J., Le Derf, F., Levillain, E., Mazari, M., Salle, M., Dubois, L., Viel, P., Bureau, C., and Palacin, S. (2004). Univocal demonstration of the electrochemically mediated binding of Pb2+ by a modified surface incorporating a TTF-based redox-switchable ligand. Journal of the American Chemical Society *126*, 12194-12195.

Macosko, C. W. (1994). Rheology Principles, Measurements, and Applications, (New York City, NY: Wiley-VCH).

Madaria, A. R., Kumar, A., and Zhou, C. Large scale, highly conductive and patterned transparent films of silver nanowires on arbitrary substrates and their application in touch screens. Nanotechnology *22*.

Malik, S., Jana, T., and Nandi, A. K. (2001). Thermoreversible gelation of regioregular poly(3-hexylthiophene) in xylene. Macromolecules *34*, 275-282.

Malik, S., and Nandi, A. K. (2002). Crystallization mechanism of regioregular poly(3-alkylthiophene)s. Journal of Polymer Science Part B-Polymer Physics *40*, 2073-2085.

Malik, S., and Nandi, A. K. (2004). Thermodynamic and structural investigation of thermoreversible poly(3-dodecylthiophene) gels in the three isomers of xylene. J Phys Chem B *108*, 597-604.

Marques, M. F. F., Burrows, H. D., Miguel, M. D., deLima, A. P., Gil, C. L., and Duplatre, G. (1997). Analysis and modelling of positron lifetime spectroscopy data for the characterisation of water-in-oil microemulsion systems stabilised by Aerosol OT - Effect of changing the counter-ion. Journal of the Chemical Society-Faraday Transactions *93*, 3827-3831.

Martens, H. C. F., Hulea, I. N., Romijn, I., Brom, H. B., Pasveer, W. F., and Michels, M. A. J. (2003). Understanding the doping dependence of the conductivity of conjugated

polymers: Dominant role of the increasing density of states and growing delocalization. Physical Review B *67*.

Martinez, L., Andrade, R., Birgin, E. G., and Martinez, J. M. (2009). PACKMOL: A Package for Building Initial Configurations for Molecular Dynamics Simulations. Journal of Computational Chemistry *30*, 2157-2164.

Mathews, M. B., and Hirschhorn, E. (1953). Solubilization and Micelle Formation in a Hydrocarbon Medium. Journal of Colloid Science *8*, 86-96.

McFarlane, S. L., Deore, B. A., Svenda, N., and Freund, M. S. (2010). A One-Step, Organic-Solvent Processable Synthesis of PEDOT Thin Films via in Situ Metastable Chemical Polymerization. Macromolecules *43*, 10241-10245.

Meyers, F., Heeger, A. J., and Bredas, J. L. (1992). FINE TUNING OF THE BAND-GAP IN CONJUGATED POLYMERS VIA CONTROL OF BLOCK COPOLYMER SEQUENCES. Journal of Chemical Physics *97*, 2750-2758.

Minami, T. (2005). Transparent conducting oxide semiconductors for transparent electrodes. Semiconductor Science and Technology *20*, S35-S44.

Mittelbach, P. (1961). Acta Phys Aust *14*, 185-211.

Morrison, I. D. (1993). Electrical Charges in Nonaqueous Media. Colloids and Surfaces a-Physicochemical and Engineering Aspects *71*, 1-37.

Nam, S., Cho, H. W., Lim, S., Kim, D., Kim, H., and Sung, B. J. Enhancement of Electrical and Thermomechanical Properties of Silver Nanowire Composites by the Introduction of Nonconductive Nanoparticles: Experiment and Simulation. Acs Nano *7*, 851-856.

Narkis, M., Lidor, G., Vaxman, A., and Zuri, L. (1999). New injection moldable electrostatic dissipative (ESD) composites based on very low carbon black loadings. Journal of Electrostatics *47*, 201-214.

Newbloom, G., Kim, F., Jenekhe, S., and Pozzo, D. (2011). Mesoscale Morphology and Charge Transport in Colloidal Networks of Poly(3-hexylthiophene). Macromolecules, 3801-3809.

Newbloom, G. M., Kim, F. S., Jenekhe, S. A., and Pozzo, D. C. (2012a). Mesoscale Morphology and Charge Transport in Colloidal Networks of Poly(3-hexylthiophene). Macromolecules *44*, 3801-3809.

Newbloom, G. M., Weigandt, K. M., and Pozzo, D. C. (2012b). Electrical, Mechanical, and Structural Characterization of Self-Assembly in Poly(3-hexylthiophene) Organogel Networks. Macromolecules *45*, 3452-3462.

Newbloom, G. M., Weigandt, K. M., and Pozzo, D. C. (2012c). Structure and property development of poly(3-hexylthiophene) organogels probed with combined rheology, conductivity and small angle neutron scattering. Soft Matter *8*.

Newbloom, G. M., Weigandt, K. M., and Pozzo, D. C. (2012d). Structure and property development of poly(3-hexylthiophene) organogels probed with combined rheology, conductivity and small angle neutron scattering. Soft Matter *8*, 8854-8864.

Omastova, M., Pionteck, J., and Trchova, M. (2003a). Properties and morphology of polypyrrole containing a surfactant. Synthetic Metals *135*, 437-438.

Omastova, M., Trchova, M., Kovarova, J., and Stejskal, J. (2003b). Synthesis and structural study of polypyrroles prepared in the presence of surfactants. Synthetic Metals *138*, 447-455.

Oosterbaan, W. D., Bolsée, J.-C., Gadisa, A., Vrindts, V., Bertho, S., D'Haen, J., Cleij, T. J., Lutsen, L., McNeill, C. R., Thomsen, L.*, et al.* (2010). Alkyl-Chain-Length-Independent Hole Mobility via Morphological Control with Poly(3-alkylthiophene) Nanofibers. Advanced Functional Materials *20*, 792-802.

Opawale, F. O., and Burgess, D. J. (1998). Influence of interfacial properties of lipophilic surfactants on water-in-oil emulsion stability. Journal of Colloid and Interface Science *197*, 142-150.

Piper, J. D., Fleiger, A. G., Smith, C. C., and Kerstein, N. A. (1939). Electrical insulating materials - Liquid dielectrics - Chemical, physical, electrical properties of systems containing lead or copper soaps in liquid paraffin. Industrial and Engineering Chemistry *31*, 307-317.

Plesse, C., Vidal, F., Randriamahazaka, H., Teyssie, D., and Chevrot, C. (2005). Synthesis and characterization of conducting interpenetrating polymer networks for new actuators. Polymer *46*, 7771-7778.

Poovarodom, S., and Berg, J. C. Effect of particle and surfactant acid-base properties on charging of colloids in apolar media. Journal of Colloid and Interface Science *346*, 370-377.

Pozzo, D., and Newbloom, G. (2013). Composites incorporating a conductive polymer nanofiber network. In, (Google Patents).

Prosa, T., Winokur, M., Moulton, J., Smith, P., and Heeger, A. (1992). X-Ray Structural Studies of Poly(3-alkylthiophenes) - An Example of an Inverse Comb. Macromolecules, 4364-4372.

Rai, R., Baker, G. A., Behera, K., Mohanty, P., Kurur, N. D., and Pandey, S. (2010). Ionic Liquid-Induced Unprecedented Size Enhancement of Aggregates within Aqueous Sodium Dodecylbenzene Sulfonate. Langmuir *26*, 17821-17826.

Rao, C. R. K., Muthukannan, R., Jebin, J. A., Raj, T. A., and Vijayan, M. (2013). Synthesis and properties of polypyrrole obtained from a new Fe(III) complex as oxidizing agent. Indian Journal of Chemistry Section a-Inorganic Bio-Inorganic Physical Theoretical & Analytical Chemistry *52*, 744-748.

Rees, G. D., Evans-Gowing, R., Hammond, S. J., and Robinson, B. H. (1999). Formation and morphology of calcium sulfate nanoparticles and nanowires in water-in-oil microemulsions. Langmuir *15*, 1993-2002.

Remsungnen, T., and Rode, B. M. (2003). QM/MM molecular dynamics simulation of the structure of hydrated Fe(II) and Fe(III) ions. Journal of Physical Chemistry A *107*, 2324-2328.

Riande, E., and R., D.-C. (2004). Electrical Properties of Polymers, (New York: Marcel Dekker).

Richards, J. J., Weigandt, K. M., and Pozzo, D. C. (2011). Aqueous dispersions of colloidal poly(3-hexylthiophene) gel particles with high internal porosity. Journal of Colloid and Interface Science *364*, 341-350.

Roncali, J. (1997). Synthetic principles for bandgap control in linear pi-conjugated systems. Chemical Reviews *97*, 173-205.

Roncali, J., Blanchard, P., and Frere, P. (2005). 3,4-Ethylenedioxythiophene (EDOT) as a versatile building block for advanced functional p-conjugated systems. Journal of Materials Chemistry *15*, 1589-1610.

Samitsu, S., Shimomura, T., Heike, S., Hashizume, T., and Ito, K. (2008a). Effective Production of Poly(3-alkylthiophene) Nanofibers by means of Whisker Method using Anisole Solvent: Structural, Optical, and Electrical Properties. Macromolecules *41*, 8000-8010.

Samitsu, S., Shimomura, T., Heike, S., Hashizume, T., and Ito, K. (2010). Field-Effect Carrier Transport in Poly(3-alkylthiophene) Nanofiber Networks and Isolated Nanofibers. Macromolecules *43*, 7891-7894.

Samitsu, S., Shimomura, T., and Ito, K. (2008b). Nanofiber preparation by whisker method using solvent-soluble conducting polymers. Thin Solid Films *516*, 2478-2486.

Schweizer, K. S. (1986). Order–disorder transitions of π-conjugated polymers in condensed phases. I. General theory. The Journal of Chemical Physics *85*, 1156-1175.

Seidler, N., Lazzerini, G. M., Destri, G. L., Marletta, G., and Cacialli, F. (2013). Enhanced crystallinity and film retention of P3HT thin-films for efficient organic solar cells by use of preformed nanofibers in solution. Journal of Materials Chemistry C *1*, 7748-7757.

Shinkle, A. A., Pomaville, T. J., Sleightholme, A. E. S., Thompson, L. T., and Monroe, C. W. (2014). Solvents and supporting electrolytes for vanadium acetylacetonate flow batteries. Journal of Power Sources *248*, 1299-1305.

Shrestha, L. K., Glatter, O., and Aramaki, K. (2009). Structure of Nonionic Surfactant (Glycerol alpha-Monomyristate) Micelles in Organic Solvents: A SAXS Study. Journal of Physical Chemistry B *113*, 6290-6298.

Sirringhaus, H., Brown, P. J., Friend, R. H., Nielsen, M. M., Bechgaard, K., Langeveld-Voss, B. M. W., Spiering, A. J. H., Janssen, R. A. J., Meijer, E. W., Herwig, P., and de Leeuw, D. M. (1999). Two-dimensional charge transport in self-organized, high-mobility conjugated polymers. Nature *401*, 685-688.

Sobkowicz, M. J., Jones, R. L., Kline, R. J., and DeLongchamp, D. M. (2011). Effect of Fullerenes on Crystallization-Induced Aggregation in Polymer Photovoltaics Casting Solutions. Macromolecules *45*, 1046-1055.

Strobl, G. (2007). The Physics of Polymers, (New Yotk: Springer).

Sun, Y., Zhang, J.-M., and Xu, K.-W. First-principles study on the relaxed structures and electronic properties of Cu [110] nanowires. Journal of the Korean Physical Society *61*, 1015-1020.

Szymanski, C., Wu, C., Hooper, J., Salazar, M. A., Perdomo, A., Dukes, A., and McNeill, J. (2005). Single Molecule Nanoparticles of the Conjugated Polymer MEH−PPV, Preparation and Characterization by Near-Field Scanning Optical Microscopy. The Journal of Physical Chemistry B *109*, 8543-8546.

Tabor, R. F., Eastoe, J., Dowding, P. J., Grillo, I., and Rogers, S. E. (2010). Bidisperse colloids: Nanoparticles and microemulsions in coexistence. Journal of Colloid and Interface Science *344*, 447-450.

Tolcin, A. C. (2015). Mineral commodity summaries 2015. In Mineral Commodities Summaries, (Reston, VA C6 -), pp. 74-75.

Tourillon, G., and Garnier, F. (1983). Effect of Dopant on the Physicochemical and Electrical-Properties of Organic Condcuting Polymer. Journal of Physical Chemistry *87*, 2289-2292.

Towey, T. F., Baglioni, P., Martini, G., and Ristori, S. (1995). ESR Spectroscopy of Metal Bis(2-Ethylhexyl) Sulfoccinate Aggregates in Cyclohexane Journal of Physical Chemistry *99*, 3939-3942.

Wall, J. S., and Hainfeld, J. F. (1986). MASS MAPPING WITH THE SCANNING-TRANSMISSION ELECTRON-MICROSCOPE. Annual Review of Biophysics and Biophysical Chemistry *15*, 355-376.

Wang J, Wolf RM, Caldwell JW, Kollman PA, and DA., C. (2005). Development and Testing of a General Amber Forced Field. Journal of Computational Chemistry *25*, 1157-1174.

Welzel, H. P., Kossmehl, G., Schneider, J., and Plieth, W. (1995). Reactive Groups on Polymer-Covered Electrodes. 2. Functionalized Thiophene Polymers by Electrochemical Polymerization and Their Application as Polymeric Reagents. Macromolecules *28*, 5575-5580.

Xie, Z., Liu, Q., Chang, Z., and Zhang, X. (2013). The developments and challenges of cerium half-cell in zinc-cerium redox flow battery for energy storage. Electrochimica Acta *90*, 695-704.

Xu, W., Li, L., Tang, H., Li, H., Zhao, X., and Yang, X. (2011). Solvent-Induced Crystallization of Poly(3-dodecylthiophene): Morphology and Kinetics. The Journal of Physical Chemistry B *115*, 6412-6420.

Xu, W., Tang, H., Lv, H., Li, J., Zhao, X., Li, H., Wang, N., and Yang, X. (2012). Sol-gel transition of poly(3-hexylthiophene) revealed by capillary measurements: phase behaviors, gelation kinetics and the formation mechanism. Soft Matter *8*, 726-733.

Yu, Z., Fang, J., Yan, H., Zhang, Y., Lu, K., and Wei, Z. (2012). Self-Assembly of Well-Defined Poly(3-hexylthiophene) Nanostructures toward the Structure–Property Relationship Determination of Polymer Solar Cells. The Journal of Physical Chemistry C *116*, 23858-23863.

Zallen, R. (1983). The Physics of Amorphous Solids, (New York: Wiley).

Zhang, D., Lan, H., and Li, Y. (2012). The application of a non-aqueous bis(acetylacetone)ethylenediamine cobalt electrolyte in redox flow battery. Journal of Power Sources *217*, 199-203.

Zhang, D., Ryu, K., Liu, X., Polikarpov, E., Ly, J., Tompson, M. E., and Zhou, C. (2006). Transparent, conductive, and flexible carbon nanotube films and their application in organic light-emitting diodes. Nano Letters *6*, 1880-1886.

Zhu, Z., Wei, B., and Wang, J. (2013). Self-assembly of poly(3-hexylthiophene) nanowire networks by a mixed-solvent approach for organic field-effect transistors. physica status solidi (RRL) – Rapid Research Letters,